Front page

Exam information
NFYK10020E - Physics Thesis 60 ECTS, Niels Bohr Institute - Contract:140651 (Miao Shang)

Handed in by
Miao Shang
mqz696@alumni.ku.dk

Exam administrators
Eksamensteam, tel 35 33 64 57
eksamen@science.ku.dk

Assessors
Jose Maria Ezquiaga
Examiner
jose.ezquiaga@nbi.ku.dk
+4535329633

Marta Orselli
Co-examiner
orselli@nbi.ku.dk

Hand-in information

Title: Exploring the Large-Scale Structure of the Universe through Lensing of Grav- itational Waves: Detectability, Signal Properties, and Population Inferences
Title, english: Exploring the Large-Scale Structure of the Universe through Lensing of Grav- itational Waves: Detectability, Signal Properties, and Population Inferences
The sworn statement: Yes
Does the hand-in contain confidential material: No

UNIVERSITY OF COPENHAGEN
DEPARTMENT OF MATHEMATICAL SCIENCES

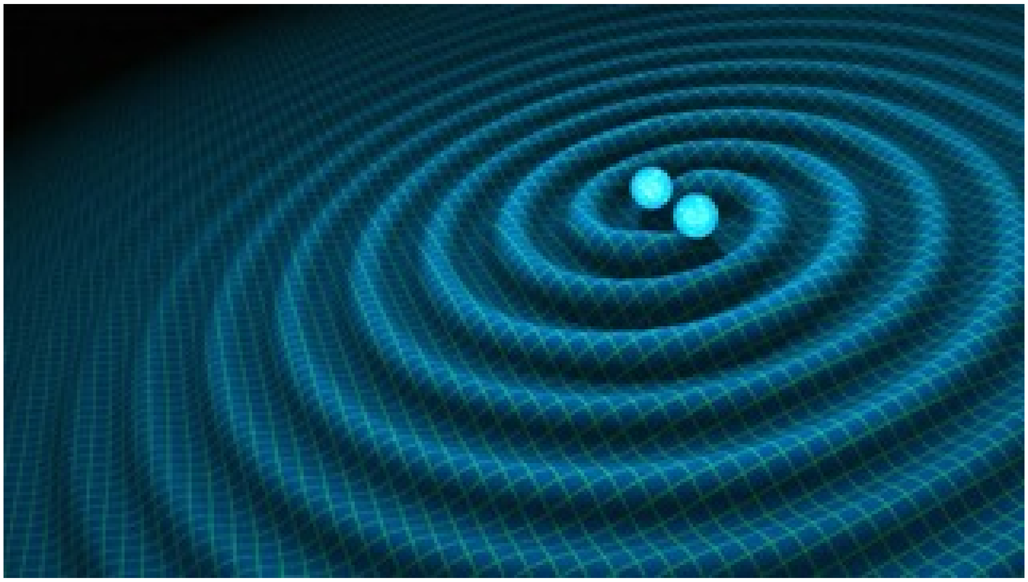

Master's thesis

Miao Shang

Exploring the Large-Scale Structure of the Universe through Lensing of Gravitational Waves: Detectability, Signal Properties, and Population Inferences

Date: Dec 2024

Advisor: Jose Maria Ezquiaga

Institute:	Niels Bohr Institute
Author(s):	Miao Shang
Title and subtitle:	Exploring the Large-Scale Structure of the Universe through Lensing of Gravitational Waves: Detectability, Signal Properties, and Population Inferences
Description:	This thesis explores the detectability and implications of gravitational wave lensing as a means to investigate the large-scale structure of the universe. Gravitational waves, ripples in spacetime caused by accelerated massive objects, offer a unique window into cosmic events like black hole and neutron star mergers. This study focuses on how these waves, when lensed by massive structures such as galaxies or galaxy clusters, can be distorted, delayed, or even amplified, providing critical insights into both the properties of the waves and the intervening matter. By simulating lensing effects and analyzing signal properties, we examine the potential biases in parameter estimation and identify ways to distinguish lensed signals from unlensed ones. Using Bayesian inference methods, we infer the population characteristics of compact binaries and propose new models for signal detection in future observatories. The results underscore the transformative role of gravitational wave lensing in expanding our understanding of both gravitational waves and the distribution of matter in the universe.
Advisor:	Jose Maria Ezquiaga
Date:	18 12 2024

Table of content

1 Introduction: History and Motivation

Albert Eintein firstly predicted gravitational waves (GWs) in his theory of general relativity (GR) [1]. GWs represent perturbations in the spacetime fabric, which are caused by the acceleration of massive, compact objects. In 1916, Einstein developed the field equations of GR. He predicted that GW amplitudes would be extremely small. That same year, Schwarzschild introduced a solution to the GR equations [2], which was later recognized as the description of a black hole (BH) [3, 4]. Kerr extended this solution to account for rotating BHs in 1963 [5]. Subsequent theoretical advancements in the 1970s led to a deeper understanding of BH quasinormal modes [6, 7, 8]. By the 1990s, more sophisticated post-Newtonian (PN) calculations [9] were developed, leading to significant progress in the analytical study of relativistic two-body systems [10, 11]. Despite the identification of numerous BH candidates through electromagnetic means [12, 13, 14], direct observation of BH mergers remained elusive until recent advancements [15].

In the 1960s, scientists began efforts to observe GWs, with Weber taking a leading role in developing resonant mass detectors [16]. The concept of interferometric detectors emerged in the early 1960s [17] and 1970s [18]. Subsequent studies focused on the noise characteristics [19] and performance optimization of these detectors [20], which eventually led to the proposal of long-baseline broadband laser interferometers capable of achieving far greater sensitivity [21, 22, 23, 24]. By the early 2000s, several interferometric detectors were established. Among the operational detectors were Virgo [24] in Italy, GEO 600 in Germany, Laser Interferometer Gravitational-Wave Observatory (LIGO) [23] in the United States, and TAMA 300 in Japan. These detectors, working in conjunction, began joint observation runs between 2002 and 2011, progressively improving and contributing to the formation of a global observational network [15, 25, 26, 27, 28].

The first indirect evidence of GWs was provided by the observation of PSR B1913+16 [29], a neutron star (NS) binary whose orbit was found to be shrinking due to energy loss via GW emission. This observation indirectly confirmed the existence of GWs. As the orbit of a binary neutron star (BNS) system gradually contracts, the emission of GWs intensifies, speeding up the inspiral phase. This phase was long anticipated to generate GW signals detectable by ground-based observatories during the final moments leading up to the stars' merger. The detection of GW170817 [30], near the end of Advanced LIGO's (ALIGO) second observing run (O2), offered direct evidence supporting these theoretical predictions. The inspiral signal was observed in the detectors' sensitive band for about 100 seconds, culminating in a coalescence that was followed by a gamma-ray burst 1.7 seconds later.

In 2015, GWs were directly detected by the LIGO observatories in Hanford (H1) and Livingston (L1) for the first time. The observation, known as GW150914 [31], confirmed a major prediction of Einstein's GR and marked the beginning of GW astronomy. This discovery has since been followed by numerous detections, including the first observation of a NS merger, which provided insights into the origin of heavy elements like gold and platinum [32]. LIGO's observations have also allowed scientists to test the properties of BHs and explore the strong-field regime of GR in ways that were previously impossible [15, 33, 34].

2 Gravitational Waves

2.1 What are gravitational waves?

GWs are solutions to the Einstein Field Equations (EFEs) within the theoretical framework of GR, providing profound insights into how the geometry of spacetime is influenced by the existence and distribution of matter and energy [10]. The EFEs are fundamental to understanding the interplay between mass-energy content and the curvature of spacetime and are mathematically expressed as:

$$G_{\mu\nu} = \frac{8\pi G}{c^4} T_{\mu\nu} \tag{1}$$

In this equation, $G_{\mu\nu}$ denotes the Einstein tensor, which encapsulates information about the curvature of spacetime resulting from mass and energy. The stress-energy tensor $T_{\mu\nu}$, provides a detailed description of the distribution and flow of energy and momentum within spacetime. Together, these tensors bridge the geometric and physical aspects of general relativity, illustrating how mass-energy dictates the curvature that GWs propagate through.

Mathematically, $G_{\mu\nu}$ can also be defined using Ricci tensor, metric tensor and Ricci scalar:

$$G_{\mu\nu} = R_{\mu\nu} - \frac{1}{2} g_{\mu\nu} R, \tag{2}$$

where $R_{\mu\nu}$ represents the Ricci tensor. Using the Riemann curvature tensor, one can obtain the Ricci tensor and it serves as a measure of the degree to which spacetime is curved in a specific region. By measuring the difference in volume between a small geodesic ball in curved spacetime and flat space, it quantifies the effect of curvature.

The metric tensor $g_{\mu\nu}$ is a essential entity in GR that defines the geometric properties of spacetime, including distances and angles between nearby points. It essentially provides the ”shape” of spacetime, determining how objects move and how light propagates within it. The Ricci scalar R, derived from the Ricci tensor through the relation:

$$R = g^{\mu\nu} R_{\mu\nu}, \tag{3}$$

By contracting the Ricci tensor with the inverse metric tensor $g^{\mu\nu}$, it provides a scalar measure of spacetime curvature.

When dealing with weak gravitational fields and negligible spacetime curvature, the metric tensor $g_{\mu\nu}$ can be modeled as a small perturbation around the flat Minkowski metric $\eta_{\mu\nu}$ [35]:

$$g_{\mu\nu} = \eta_{\mu\nu} + h_{\mu\nu}, \quad |h_{\mu\nu}| \ll 1 \tag{4}$$

here, $h_{\mu\nu}$ is small perturbation representing the gravitational field. This approximation is known as linearized gravity, where the spacetime metric is treated as a small perturbation around flat spacetime. It simplifies the complex, highly nonlinear EFEs Eq.1 into linear equation sets that can be resolved with greater ease.

In linearized gravity, the perturbation $h_{\mu\nu}$ must satisfy a wave equation similar to the wave equation in electromagnetism due to the structure of the linearized EFEs and the physical nature of small perturbations propagating through spacetime. The Lorentz gauge condition is a constraint applied to simplify the equations in both electromagnetism and general relativity. In the context of linearized gravity, it is used to simplify the EFEs Eq.1 by imposing a condition on the metric perturbation $h_{\mu\nu}$.

The Lorentz gauge condition plays a pivotal role in simplifying the EFEs within the context of general relativity. As delineated by Misner et al. [35], the Lorentz gauge condition is mathematically formulated as:

$$\partial^{\nu} \bar{h}_{\mu\nu} = 0 \tag{5}$$

In this formulation, $\bar{h}_{\mu\nu}$ represents the trace-reversed perturbation of the metric tensor, defined by:

$$\bar{h}_{\mu\nu} = h_{\mu\nu} - \frac{1}{2}\eta_{\mu\nu} h \tag{6}$$

Here, The perturbation's trace, h, is expressed as $h = \eta^{\mu\nu} h_{\mu\nu}$, where $\eta^{\mu\nu}$ is the inverse Minkowski metric tensor. The trace-reversed perturbation $\bar{h}_{\mu\nu}$ serves to decouple EFEs, facilitating a more straightforward analysis of GW propagation.

Under the Lorentz gauge condition, the linearized EFEs simplify significantly. Specifically, they reduce to the wave equation:

$$\Box \bar{h}_{\mu\nu} = 0 \tag{7}$$

In this equation, $\Box$ denotes the d'Alembertian operator, defined as $\Box = \partial^{\alpha}\partial_{\alpha}$. Weinberg [36] provides an extensive discussion on the properties and applications of the d'Alembertian operator in the context of wave propagation in spacetime.

In the framework of Minkowski space, and using standard Cartesian coordinates (t, x, y, z), the d'Alembertian operator takes the explicit form:

$$\Box = \partial^{\mu}\partial_{\mu} = \eta^{\mu\nu}\partial_{\nu}\partial_{\mu} = \frac{1}{c^2}\frac{\partial^2}{\partial t^2} - \frac{\partial^2}{\partial x^2} - \frac{\partial^2}{\partial y^2} - \frac{\partial^2}{\partial z^2} = \frac{1}{c^2}\frac{\partial^2}{\partial t^2} - \nabla^2 \tag{8}$$

In this expression, ∇^2 represents the three-dimensional Laplacian operator, which accounts for spatial derivatives. The Minkowski metric tensor $\eta^{\mu\nu}$ is defined with components:

$$\eta_{00} = 1, \quad \eta_{11} = \eta_{22} = \eta_{33} = -1, \quad \eta_{\mu\nu} = 0 \quad \text{for} \quad \mu \neq \nu \tag{9}$$

This signature of the Minkowski metric ensures that the spacetime interval retains its invariant form under Lorentz transformations, a cornerstone of special relativity.

The resultant wave equation $\Box \bar{h}_{\mu\nu} = 0$ characterizes the propagation of GWs in a flat spacetime background. Solutions to this equation describe pacetime ripples that propagate at light speed, transmitting energy and information from their sources in the cosmos. The linearized approach, utilizing small perturbations $h_{\mu\nu}$ around the Minkowski metric, is essential for studying GWs in weak-field regimes where spacetime deviations from flatness are minimal.

In the analysis of GWs, the transverse-traceless (TT) gauge [37] is typically employed, ensuring that the perturbation $h_{\mu\nu}$ meets supplementary conditions :

1. Transverse condition:

$$\partial^\mu h_{\mu\nu} = 0 \tag{10}$$

this divergence-free condition ensures that the GW is transverse to its direction of propagation.

2. Traceless condition:

$$h^\mu_\mu = 0 \tag{11}$$

the perturbation has zero trace, eliminating scalar modes and focusing on tensor modes.

3. Temporal gauge condition:

$$h_{0\mu} = 0 \tag{12}$$

this sets the time components of the perturbation to zero, isolating spatial oscillation.

The conditions imposed by the TT gauge is important in simplifying the representation of GWs. Specifically, these conditions restrict the GW to possess only two independent polarization states, commonly denoted as h_+ and $h_\times$. This reduction is fundamental for analyzing the physical effects of GWs on spacetime and for facilitating their detection through interferometric observatories.

In the TT gauge, the metric perturbation h_{ij} characterizing a plane GW propagating in the z-direction is elegantly expressed as:

$$h_{ij}(t,z) = \begin{pmatrix} h_+(t-z) & h_\times(t-z) & 0 \\ h_\times(t-z) & -h_+(t-z) & 0 \\ 0 & 0 & 0 \end{pmatrix} \tag{13}$$

At a given time t and position z along the propagation direction, $h_{ij}(t,z)$ describes the spatial components of the metric perturbation tensor. The GW possesses two non-zero components, h_+ and $h_\times$, which correspond to its two distinct polarization states.

Plus Polarization (h_+): The h_+ polarization describes a stretching and squeezing effect along the x- and y-axes. As the GW passes through a region of space, objects aligned along the x-axis are alternately stretched and compressed along the y-axis, and vice versa. This oscillatory behavior creates a "plus" shaped distortion pattern.

Cross Polarization ($h_\times$): The $h_\times$ polarization induces a similar stretching and squeezing effect but rotated by 45° relative to the h_+ polarization. This results in a "cross" shaped distortion pattern, where the principal axes of stretching and compression are oriented diagonally with respect to the x- and y-axes.

The matrix form of $h_{ij}(t,z)$ in Eq. (13) succinctly encapsulates the essence of GW polarizations in the TT gauge. The off-diagonal terms $h_\times(t-z)$ introduce shear distortions, while the diagonal terms $h_+(t-z)$ and $-h_+(t-z)$ account for the stretching and squeezing along perpendicular axes. The zeros in the third row and column indicate that there is no perturbation in the z-direction, consistent with the transversality condition of the TT gauge, which stipulates that GWs are purely transverse to the direction of propagation.

The dependence of h_+ and $h_\times$ on $t-z$ signifies that these polarization states propagate as waves moving in the positive z-direction at the speed of light. This wave-like propagation is a direct consequence of the linearized EFEs under the TT gauge, which describe how disturbances in spacetime curvature propagate through the vacuum.

The influence of GW on matter can be described using the geodesic deviation equation [37], which shows how nearby free-falling particles oscillate due to the passage of GWs:

$$\frac{D^2\xi^\mu}{d\tau^2} = -R^\mu_{\nu\rho\sigma}\xi^\rho u^\sigma \tag{14}$$

where ξ^μ is the separation vector between neighboring geodesics, $u^\nu = \frac{dx^\nu}{d\tau}$ is the four-velocity of the reference geodesic, τ is the proper time along the geodesic, $\frac{D}{d\tau}$ denotes the covariant derivative along the geodesic.

Applying the metric perturbation Eq.4 and transverse-traceless gauge, the geodesic deviation equation reduces to:

$$\frac{d^2\xi^i}{dt^2} = -R^i_{\ 0j0}\xi^j \tag{15}$$

where ξ^j represents the separation vector between two particles, and $R^i_{\ 0j0}$ are the components of the Riemann curvature tensor [35], which are directly related to the wave amplitude h_{ij}.

In the linear approximation, the Riemann tensor is expressed in terms of the metric perturbation:

$$R^\mu{}_{\nu\rho\sigma} = \frac{1}{2}\left(\partial_\rho\partial_\nu h^\mu{}_\sigma + \partial_\sigma\partial^\mu h_{\nu\rho} - \partial_\sigma\partial_\nu h^\mu{}_\rho - \partial_\rho\partial^\mu h_{\nu\sigma}\right) \tag{16}$$

and the relevant components are:

$$R^i_{\ 0j0} = -\frac{1}{2}\frac{\partial^2 h_{ij}}{\partial t^2} \tag{17}$$

the geodesic deviation equation Eq.15 becomes:

$$\frac{d^2\xi^i}{dt^2} = \frac{1}{2}\frac{\partial^2 h_{ij}}{\partial t^2}\xi^j \tag{18}$$

and the components of the equation become:

$$\frac{d^2\xi^1}{dt^2} = \frac{1}{2}\left(\frac{\partial^2 h_{11}}{\partial t^2}\,\xi^1 + \frac{\partial^2 h_{12}}{\partial t^2}\,\xi^2\right) \tag{19}$$

$$\frac{d^2\xi^2}{dt^2} = \frac{1}{2}\left(\frac{\partial^2 h_{21}}{\partial t^2}\,\xi^1 + \frac{\partial^2 h_{22}}{\partial t^2}\,\xi^2\right) \tag{20}$$

using the expression for h_{ij} in Eq.13, the equations become:

$$\frac{d^2\xi^1}{dt^2} = \frac{1}{2}\left(\frac{\partial^2 h_+}{\partial t^2}\,\xi^1 + \frac{\partial^2 h_\times}{\partial t^2}\,\xi^2\right) \tag{21}$$

$$\frac{d^2\xi^2}{dt^2} = \frac{1}{2}\left(\frac{\partial^2 h_\times}{\partial t^2}\,\xi^1 - \frac{\partial^2 h_+}{\partial t^2}\,\xi^2\right) \tag{22}$$

For a GW propagating in the z-direction, the geodesic deviation equation results in oscillatory motion for test particles in the x and y directions, showing the characteristic stretching and squeezing effect associated with the h_+ and $h_\times$ polarizations.

Assume a monochromatic GW:

$$h_+(t) = h_0\cos(\omega t) \tag{23}$$

then

$$\frac{d^2\xi^1}{dt^2} = -\frac{1}{2}h_0\omega^2\cos(\omega t)\xi^1 \tag{24}$$

the solution to this equation is:

$$\xi^1(t) = \xi^1(0) + \delta\xi^1(t) \tag{25}$$

where $\delta\xi^1(t)$ represents the oscillatory motion induced by the GW.

The fractional change in separation $\Delta\xi^i/\xi^i$ scales with the GW's amplitude h_0:

$$\frac{\Delta\xi^i}{\xi^i} \approx \frac{1}{2}h_0 \tag{26}$$

this shows that the GWs produce extremely small deformations.

GWs carry energy, momentum, and angular momentum. In linearized theory, the energy flux of a GW can be described by the Isaacson stress-energy pseudo tensor [38], $t^{\mu\nu}$, in the shortwavelength approximation, it approximates the effective energy-momentum carried by GWs:

$$\langle t^{\mu\nu} \rangle = \frac{c^4}{32\pi G} \langle \partial^\mu h_{ij} \partial^\nu h^{ij} \rangle. \tag{27}$$

The energy density is:

$$\rho_{\mathrm{GW}} = t_{00}^{(\mathrm{GW})} = \frac{1}{32\pi G} \left\langle \frac{\partial h_{ij}}{\partial t} \frac{\partial h^{ij}}{\partial t} \right\rangle \tag{28}$$

The energy density of a plane wave moving in the z-direction is given by:

$$\rho_{\mathrm{GW}} = \frac{1}{16\pi G} \left\langle (\frac{\partial h_{ij}}{\partial t})^2 \right\rangle \tag{29}$$

Along the z-axis, the energy flux is:

$$\mathcal{F}_z = c\, t_0 z^{(\mathrm{GW})} = \frac{c}{16\pi G} \left\langle (\frac{\partial h_{ij}}{\partial t})^2 \right\rangle \tag{30}$$

The total energy passing through a surface S over time T is given by:

$$E = \int_0^T dt \int_S \mathcal{F}_i\, n^i\, dA = \int_0^T dt \int_S t_{0i}^{(\mathrm{GW})}\, n^i\, dA \tag{31}$$

The angular momentum flux density is related to the stress-energy pseudo tensor:

$$\mathcal{J}^i = \epsilon^{ijk} x_j t_{0k}^{(\mathrm{GW})} \tag{32}$$

where ϵ^{ijk} is the Levi-Civita symbol, and x_j are spatial coordinates. The total angular momentum is:

$$J^i = \int_0^T dt \int_S \mathcal{J}^i dA = \int_0^T dt \int_S \epsilon^{ijk} x_j t_{0k}^{(\mathrm{GW})} dA \tag{33}$$

2.2 Gravitational waves from compact binary coalescence: binary black hole, binary neutron star

CBC, which stands for compact binary coalescence, involves the merging of a pair of compact objects.These can be BHs, NSs, or one of each. BHs have strong gravity, preventing even light from escaping. NSs are supernova remnants made mostly of neutrons. Their densities are similar to those of atomic nuclei.

When the objects orbit each other, their mutual gravitational attraction causes them to accelerate, this acceleration leads to the release of GWs, resulting in the system losing energy. As a result, the orbiting objects lose energy, and their orbits decay, causing them to spiral inward toward each other.

For a binary system involving two compact masses, m_1 and m_2, the total mass M is the sum $M = m_1 + m_2$, and the reduced mass μ is expressed as $\mu = \frac{m_1 m_2}{M}$. The distance between the two objects is r, and they orbit each other in nearly circular orbits.

The quadrupole moment tensor is:

$$Q_{ij} = \sum_{a=1}^{2} m_a (x_a^i x_a^j - \frac{1}{3}\delta_{ij} r_a^2)$$

and the third time derivative for a circular orbit in the x-y plane is:

$$\dddot{Q} xx = 4\mu r^2 \omega^3 \sin(2\omega t) \tag{34}$$

$$\dddot{Q} yy = -4\mu r^2 \omega^3 \sin(2\omega t) \tag{35}$$

$$\dddot{Q} xy = -4\mu r^2 \omega^3 \cos(2\omega t) \tag{36}$$

The quadrupole formula for power P radiated is:

$$P = -\frac{G}{5c^5} \left\langle \dddot{Q}_{ij} \dddot{Q}^{ij} \right\rangle \tag{37}$$

since $\dddot{Q}_{ij}$ is a symmetric tensor and only xx, yy, xy components are non-zero, the sum is:

$$\dddot{Q} ij \dddot{Q}^{ij} = (\dddot{Q} xx)^2 + (\dddot{Q} yy)^2 + 2(\dddot{Q} xy)^2 \tag{38}$$

we will get:

$$\dddot{Q}_{ij} \dddot{Q}^{ij} = 16\mu^2 r^4 \omega^6 \left(2\sin^2(2\omega t) + 2\cos^2(2\omega t)\right) \tag{39}$$

$$= 32\mu^2 r^4 \omega^6 \tag{40}$$

$$P = -\frac{G}{5c^5} \times 32\mu^2 r^4 \omega^6 = -\frac{32G}{5c^5}\mu^2 r^4 \omega^6 \tag{41}$$

Eq.41 can be simplified and since power is positive, we can drop the negative sign:

$$P = \frac{32G}{5c^5}\mu^2 (GM)^{4/3} \omega^{10/3} \tag{42}$$

The power radiated by GWs depends on the square of the reduced mass, so systems with more equal masses emit GWs more efficiently, and more massive systems emit more gravitational radiation. As the masses spiral inwards due to energy loss, orbital frequency increases, and the power radiated increases rapidly with ω.

Likewise, The system's orbital energy, E, is defined as [35]:

$$E = -\frac{Gm_1m_2}{2r} \tag{43}$$

According to GR, the system loses energy due to the emission of gravitational radiation, which is given by the quadrupole formula [39]:

$$\frac{dE}{dt} = -\frac{32}{5}\frac{G^4}{c^5}\frac{(m_1m_2)^2(m_1+m_2)}{r^5} \tag{44}$$

The rate of the energy loss $\frac{dE}{dt}$ is proportional to $\frac{1}{r^5}$, meaning as the objects get closer together, the energy loss increases rapidly [10].

Due to the system's energy loss, the two bodies draw nearer by spiraling towards one another and the orbital angular frequency ω increases [37]:

$$\omega^2 = \frac{G(m_1+m_2)}{r^3} \tag{45}$$

The frequency of the GWs emitted by a BBH system is intrinsically linked to the orbital dynamics of the system. Specifically, the GW frequency is observed to be twice the orbital frequency of the binary system [40]. This relationship arises due to the nature of the GW generation mechanism, which is fundamentally rooted in the time-varying quadrupole moment of the mass distribution within the system [41]:

$$f_{\mathrm{GW}} = \frac{\omega_{\mathrm{GW}}}{2\pi} = \frac{2\omega}{2\pi} = 2f_{\mathrm{orbital}} \tag{46}$$

The quadrupole moment repeats itself every half orbit due to the symmetry of the system. As the system rotates by 180° the configuration looks the same from the perspective of the quadrupole moment.

As the two objects spiral closer together, the simultaneous increase in GW frequency and amplitude leads to a characteristic chirp waveform illustrated in Fig.1, detectable by observatories like LIGO and Virgo.

h_{ij}^{TT}, representing the metric perturbation in the transverse-traceless gauge, is expressed as:

$$h_{ij}^{\mathrm{TT}}(t,\mathbf{x}) = \frac{2G}{c^4D}\ddot{Q}_{ij}^{\mathrm{TT}}\left(t-\frac{D}{c}\right) \tag{47}$$

where D is the distance from the source to the observer and $t_{\mathrm{ret}} = t - D/c$ is the retarded time, which refers to the time it takes for information to propagate through space at a finite speed.

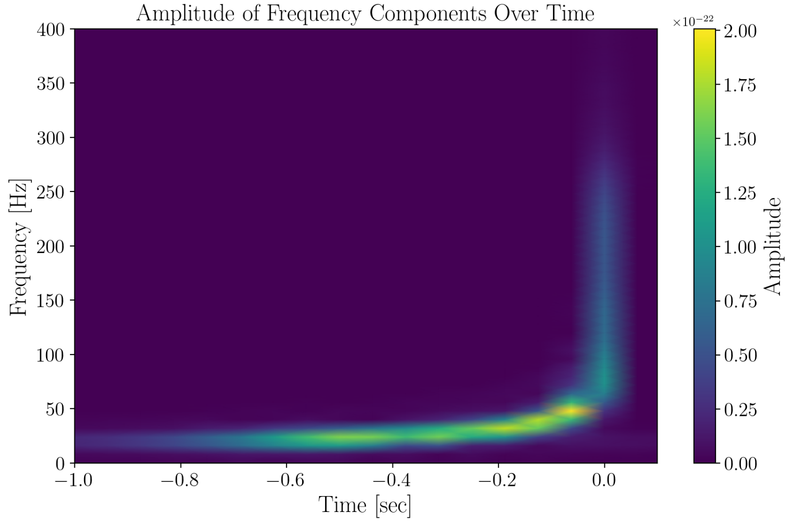

Figure 1: The amplitude of frequency $f(t)$ of the GW signal generated by a BBH merger with component masses of $35M_\odot$ and $30M_\odot$. As the binary system spirals inward due to gravitational radiation, the frequency increases steadily, producing a characteristic "chirp" signal. The frequency peaks sharply near the time of coalescence, and is associated with the rapid dynamics occurring during the merger phase.

The components h_{ij}^{TT} are:

$$h_{xx}^{\mathrm{TT}}(t) = -\frac{4G\mu r^2\omega^2}{c^4 D}\cos(2\omega t_{\mathrm{ret}}) \tag{48}$$

$$h_{yy}^{\mathrm{TT}}(t) = \frac{4G\mu r^2\omega^2}{c^4 D}\cos(2\omega t_{\mathrm{ret}}) \tag{49}$$

$$h_{xy}^{\mathrm{TT}}(t) = \frac{4G\mu r^2\omega^2}{c^4 D}\sin(2\omega t_{\mathrm{ret}}) \tag{50}$$

The strain $h(t)$ is related to the metric perturbation components:

$$h(t) = h_{ij}^{\mathrm{TT}}(t)\frac{1}{2}(\hat{u}^i\hat{u}^j - \hat{v}^i\hat{v}^j) \tag{51}$$

$$= \frac{1}{2}\left(h_{xx}^{\mathrm{TT}} - h_{yy}^{\mathrm{TT}}\right) \tag{52}$$

where the unit vectors $\hat{u}$ and $\hat{v}$ are oriented along the arms of the detector and $\hat{u} = (1, 0, 0)$, $\hat{v} = (0, 1, 0)$.

Then we will get,

$$h(t) = \frac{1}{2}\left(-\frac{4G\mu r^2\omega^2}{c^4 D}\cos(2\omega t_{\mathrm{ret}}) - \frac{4G\mu r^2\omega^2}{c^4 D}\cos(2\omega t_{\mathrm{ret}})\right) \tag{53}$$

$$= -\frac{4G\mu r^2\omega^2}{c^4 D}\cos(2\omega t_{\mathrm{ret}}) \tag{54}$$

The chirp mass is defined as:

$$\mathcal{M} = \frac{(m_1 m_2)^{3/5}}{(m_1 + m_2)^{1/5}} \tag{55}$$
$$= \mu^{3/5} M^{2/5} \tag{56}$$

and we can express $h(t)$ in terms of chirp mass and frequency:

$$h(t) = -\frac{4G^{5/3}\mathcal{M}^{5/3}\omega^{4/3}}{c^4 D}\cos(2\omega t_{\mathrm{ret}}) \tag{57}$$

The strain $h(t)$, as energy is lost from the system, the two bodies spiral inward toward each other, with the parameter measuring the fractional length change caused by a GW increasing over time. This strain is proportional to [37]:

$$h(t) \propto \frac{G^{5/3}}{c^4}\frac{\mu M^{2/3} f(t)^{2/3}}{D} \tag{58}$$

Formula 58 represents a simplified model that does not account for cosmological effects such as redshift. For distant sources, redshift can affect the observed strain and frequency, leading to modifications in the signal properties as detected by observatories.

Thus, the luminosity distance D_L to a binary system can be inferred from the GW signal [42]:

$$h \propto \frac{1}{D_L} \tag{59}$$

where D_L is defined as the distance an object needs to be to produce the observed flux given its known luminosity, assuming no cosmological effects. In cosmology, D_L is related to the redshift z of the light emitted by a distant object, expressed as [43]:

$$D_L = (1 + z) D_M \tag{60}$$

where D_M is the comoving distance, which accounts for the actual distance between two points in a universe that is expanding.

In the analysis of GWs, particularly from distant astrophysical sources, the observed frequencies are impacted by redshift, which in turn influences the inferred mass measurements of source objects such as BHs or NSs. The observed mass M_{obs} from Earth is related to the actual source mass M by the relation

$$M = (1 + z) M_{\mathrm{obs}} \tag{61}$$

This equation underscores the importance of accounting for redshift to accurately determine the intrinsic properties of the source objects.

The TT projection is influenced by the observer's direction. To simplify, we use the coordinate system is defined such that the orbital plane is oriented at an angle ι in relation to the observer's line of sight. The observer's position is described by spherical coordinates (θ, ϕ), with $\theta = \iota$ and $\phi = 0$ chosen for simplicity. The projection is given by:

$$\ddot{Q}ij^{\mathrm{TT}} = \Lambda ij, kl\ddot{Q}_{kl} \tag{62}$$

where $\Lambda_{ij,kl}$ is the projection operator:

$$\Lambda_{ij,kl} = P_{ik}P_{jl} - \frac{1}{2}P_{ij}P_{kl} \tag{63}$$

and $P_{ij} = \delta_{ij} - n_i n_j$ is the projection operator onto the plane perpendicular to the propagation direction $n = (\sin\iota, 0, \cos\iota)$.

Thus we will derive $\Lambda_{ij,kl}$ components:

$$\Lambda_{xx,xx} = P_{xx}P_{xx} - \frac{1}{2}P_{xx}P_{xx} = \frac{1}{2}P_{xx}P_{xx} = \frac{1}{2}(\cos^2\iota)^2 \tag{64}$$

$$\Lambda_{xx,yy} = P_{xy}P_{xy} - \frac{1}{2}P_{xx}P_{yy} = -\frac{1}{2}P_{xx}P_{yy} = -\frac{1}{2}\cos^2\iota \tag{65}$$

$$\Lambda_{xx,xy} = P_{xx}P_{xy} - \frac{1}{2}P_{xx}P_{xy} = \frac{1}{2}P_{xx}P_{xy} = 0 \tag{66}$$

$$\Lambda_{xy,xy} = P_{xx}P_{yy} - \frac{1}{2}P_{xy}P_{xy} = \cos^2\iota \tag{67}$$

And polarization tensors are defined as:

$$e_{+}^{ij} = \hat{e}\theta^i\hat{e}\theta^j - \hat{e}\phi^i\hat{e}\phi^j \tag{68}$$

$$e_{\times}^{ij} = \hat{e}\theta^i\hat{e}\phi^j + \hat{e}\phi^i\hat{e}\theta^j \tag{69}$$

h_{ij}^{TT} can be expressed in terms of h_+ and $h_\times$:

$$h_{ij}^{TT} = h_+ e_+^{ij} + h_\times e_\times^{ij} \tag{70}$$

The spherical basis vectors are:

$$\hat{e}\theta = (\cos\iota, 0, -\sin\iota), \quad \hat{e}\phi = (0, 1, 0) \tag{71}$$

Components of e_+^{ij} are:

$$e_+^{xx} = \hat{e}\theta^x \hat{e}\theta^x - \hat{e}\phi^x \hat{e}\phi^x = \cos^2\iota \tag{72}$$
$$e_+^{yy} = \hat{e}\theta^y \hat{e}\theta^y - \hat{e}\phi^y \hat{e}\phi^y = -1 \tag{73}$$
$$e_+^{zz} = \hat{e}\theta^z \hat{e}\theta^z - \hat{e}\phi^z \hat{e}\phi^z = \sin^2\iota \tag{74}$$
$$e_+^{xy} = e_+^{yx} = \hat{e}\theta^x \hat{e}\theta^y - \hat{e}\phi^x \hat{e}\phi^y = 0 \tag{75}$$

Like wise we can compute the components of $e_\times^{ij}$:

$$e_\times^{xy} = e_\times^{yx} = \hat{e}\theta^x \hat{e}\phi^y + \hat{e}\phi^x \hat{e}\theta^y = \cos\iota \tag{76}$$
$$e_\times^{xz} = e_\times^{zx} = \hat{e}\theta^x \hat{e}\phi^z + \hat{e}\phi^x \hat{e}\theta^z = 0 \tag{77}$$
$$e_\times^{yz} = e_\times^{zy} = \hat{e}\theta^y \hat{e}\phi^z + \hat{e}\phi^y \hat{e}\theta^z = -\sin\iota \tag{78}$$

Finally we will get the expressions for h_+ and $h_\times$ in terms of chirp mass:

$$h_+ = -\frac{4G\mu r^2\omega^2}{c^4 D}(1+\cos^2\iota)\cos(2\omega t) \tag{79}$$
$$= -\frac{4G^{5/3}\mathcal{M}^{5/3}\omega^{2/3}}{c^4 D}(1+\cos^2\iota)\cos(2\omega t) \tag{80}$$
$$h_\times = -\frac{8G\mu r^2\omega^2}{c^4 D}\cos\iota\sin(2\omega t) \tag{81}$$
$$= -\frac{4G^{5/3}\mathcal{M}^{5/3}\omega^{2/3}}{c^4 D}\cos\iota\sin(2\omega t) \tag{82}$$

Figure 2 presents the time-domain waveform of a GW emanating from a BBH system. This waveform encompasses the three fundamental phases of the BH coalescence process: inspiral, merger, and ringdown. Each phase is distinctly characterized by its unique temporal and amplitude features, providing a comprehensive depiction of the GW signal generated during the BBH interaction.

Inspiral Phase: The inspiral phase marks the initial stage of the coalescence, where the pair of BHs revolve around each other while steadily approaching closer. During this phase, the system loses energy through the emission of GWs, causing the orbital frequency and GW amplitude to increase progressively. The inspiral waveform exhibits a chirping pattern, as the BHs move closer in their spiral, the frequency and amplitude escalate.

Merger Phase: In due course, the two objects become sufficiently close to unite into a single, larger mass. This phase produces a burst of high-frequency GWs with a peak amplitude, especially in the case of BH mergers. The peak frequencies of these GWs typically lie in the range of hundreds of Hz, around 100 Hz to 1000 Hz, depending on the masses and types of the merging objects. For BH mergers, the frequencies are generally in the range of 100 Hz to a few hundreds Hz, while NS

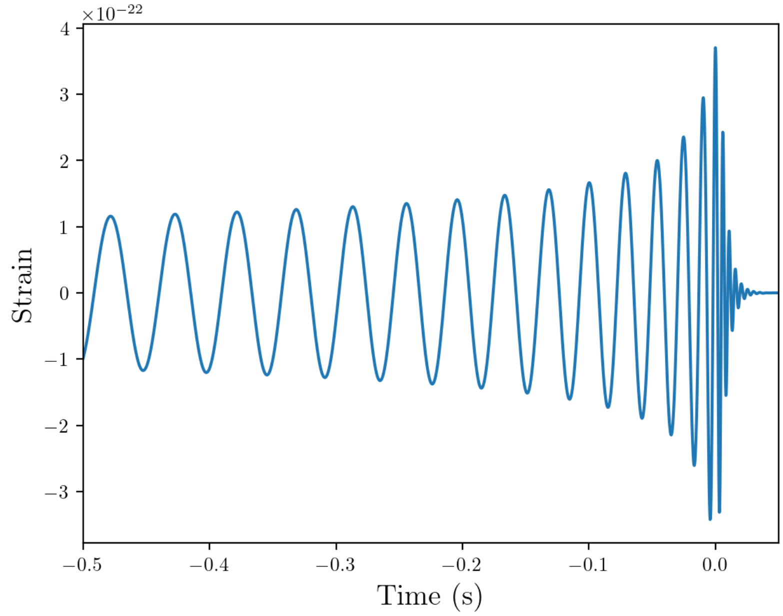

Figure 2: The GW strain h_+ over time is illustrated for a BBH merger. This system has a chirp mass of 25 $M_\odot$ at a redshift of $z = 0.5$. The orbital plane is tilted at an angle of $\theta_{\mathrm{JN}} = \pi/3$ relative to the observer's line of sight and has a polarization angle $\psi = 1.5$. The waveform was generated using the IMRPhenomXPHM approximant [44], commencing at a frequency of 10 Hz and incorporating the modes $(\ell, m) = (2,2), (2,1), (3,3), (3,2), (4,3)$.

mergers can reach frequencies up to 1 kHz or higher. The waveform during this phase reflects the highly the nonlinear behavior of spacetime curvature during the interaction of BHs merge.

Ringdown Phase: After the merger, the resulting black hole enters the ringdown phase, where it settles into a stable state. This phase is characterized by damped oscillations in the GW signal, corresponding to the emission of quasi-normal modes of the BH. The amplitude of the waveform decreases exponentially over time as the BH radiates away residual distortions, ultimately stabilizing into a Kerr black hole, which is uniquely identified by its mass and spin properties.

GWs cannot be fully described by a single harmonic; instead, they are more accurately expressed as a combination of spin-weighted spherical harmonics [45]. While the dominant contribution comes from the $\ell = 2, m = \pm 2$ harmonic, higher-order harmonics, such as the (2,1), (3,2), (3,3), and (4,4) harmonics, also carry significant power [46, 47]. The ℓ and m are quantum numbers that specify the properties and shape of the spherical harmonic function which is denoted as $Y_l^m(\theta, \phi)$. ℓ is a non-negative integer which determines the degree of the spherical harmonic, related to the number of angular nodes. m is an integer that satisfies $-\ell \leq m \leq \ell$ which determines the azimuthal variation of the spherical harmonics. As the mass ratio between the two BHs diminishes, the relevance of these additional harmonics escalates and becomes more significant during the binary system's late inspiral and merger phases.

The amplitude of the GW signal can be modified by higher-order modes and constructively or destructively be interfered with the dominant mode, leading to variations in the observed amplitude. Each mode oscillates at a frequency proportional to $m \times \omega$, where ω is the orbital frequency, so higher modes introduce higher-frequency components to the GW signal.

The GW strain $h(t)$ is formulated through a sum over various modes:

$$h(t) = \frac{1}{D} \sum_{\ell=2}^{\infty} \sum_{m=-\ell}^{\ell} h_{\ell m}(t) {-2}Y_{\ell m}(\theta, \phi) \tag{83}$$

where $h_{\ell m}(t)$ is the complex amplitudes of the modes, dependent on the source dynamics, $-2Y_{\ell m}(\theta, \phi)$ is the spin-weighted spherical harmonics, which encode how each mode $h_{lm}(t)$ varies with the observer's angular position (θ, ϕ).

Each $h_{lm}(t)$ can be further broken down:

$$h_{\ell m}(t) = A_{\ell m} e^{-im\Phi(t)} \tag{84}$$

$$A_{\ell m}(t) \approx \omega^{2-l} \tag{85}$$

for higher order modes ($\ell > 2$), $A_{\ell m}$ is suppressed by negative powers of ω. Generally, $A_{\ell m}$ decreases as the multipole order ℓ increases, and vary with the azimuthal number m, though this dependence is typically less pronounced than that on ℓ.

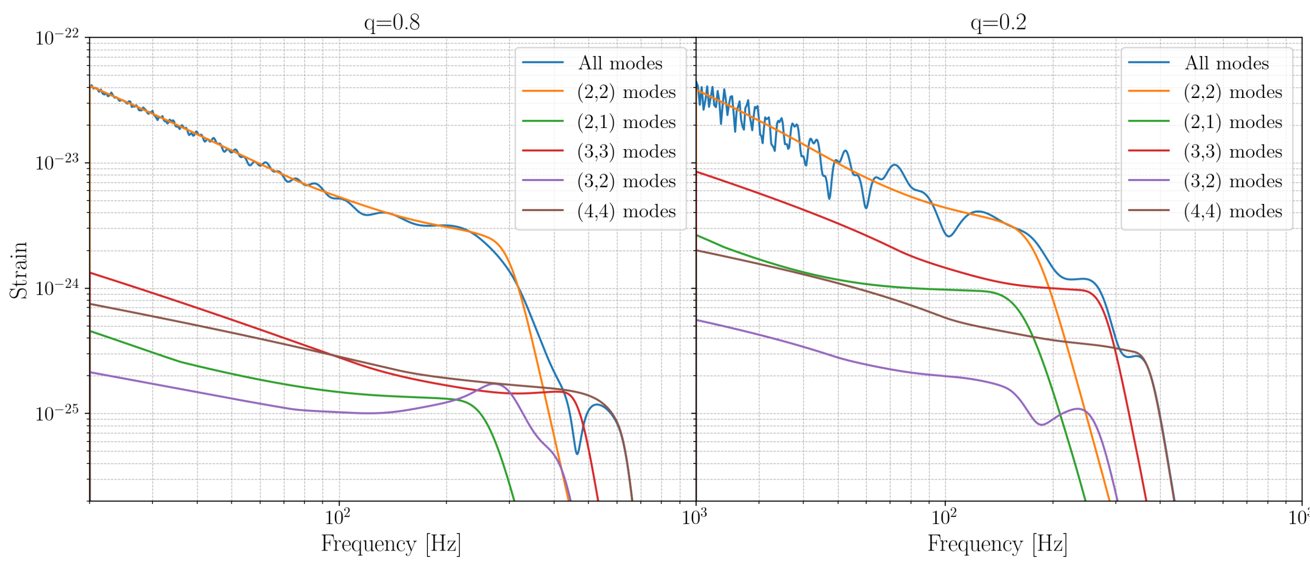

Figure 3: GW strain in frequency domain for two different mass ratios in binary coalescence. The left panel shows the strain for a mass ratio $q = 0.8$ and the right panel for a mass ratio $q = 0.2$. Different colored lines represent the strain of GW under various modes.

Fig.3 shows the GW strain containing different modes as a function of frequency for mass ratios $q = 0.8$ and $q = 0.2$. The waveform is dominated by $(2, 2)$ mode, and higher order modes are less essential compared to the dominant mode. For $q = 0.2$, higher order modes contributes more compared to higher mass ratio $q = 0.8$. The higher order modes introduce oscillations in the total strain, highlighting the effect of asymmetry in the system.

To detect GWs, we need a theoretical framework. This involves solving the EFEs in a way that applies to many matter systems. The solution must explain how GWs are emitted and propagated. It must also account for how these waves affect their source [10]. Solving this problem exactly in GR is almost impossible for most sources. Instead, we rely on approximation methods. The PN approximation is widely regarded as the standard approach [48]. It is crucial for analyzing GWs from inspiraling compact binaries. This requires a detailed understanding of the equations of motion and the radiation field at high PN orders.

The PN expansion approximates the EFE by expanding them in powers of v/c. Each order in expansion corresponds to a successive correction to Newtonian gravity:

$$g_{\mu\nu} = g_{\mu\nu_{\text{Newtonian}}} + \epsilon^1 \, g_{\mu\nu_{1\text{PN}}} + \epsilon^2 \, g_{\mu\nu_{2\text{PN}}} + \dots \tag{86}$$

where $\epsilon = (v/c)^2$.

In the PN framework, the perturbation is expressed as:

$$h_{\mu\nu} = \sum_{n=1}^{\infty} (\frac{v}{c})^n h^n_{\mu\nu} \tag{87}$$

the order n refers to the $n/2$-PN term.

At 0PN order (Newtonian Approximation), the dynamics are governed by Newton's laws of gravitation, recovering the Possion equation for the gravitational potential Φ:

$$\nabla^2 \Phi = 4\pi G\rho \tag{88}$$

and the metric is approximately:

$$ds^2 = -(1 + \frac{2\Phi}{c^2})c^2 dt^2 + (1 - \frac{2\Phi}{c^2})d\mathrm{x}^2 \tag{89}$$

And at 1PN order, the effects of general relativity start to appear. Corrections account for factors such as time dilation, perihelion precession, and gravitational redshift [10]. Corrections to the metric $g_{\mu\nu}$ include terms of $\mathcal{O}(v^2/c^2)$, and for example the time-time component of the metric becomes:

$$g_{00} = -(1 + \frac{2\Phi}{c^2} + \frac{2\Phi^2}{c^4}) \tag{90}$$

The total energy E of the system is corrected by relativistic terms:

$$E = -\frac{Gm_1 m_2}{2r}(1 + \text{PN terms}) \tag{91}$$

2PN order includes further corrections to the motion and gravitational field, including the spin-

spin interactions [49]. 2.5PN order is inclusion of radiation reaction effects, where the energy carried away by GWs is considered, leading to inspiral due to gravitational radiation. Moreover, 3PN order and higher includes even finer corrections that might be necessary for high-precision modelling or when dealing with systems with strong fields and high velocities.

The leading-order power radiated by GWs is given by Eq.44 and at 2.5PN order, due to energy being lost through GW emission, the orbit of the binary system shrinks, and the rate at which the orbital radius r changes is determined by [39]:

$$\frac{dr}{dt} = -\frac{64}{5}\frac{G^3 m_1 m_2 (m_1 + m_2)}{c^5 r^3} \tag{92}$$

The waveform of GWs from CBC can be described using Post-Newtonian expansion:

$$h(t) = A_+ \left[\frac{\pi f_{gw}(t)}{c}\right]^{2/3} \cos\left[\Phi(f_{gw}(t)) + \Phi_0\right] + A_\times \left[\frac{\pi f_{gw}(t)}{c}\right]^{2/3} \sin\left[\Phi(f_{gw}(t)) + \Phi_0\right] \tag{93}$$

where $\Phi(f_{gw})$ and $f_{gw}(t)$ are known up to 3.5PN order.

The gravitational waveform $h(t)$ is contingent upon the chirp mass $\mathcal{M}$ of the binary system, which is the most important parameter in the gravitational waveform because it determines the leading order amplitude and frequency evolution of the GWs. It appears at the 0PN order in the waveform [10].

The symmetric mass ratio η enters at the 1PN order and affects higher-order terms in the expansion. It is critical in determining PN corrections to the gravitational waveform's phase [50].

$$\eta = \frac{m_1 m_2}{(m_1 + m_2)^2}, \tag{94}$$

The compact objects' angular momentum is described by their dimensionless spins $\chi_{1,2}$. Spin effects begin at 1.5PN order. Spin-orbit coupling affects the phase at 1.5PN, and spin-spin interactions contribute at 2PN [51].

$$\chi_{1,2} = \frac{c\mathrm{S}_{1,2}}{Gm_{1,2}^2} \tag{95}$$

where $\mathrm{S}_{1,2}$ is the angular momentum of the compact objects.

It is defined as the projection of the individual spins along the orbital angular momentum, weighted by their masses, the effective spin parameter χ_{eff} enters at the 1.5PN order [52]:

$$\chi_{\text{eff}} = \frac{m_1 \chi_1 \cos\theta_1 + m_2 \chi_2 \cos\theta_2}{m_1 + m_2} \tag{96}$$

Spin's impact on the waveform additionally relies on the mass ratio of the binary compact objects. Starting from the 1PN order and higher, the mass ratio q influences both the system's dynamics and the waveform characteristics.

$$q = \frac{m_2}{m_1} \tag{97}$$

Parameters that shape the signal's amplitude and phase at the detector are adjusted during the matched-filter search. These are further refined through thorough parameter estimation analysis. [53].

When one or both of the merging compact objects are not BHs, the orbital dynamics are significantly affected. In such scenarios, each star is distorted by the tidal field generated by its companion, which extracts energy from the orbit and induces a quadrupole moment that enhances GW emission. This effect is particularly relevant in BNS systems.

To first approximation, the induced quadrupole moment Q_{ij} scales with the tidal field σ_{ij} and is defined by:

$$Q_{ij} = -\lambda\sigma_{ij} \tag{98}$$

where λ signifies the tidal deformability.

The tidal deformability is contingent upon the equation of state (EOS) and the star's mass, and it is expressed as:

$$\Lambda = \frac{\lambda}{m^5} \sim \left(\frac{R}{m}\right)^5 \tag{99}$$

where R and m denote the star's radius and mass, respectively.

Thus, less massive NSs, which have larger deformability, are easier to measure. Specifically, the tidal deformability Λ is given by:

$$\Lambda = \left(\frac{2}{3}\right) k_2 \left[\left(\frac{c^2}{G}\right)\left(\frac{R}{m}\right)^5\right],$$

In this context, k_2 stands for the second Love number, while R refers to the stellar radius. For realistic NSs, k_2 typically ranges from 0.05 to 0.15. BHs, on the other hand, are expected to have $k_2 = 0$, meaning this tidal effect is absent for them [30].

NSs are thought to form from explosive supernova events caused by the implosion of iron cores in large stars. A widely accepted scenario begins with a binary system of two massive stars (8–25 $M_\odot$). The larger star undergoes a supernova explosion, resulting in the formation of a NS. This NS and the companion star enter a "common envelope" phase, where the NS orbits within the extended layers of the secondary star. Later, the second star also undergoes a supernova. If the stars remain gravitationally bound after both explosions, a BNS system forms [54]. Observations confirm the existence of BNS systems, but their exact formation is not fully understood. Another proposed pathway is "dynamical capture," where two isolated NSs interact in dense regions like globular clusters. This often leads to BNS systems with high orbital eccentricities.

The inspiral phase, where the stars spiral towards each other due to gravitational-radiation losses, is largely unaffected by magnetic fields or neutrinos and has been extensively studied through a combination of numerical simulations and analytical calculations based on PN expansions or other approximation methods.

The result of the merger is determined by the total mass of the binary M in comparison to the maximum mass of a non-rotating NS M_{TOV}. Depending on this mass ratio, the merger can lead to several outcomes: the system can immediately collapse into a BH with a surrounding torus. Alternatively, it may form a hypermassive or supramassive NS that later collapses into a BH. If the total mass is below the critical limit, a stable NS may form instead.

During the late stages of inspiral, tidal forces become so strong that tidal waves are generated on the stellar surfaces, accompanied by the emission of matter and the formation of shocks. These shocks are generated by small sound waves originating in the stars' central regions, which steepen as they travel outward into areas of lower density. During the merger, the stars collide with a significant impact parameter, resulting in a vortex sheet where the tangential velocity component is discontinuous. This setup is susceptible to the Kelvin-Helmholtz instability (KHI), potentially giving rise to vortices across a range of wavelengths. An initially poloidal magnetic field can cause the KHI to exponentially amplify the toroidal magnetic field component, the magnetic field within a core-collapse supernova can undergo significant amplification, increasing by approximately three orders of magnitude. High-resolution simulations of such supernovae reveal that parasitic instabilities play a crucial role in this process by suppressing the Magneto-Rotational Instability (MRI). The suppression of MRI by these instabilities effectively limits the extent of magnetic field growth, resulting in a magnetic field amplification factor of around 100. Importantly, this amplification factor remains largely independent of the initial magnetic field strength, suggesting that the underlying mechanism governing this process is robust across varying initial conditions.

2.3 Detection of gravitation waves

The GW detector generate a time series signal, reflecting the state of oscillation of a resonant mass or the phase change in light that is recombined from the two arms of the interferometer [39]. It contains a mix of the true GW signal and noise [39].

$$s(t) = h(t) + n(t) \tag{100}$$

Here, $s(t)$ represents the aggregate signal captured by the detector, $h(t)$ denotes the GWsignal, and $n(t)$ stands for the detector's noise. For ease of analysis, the time-domain signals $s(t)$, $h(t)$, and $n(t)$ are converted into the frequency domain via the Fourier transform.:

$$\tilde{s}(f) = \int_{-\infty}^{\infty} s(t) e^{-2\pi i f t} dt \tag{101}$$

$$\tilde{h}(f) = \int_{-\infty}^{\infty} h(t)e^{-2\pi ift}dt \tag{102}$$

$$\tilde{n}(f) = \int_{-\infty}^{\infty} n(t)e^{-2\pi ift}dt \tag{103}$$

The noise is modeled as a stationary Gaussian random process with an average of zero. Its statistical characteristics are defined by the noise power spectral density (PSD) $S_n(f)$ [55], which is given by [56]:

$$\langle \tilde{n}^*(f)\tilde{n}(f') \rangle = \delta(f - f')\frac{1}{2}S_n(f) \tag{104}$$

Here, $\langle \cdot \rangle$ represents an ensemble average, and $\delta(f - f')$ denotes the Dirac delta functio, which ensures that the expression is only non-zero when $f = f'$. It describes the auto-correlation function of the noise in the frequency domain.

To detect $h(t)$ in $s(t)$, we construct a matched filter $Q(t)$ that maximize the SNR [57]. The matched filter is defined as the correlation of $s(t)$ with a template $h(t)$:

$$z = \int_{-\infty}^{\infty} s(t)h(t)dt \tag{105}$$

In the frequency domain, this becomes:

$$z = 4Re\int_{0}^{\infty} \frac{\tilde{s}(f)\tilde{h}^*(f)}{S_n(f)}df \tag{106}$$

where $\tilde{h}^*(f)$ is the complex conjugate of the signal template in the frequency domain, and $S_n(f)$ weights the contribution of each frequency according to the detector's sensitivity.

The SNR, denoted by ρ, quantifies the likelihood of signal detection, which is defined as:

$$\rho = \frac{\langle z \rangle}{\sigma_z} \tag{107}$$

where $\langle z \rangle$ is the expected value of the matched filter output when a signal is present, and σ_z is the standard deviation of z due to noise.

The expected value is:

$$\langle z \rangle = 4Re\int_{0}^{\infty} \frac{|\tilde{h}(f)|^2}{S_n(f)}df \tag{108}$$

The noise-induced variance σ_z^2 of the filter output is given by:

$$\sigma_z^2 = 4\int_{0}^{\infty} \frac{|\tilde{h}(f)|^2}{S_n(f)}\,df$$

Thus, the SNR becomes:

$$\rho^2 = 4\int_0^\infty \frac{|\tilde{h}(f)|^2}{S_n(f)} df \tag{109}$$

The GWsignal $h(t)$ detected by an observatory is a superposition of two distinct polarization modes, $h_+(t)$ and $h_\times(t)$, each modulated by the detector's response functions, $F_+(\theta,\phi,\psi)$ and $F_\times(\theta,\phi,\psi)$:

$$h(t) = h_+(t)F_+(\theta,\phi,\psi) + h_\times(t)F_\times(\theta,\phi,\psi) \tag{110}$$

These independent polarizations, $h_+(t)$ and $h_\times(t)$, are governed by the intrinsic properties of the binary system. The detector's sensitivity to each polarization is contingent upon its orientation relative to the source. The response functions F_+ and $F_\times$ are specifically influenced by three key parameters: θ, which represents the inclination angle of the source relative to the detector; ϕ, the azimuthal position of the source with respect to the detector; and ψ, the polarization angle of the GW [58].

The mathematical expressions for the response functions are as follows:

$$F_+(\theta,\phi,\psi) = \frac{1}{2}(1+\cos^2\theta)\cos 2\phi\cos 2\psi - \cos\theta\sin 2\phi\sin 2\psi \tag{111}$$

$$F_\times(\theta,\phi,\psi) = \frac{1}{2}(1+\cos^2\theta)\cos 2\phi\cos 2\psi + \cos\theta\sin 2\phi\sin 2\psi \tag{112}$$

A single detector measures an output $h(t)$, which, as described by Eq.110, depending on the two functions $h_{+,\times}(t)$, and the angles (θ,ϕ,ψ) [59]. To resolve these quantities, coincident observations from a network of detectors are required. Using three interferometers, five quantities can be measured: the three signals $h_i(t)$ $(i = 1, 2, 3)$ and two independent time delays. These measurements enable the determination of $h_+(t)$, $h_\times(t)$, θ, ϕ, and ψ.

Each LIGO site houses a single Advanced LIGO detector [60]. The detector records GW strain by measuring the difference in length between two perpendicular arms. Each arm, made up of mirrors acting as test masses, is 4 km in length. As a gravitational wave traverses the detector, it alters the lengths of its arms, resulting in a measured difference of $\Delta L(t) = \delta L_x - \delta L_y = h(t)L$. In this equation, $h(t)$ represents the GW strain amplitude as projected onto the detector, and L is the unperturbed arm length [15].

LIGO was designed as a facility capable of supporting multiple generations of detectors. After an initial period of scientific data collection and incremental upgrades to the original LIGO detectors, the Advanced LIGO (aLIGO) upgrade began in 2010. The aLIGO detectors started operations in 2015 during the first observing run (O1) [61]. These advanced detectors are sensitive to GWs at frequencies as low as 10 Hz, although achieving this sensitivity is extremely challenging in practice. They offer a tenfold increase in sensitivity across the frequency band. This marks a significant improvement compared to the 40 Hz lower cutoff frequency of the initial LIGO detectors [60]. Between the O1 and O3 observing runs, substantial upgrades were made. These enhancements extended the angle-averaged BNS range to over 100 Mpc for LIGO H1 and 125 Mpc for LIGO L1.

The forth observing run(O4) is divided into two phases: O4a and O4b. The improvements made to the detectors include upgrades to the optical systems to surpass the quantum noise sensitivity limits and isolation of noise sources within the vacuum chambers [62, 63].

Looking forward, LIGO is expected to undergo several upgrades to further increase its sensitivity, allowing it to detect a greater number and variety of GW events. In parallel, other detectors such as the European Virgo [24] and the Japanese KAGRA [64, 65] observatories are contributing to a global network that will enhance localization and parameter estimation of GW sources. Additionally, plans for next-generation detectors like the Einstein Telescope and the space-based LISA mission promise to open new windows into the universe, detecting GWs from sources currently beyond LIGO's reach.

Virgo [66] is an interferometric GW detector situated in Italy, with 3 km long arms and a design optimized for detecting signals in the low-frequency range. The Advanced Virgo project [67] introduced upgrades that significantly enhanced its sensitivity. Advanced Virgo commenced data collection on August 1, 2017, collaborating with the two LIGO interferometers during the latter part of the O2 run, achieving a sensitivity equivalent to a BNS inspiral range of approximately 30 Mpc.

Virgo made its first GW detection with the event GW170814 [68]. This event, which was also observed by both LIGO interferometers, represented the first triple detection of a GW signal. Only three days later, the three detectors observed GW170817 [30], a binary NS merger that heralded the advent of multi-messenger astronomy.

KAGRA [64, 65] stands out from LIGO and VIRGO due to two technological innovations: Firstly, KAGRA is located deep underground to reduce seismic disturbances; secondly, its test masses consist of sapphire mirrors designed to function at cryogenic temperatures (approximately $20K$) to lower thermal noise. As a result, KAGRA is expected to attain sensitivity levels comparable to those of ALIGO and Virgo, reaching $2 \times 10^{-24}/\sqrt{\mathrm{Hz}}$ at 100 Hz. The designed sensitivity corresponds to a BNS range of 140 Mpc.

The plot 4 illustrates the amplitude spectral density (ASD) of five GW detectors in relation to frequency, representing the square root of the power spectral density (PSD).

$$A(f) = \sqrt{S(f)} \tag{113}$$

The detectors represented in the plot include Advanced LIGO (aLIGO) from its fourth (O4) observing runs, Virgo during its fourth (O4) and fifth (O5) observing runs, and KAGRA at 80 Mpc sensitivity which is used in O5 runs, and A+ from its O5 runs. The PSD is a key metric in evaluating the sensitivity of GW detectors across different frequencies, with lower values indicating higher sensitivity.

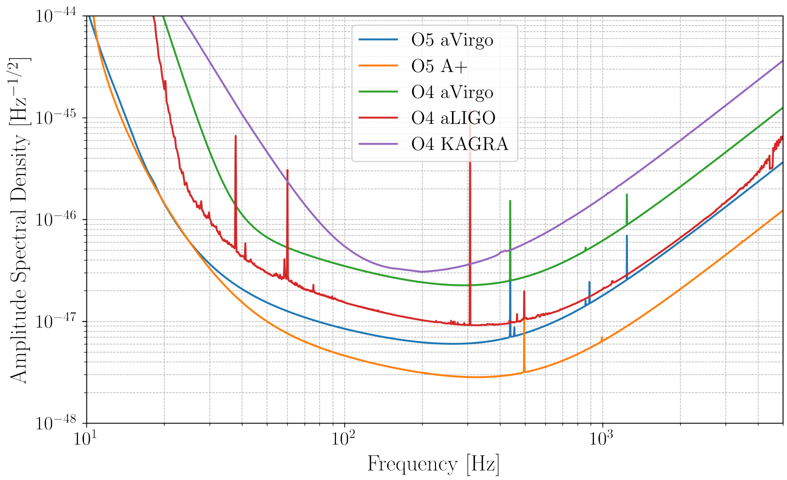

Figure 4: The amplitude spectral density (ASD) of five GW detectors across the frequency domain, based on publicly available noise curve data. The plot illustrates the sensitivity of each detector as a function of frequency. The selected detection runs include: O5 simulations using Virgo and A+, O4 simulations using Virgo, LIGO and KAGRA.

In this plot, the x-axis represents the frequency in Hz, while the y-axis shows the ASD in units of $\mathrm{Hz}^{-1/2}$. It highlights the improvements made in detector sensitivity across different observing runs and the comparison between different detectors. For instance, the A+ O5 and Advanced Virgo O5 runs demonstrate significant advancements in sensitivity compared to earlier runs, particularly at lower frequencies where sensitivity improvements are crucial for detecting BNS mergers and other low-frequency GW sources.

Fig.4 is essential for understanding the performance and limitations of each detector, guiding the development of future upgrades and the interpretation of GW data from these observatories.

GW detection is an extremely sensitive process, and LIGO must contend with various noise sources, including seismic activity, thermal noise, and quantum noise. LIGO employs several strategies to mitigate these effects, such as suspending the mirrors on quadruple pendulums to isolate them from seismic vibrations and using high-power lasers to reduce quantum noise. Additionally, the detectors are located at separate sites, which allows for cross-correlation of signals to distinguish true GW events from local noise.

GW detectors are influenced by various noise sources, but the sensitive frequency band is primarily determined by three key types of noise. Fig. 5 provides a comprehensive visualization of how different types of noise affect the sensitivity of GW detectors across various frequency ranges.

The seismic noise is given by:

$$S_{\text{seismic}}(f) = A_{\text{seismic}}\left(\frac{f}{f_{\text{ref}}}\right)^{-2} \tag{114}$$

where $S_{\text{seismic}}(f)$ is the PSD of seismic noise at frequency f, and A_{seismic} is the baseline amplitude of seismic noise at a reference frequency (typically chosen based on the local seismic activity and

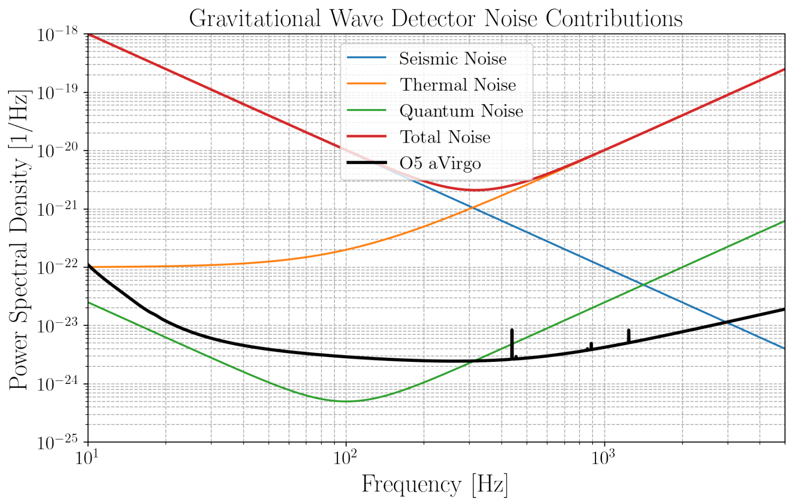

Figure 5: Power Spectral Density (PSD) for Advanced Virgo in the 5th run, illustrating the contribution of three key types of noise: Seismic Noise, Thermal Noise, and Photon Shot Noise. Seismic Noise: (blue line) dominates at low frequencies (below 10 Hz), where ground vibrations are most significant. It decreases approximately with f^{-2} as frequency increases, due to isolation systems designed to reduce ground motion. Thermal Noise: (orange line) dominated by mirror coatings and suspensions, especially around 30–500 Hz. The frequency $f_0 = 100$ Hz serves as a reference for the resonant behavior of thermal noise, which increases as f^2 beyond f_0. Quantum Noise: (green line) combines shot noise at high frequencies (due to photon counting uncertainty) and radiation pressure noise at low frequencies (from photon momentum fluctuations impacting the mirrors). These two effects create a characteristic “U-shaped” noise curve. The Total Noise: (red line) represents the combined effect of all noise sources, determining the overall sensitivity of the detector to GWs.

the isolation system's performance). In this case, we chose 10^{-18}. f_{ref} is the reference frequency, often set to 10 Hz.

The thermal noise in the coatings and suspensions is usually described by a model that includes a resonance frequency, the PSD is:

$$S_{\text{thermal}}(f) = A_{\text{thermal}}(1 + \frac{f}{f_0}^2) \tag{115}$$

where A_{thermal} is the baseline amplitude of thermal noise, typically derived from material properties and the design of the suspension system, in this case, we chose 10^{-22}. f_0 is the resonance frequency, often set around 100 Hz, where thermal noise peaks due to resonance effects.

The quantum noise consists of two main components: radiation pressure (dominant at low frequencies) and shot noise (dominant at high frequencies). It is often modeled as:

$$S_{\text{quantum}}(f) = A_{\text{quantum}}((\frac{f_{\text{low}}}{f})^2 + (\frac{f}{f_{\text{high}}})^2) \tag{116}$$

where A_{quantum} is influenced by the laser power and interferometer optics, here, we set to 10^{-24},

f_{low} represents the frequency where radiation pressure noise becomes significant (typically around 50 Hz), f_{high} represents the frequency where shot noise becomes dominant (around 200 Hz).

And the total noise is:

$$S_{\text{total}}(f) = S_{\text{seismic}}(f) + S_{\text{thermal}}(f) + S_{\text{quantum}}(f) \tag{117}$$

Photon shot noise is one of the primary noise sources in laser interferometric detectors. This noise originates from the light source and results from fluctuations in the interference pattern monitored for GW signals. Since photon interference follows a Poisson process, it produces variations referred to as photon shot noise. At high frequencies, the sensitivity of the detector is constrained by this noise, which depends on the number of photons collected—a factor influenced by both the laser power and the GW frequency. To mitigate photon shot noise, increasing laser power and employing power recycling techniques, which recover light escaping through the symmetric output port, can be effective. However, increasing the laser power introduces a trade-off, as it can lead to increased radiation pressure on the mirrors, which in turn limits the sensitivity at low frequencies.

The second major noise source is thermal noise, which is caused by the vibrations of the detector components due to heat. This type of noise is particularly impactful in the mid-frequency range (around 100 Hz). To mitigate thermal noise, LIGO and Virgo have focused on selecting materials with low internal losses. KAGRA, on the other hand, has implemented a cryogenic system that cools its mirrors to approximately 20K, significantly reducing thermal noise through successful cryogenic operations.

The third type of noise is seismic noise, which originates from the vibrations of the ground. The Earth is constantly in motion due to various factors, and these vibrations are further influenced by the surrounding environment. To address seismic noise, sophisticated vibration isolation systems have been developed. These systems are designed to suppress seismic vibrations by several orders of magnitude, thereby extending the detector's sensitivity down to frequencies around 10 Hz, while still maintaining the necessary control over the mirrors.

Ground-based detectors such as LIGO, Virgo [24], and KAGRA [64, 65] are highly sensitive to GWs in the frequency range of approximately 10 Hz to several kHz. These detectors are well-suited for observing events such as BBH mergers and NS collisions. However, they are limited by terrestrial noise sources, including seismic vibrations and atmospheric disturbances, which restrict their sensitivity at lower frequencies.

Alternatively, the Laser Interferometer Space Antenna (LISA), a space-based detector, is set to operate in a significantly lower frequency range, from 0.1 mHz to 1 Hz. LISA will comprise three spacecraft arranged in an equilateral triangle with arm lengths measuring millions of kilometers. The configuration is designed to detect GWs from a variety of sources, including supermassive black hole (SMBH) mergers, extreme mass ratio inspirals (EMRIs), and potentially primordial GWs that could have originated in the early universe. The absence of terrestrial noise sources will enable LISA to explore a different range of astrophysical phenomena, complementing the discoveries made by ground-based detectors.

3 Gravitational Lensing

As GWs propagate across cosmological distances, they interact with the cosmological expansion and inhomogeneities in the universe [58]. Galaxies and galaxy clusters can act as gravitational lenses. This results in multiple images of the GW signal, time delays, and phase shifts. Detecting lensed signals is essential to avoid biases in binary parameter estimation. These signals also affect cosmological measurements. One method to identify lensing is to analyze the entire GW population statistically [58]

With the designed sensitivities for Advanced LIGO and Virgo, it is expected that between $1.3^{+0.6}_{-0.4}$ to $1.7^{+0.9}_{-0.6}$ detections of BBH lensed by galaxies could occur annually [69]. The addition of the KAGRA [70, 71] and LIGO-India [72] detectors to the network will enhance these prospects. Moreover, third-generation detectors, like the Cosmic Explorer (CE) [73] and the Einstein Telescope (ET) [74], are expected to have sensitivities an order of magnitude better than the current detector network, potentially enabling the observation of hundreds of thousands of mergers per year. Despite these advances, our understanding of the universe remains constrained by the sensitivity of our detectors. Fortunately, the largest structures in the Universe, such as galaxies or clusters of galaxies, can act as massive magnifying glasses, allowing us to observe objects at much greater distances. Through the gravitational lensing effect, we have been able to detect the most distant galaxies at redshifts of $z \approx 13$ and even individual stars at $z \approx 6$ [75]. In these cases, the light from stars can be amplified by a factor of more than $\mu \sim 10^4 - 10^5$. Gravitational lensing thus provides an opportunity to explore the distant universe, revealing sources that would otherwise be too faint to detect.

3.1 Geometric optics

If we consider all possible paths from a source S to an observer located at O, as shown in Fig.6, each path defines a path integral. This integral measures the time taken for light to travel from S to O when emitted at a fixed time. According to Fermat's principle, the travel time is extremized for paths that correspond to actual light rays. In the following discussion, we assume the existence of angular diameter distances. These distances relate the proper distance at the source to the angle it subtends at the observer, as is the case in a homogeneous cosmological model [76].

The angular diameter distances between the observer and the source is denoted by d_{OS}, the observer is represented by d_{OL} and the lens is expressed as d_{LS}, and the lens and the source [1]. The angular position of the source in the sky, θ_S, represents the direction from which a ray would have been observed if no lens were present. As the ray passes through the lens plane, it is deflected

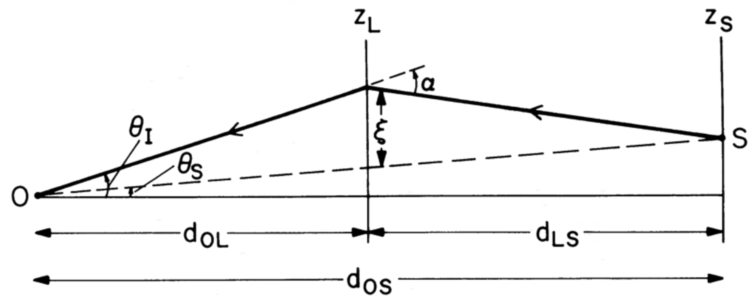

Figure 6: The plot is from Blandford's work, which shows a ray originating from the source S, located at a redshift z_s, is deflected by a gravitational angle α as it travels past the lens at redshift z_L before reaching the observer O. The observed image is positioned at an angular coordinate θ_I, measured relative to a reference direction. In the absence of the lens, the source would be seen at the angular position θ_S [76]

by an angle α, leading it to reach the observer from the direction θ_I [76].

The lens equation relates θ_S to the θ_I due to the deflection caused by the lensing mass is

$$\theta_S = \theta_I - \alpha(\theta_I) \tag{118}$$

and the defection angle $\alpha(\theta_I)$ is derived from the gravitational potential $\psi(\theta_I)$ of the lens:

$$\alpha(\theta_I) = \nabla\psi(\theta_I) \tag{119}$$

where

$$\psi(\theta_I) = \frac{1}{\pi}\int \kappa(\theta\prime)\ln|\theta_I - \theta\prime| d^2\theta\prime \tag{120}$$

and $\kappa(\theta\prime)$ is convergence, defined as the dimensionless surface mass density, represents the isotropic focusing of light rays due to the mass density of the lens, is expressed as:

$$\kappa = \frac{1}{2}\nabla^2\psi \tag{121}$$

We consider the lensing mass distribution to be confined within a thin layer positioned between the source at redshift z_s and the observer. This distribution is characterized by a projected two-dimensional density on a lens plane at redshift z_L. Light propagation paths are described by null geodesics in the uniform background universe, traveling from S to points on the lens plane, and then continuing as null geodesics from the lens plane to O. These paths are parameterized by the two-dimensional angular coordinate θ_I, representing the ray's direction at O, relative to an arbitrarily defined origin, typically chosen as the center of the lens [76].

For any given path, there are two sources of time delay. The first is the geometrical time delay, which arises from the extra path length that light travels when it is deflected from a background geodesic by a massive object. The second is the gravitational time delay, which results from the local distortion of spacetime caused by the mass of the lens.

Under the small-angle approximation, the geometrical time delay caused by the additional path length of the deflected ray, compared to the direct path from the source (S) to the observer (O), is measured by an observer in the lens plane as $\alpha\xi/2$. Here, we use units where $c = G = 1$ and define $\xi = (\theta_I - \theta_S)d_{OL}$ [77].

The time delay is given by:

$$t_{\text{geom}}(\theta_I; \theta_S) = \frac{(1 + z_L)d_{OL}d_{OS}}{2d_{LS}}(\theta_I - \theta_S)^2 \tag{122}$$

The gravitational time delay in the observer frame is [78]:

$$t_{\text{grav}}(\theta_I) = -2(1 + z_L)\int ds\psi(\theta_I) \tag{123}$$

where the integral is along the line of sight.

The total time delay is obtained by adding the geometrical and gravitational contributions [77]:

$$\tau(\theta_I; \theta_S) = \frac{1}{2}|\theta_I - \theta_S)|^2 - \psi(\theta_I) \tag{124}$$

where $\tau(\theta_I; \theta_S)$ is the time surface.

According to Fermat's principle, for a given source position θ_S, the locations of the images correspond to the stationary points of $\tau(\theta_I; \theta_S)$ with respect to variations in θ_I. In the absence of any intervening mass, $\tau(\theta_I; \theta_S)$ forms a paraboloid, and the single image appears at the minimum, where $\theta_I = \theta_S$. As mass is gradually introduced, the arrival time surface is elevated, and new extrema emerge, corresponding to additional images [79].

The scaled (extrinsic) curvature tensor [79]:

$$K_{ij} = \tau_{ij} = \delta_{ij} - \frac{\partial^2\psi}{\partial\theta_{Ii}\partial\theta_{Ij}} = \frac{\partial\theta_{Si}}{\partial\theta_{Ij}} \tag{125}$$

K_{ij} is the Hessian of the transformation $\theta_I \to \theta_S$. The Jacobian matrix K_{ij} describes how small changes in the image position map to changes in the source position.

Defined as the flux ratio between a lensed image and its corresponding unlensed source, the magnification μ is calculated by taking the inverse of the Jacobian matrix K_{ij}'s determinant:

$$\mu = \frac{1}{|\det(K)|} \tag{126}$$

For a two-dimensional lens plane, the Jacobian matrix can be written as:

$$\mathcal{K} = \begin{pmatrix} 1-\kappa-\gamma_1 & -\gamma_2 \\ -\gamma_2 & 1-\kappa+\gamma_1 \end{pmatrix}$$

where γ_1 and γ_2 represent the anisotropic distortion of images (being stretched or squeezed), they are defined as:

$$\gamma_1 = \frac{1}{2}(\frac{\partial^2\psi}{\partial\theta_{I_1}^2} - \frac{\partial^\psi}{\partial\theta_{I_2}^2}) \tag{127}$$

$$\gamma_2 = \frac{\partial^2\psi}{\partial\theta_{I_1}\partial\theta_{I_2}} \tag{128}$$

The magnification formula is:

$$\mu = \frac{1}{|(1-\kappa)^2 - (\gamma_1^2+\gamma_2^2)|} \tag{129}$$

Rewriting in terms of the eigenvalues ρ_1 and ρ_2, the magnification can be written as

$$\mu = (\kappa^2 - \mu^2)^{-1} \tag{130}$$

where $\kappa = 1/2(\rho_1^{-1} + \rho_2^{-1})$ is the expansion, and $\mu = 1/2(\rho_1^{-1} - \rho_2^{-1})$ is the shear.

The principal radii of curvature of the time-delay surface, ρ_1 and ρ_2, are utilized to determine the parity of the image. In gravitational lensing, the parity of a lensed image describes its orientation relative to the source, indicating whether the image is inverted or retains the same orientation. The partial parities of the image are defined by the signs of ρ_1 and ρ_2, while the total parity is determined by the sign of the product $\rho_1\rho_2$. At the minimum of the time-delay surface, both partial parities and the total parity are positive. At a maximum, the partial parities are negative, but the total parity remains positive. For a saddle point, the total parity is negative, and the partial parities have opposite signs [76].

In the absence of a lens, there exists a single image with positive parity. The introduction of lensing mass generates additional images in pairs, each with opposite parity. Furthermore, the earliest image always possesses positive partial parities and, therefore, a positive total parity; in other words, the first image to form must carry the majority parity. Images with positive partial parities contain more flux than the original source, whereas those with negative partial parities are associated with rays passing through regions where the mass density exceeds the critical density [76].

When the gravitational field of a massive object, such as a galaxy or galaxy cluster, bends the path of light (or other electromagnetic radiation) from a distant source, the gravitational lensing happens. This bending of light can produce multiple images of the same astronomical object, each differing in position, magnification, and time delay relative to one another. These multiple images are categorized into three distinct types—Type I, Type II, and Type III—based on their time delays in comparison to a reference event [80].

Image Classification Based on Time Delays: The classification into Type I, Type II, and Type III images corresponds to the nature of their respective time delays. Specifically:

- Type I: These images are associated with the minimum time delay. They typically appear brighter and are often referred to as the ”primary” images.
- Type II: These images correspond to saddle points in the lensing potential and exhibit intermediate time delays. They are sometimes called ”saddle-point” images.
- Type III: These images are linked to maximum time delays and are generally fainter, often termed ”secondary” images.

The parity of an image refers to the orientation of its image relative to the source. Type I and Type III images exhibit positive parity, meaning they maintain the original orientation of the source. In contrast, Type II images display negative parity, resulting in a mirror-image or inverted orientation relative to the source. This distinction in parity is crucial for understanding the distortion and magnification effects induced by gravitational lensing.

In the context of GWs, phase shifts play a significant role in the observed waveform's characteristics. Type II images experience a phase shift of $\pi/2$, which differs from the phase shifts observed in Type I and Type III images, which undergo phase shifts of 0 and π radians, respectively [81]. These phase shifts arise due to the differing paths and gravitational potentials traversed by the GWs as they form each image type.

The distinctive $\pi/2$ phase shift experienced by Type II images leads to observable distortions when compared to unlensed images. These distortions manifest as alterations in the amplitude and phase of the GW signal, making Type II images particularly notable for their unique imprint on the waveform [80]. Such distortions are instrumental in identifying and classifying lensed GW events, as they provide critical information about the lensing mass distribution and the geometry of the lensing configuration.

In cases where GW signals are dominated by the fundamental harmonics (specifically the $(2, \pm 2)$ modes). Through adjustments to parameters like the coalescence phase or polarization angle, Type I or unlensed GW signals can emulate these distortions introduced by gravitational lensing [58]. However, for signals that include significant contributions from higher harmonics, precession, or orbital eccentricity, these lensing-induced distortions cannot be accurately reproduced by Type I signals alone [58]. In such instances, incorrectly assuming that a detected signal is unlensed can lead to considerable biases in the inferred astrophysical parameters. Moreover, these complex lensed signals might be missed by the conventional LIGO-Virgo search algorithms [82, 58].

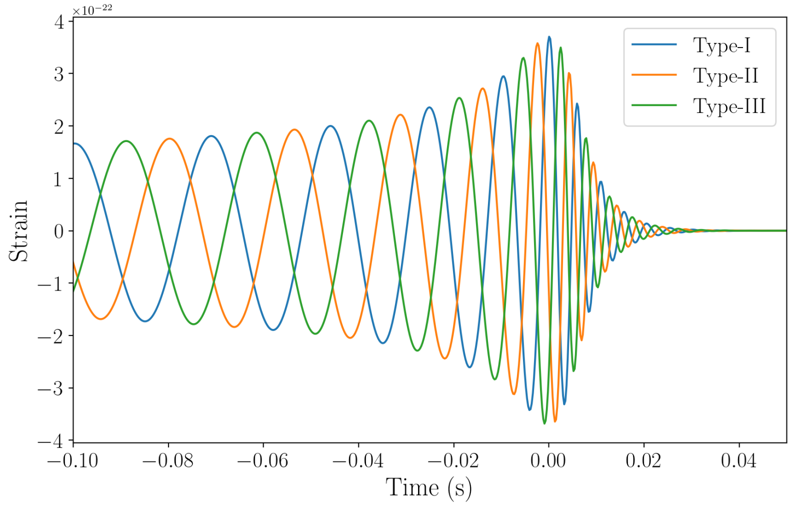

Figure 7: Time-domain waveforms of the h_+ polarization strain for three types of lensed GW signals: Type-I (blue), Type-II (orange), and Type-III (green).

Fig.7 illustrates the time-domain waveforms of the h_+ polarization strain for three types of lensed GW signals: Type-I (blue), Type-II (orange), and Type-III (green). These waveforms, representing different lensing scenarios, exhibit the characteristic phases of a compact binary coalescence—namely inspiral, merger, and ringdown. While the overall shapes of the waveforms are similar, the Type-II and Type-III signals display noticeable phase shifts. These variations, caused by gravitational lensing, highlight the impact of lensing on the observed signals, affecting the apparent time of arrival and phase. Understanding these distortions is crucial for accurately interpreting lensed GW events.

3.2 Wave optics

Ground-based detectors are presently investigating frequencies between 10 Hz and 10 kHz. On the other hand, space-based observatories like LISA are designed to function within the 0.1 mHz to 100 mHz range, while DECIGO targets frequencies from 1 mHz up to 100 Hz.These frequency ranges correspond to GW wavelengths of $10^4\,\mathrm{m} < \lambda < 10^7\,\mathrm{m}$ for ground-based detectors and $10^6\,\mathrm{m} < \lambda < 10^{12}\,\mathrm{m}$ for space-based detectors [83]. Therefore, when the Schwarzschild radius of the deflectors is comparable to λ, the wave optics regime becomes essential [1].

The perturbed space-time line element due to the lens is described by

$$ds^2 = -(1+2U)dt^2 + (1-2U)dr^2 = g_{\mu\nu}dx^\mu dx^\nu \tag{131}$$

In this equation, $U(r)$ represents the Newtonian gravitational potential associated with the lens. The disturbance in the background metric $g_{\mu\nu}$ caused by the GWs is given by $h_{\mu\nu} = \phi e_{\mu\nu}$ [84]. Since the null geodesic is the path along which the polarization tensor $e_{\mu\nu}$ is parallel transported, its variation can be ignored, permitting the examination of the scalar wave's propagation equation as shown below [1]:

$$(\nabla^2 + \omega^2)\tilde{\phi} = 4\omega^2 U \tilde{\phi} \tag{132}$$

In the phenomenon of gravitational lensing, the bending of a wave induced by the lens's gravitational potential is considered to occur instantaneously, a premise known as the thin-lens approximation. This simplification is valid because the cosmological distances separating the lens, source, and observer vastly exceed the actual size of the area where lensing occurs [77]. Under this model, the mass of the lens is projected onto a two-dimensional surface, termed the lens plane [1].

As a waveform interacts with a gravitational lens, its path and amplitude are distorted. In the absence of lensing, the wave's amplitude is described by $\tilde{\Phi}_0(r) = Ae^{i\omega r}/r$. Consequently, the lens-induced amplitude is defined as [1]

$$F(\boldsymbol{r}) = \frac{\tilde{\Phi}(\boldsymbol{r})}{\tilde{\Phi}_0(\boldsymbol{r})} \tag{133}$$

Rewriting the propagation equations using F leads to [78]:

$$\frac{\partial^2 F}{\partial r^2} + 2i\omega \frac{\partial F}{\partial r} + \frac{1}{r^2}\nabla_\theta^2 F = 4\omega^2 U F \tag{134}$$

Provided that $\omega/|\partial \ln F/\partial r| \sim$ (the characteristic length over which F changes) divided by the wavelength is much larger than one, the first term can be omitted. Consequently, Equation 155 resembles the Schrödinger equation [79]. Specifically, the amplification factor can be computed by solving the relevant path integral formulated from the classical Lagrangian [1], hence,

$$F(r_0) = \int \mathcal{D}\theta(r) \exp\left\{ i \int_0^{r_0} dr L[r, \theta(r), \dot{\theta}(r)] \right\} \tag{135}$$

Equation 135 employs the standard methodology introduced by Feynman and Hibbs [85] alongside the thin lens approximation [1], and can be expressed as:

$$F(r_0) = \left[\prod_{j=1}^{N-1} \int \frac{d^2\theta_j}{A_j} \right] \exp\left\{ i\omega \left[\epsilon \sum_{j=1}^{N-1} \frac{r_j r_{j+1}}{2} \left| \frac{\theta_j - \theta_{j+1}}{\epsilon} \right|^2 - \hat{\psi}(\theta_L) \right] \right\} \tag{136}$$

The initial $l - 1$ integrals are Gaussian in nature, and the remaining terms can similarly be transformed into Gaussian integrals, and the final result is Kirchhoff diffraction integral [86]:

$$F(r_0) = \frac{\omega}{2\pi i} \frac{D_L D_S}{D_{LS}} \int d^2\theta \exp\left\{ i\omega \left[\frac{D_L D_S}{2D_{LS}} |\theta - \beta|^2 - \hat{\psi}(\theta) \right] \right\} \tag{137}$$

In this context, θ represents the angular distance between the lens and the observed image, while β denotes the angle between the observer's line of sight to the source's true position and the lens.

The symbols D_L corresponds to the distances to the lens, D_S represents the distance to the source, and D_{LS} denotes the distacne between the lens and the source, respectively [77, 1].

Within Eq. 137, the first component inside the square brackets denotes the geometrical delay. This delay arises from the difference in the distance traveled by the direct, unlensed path from the source to the observer compared to the lensed path that passes through the lens plane at an angle θ. The second component accounts for the gravitational time delay resulting from the gravitational potential of the lens [1].

Detectable gravitational lensing events are thought to occur when the source, lens, and observer are roughly in alignment, and the source lies within the Einstein radius of the lens [77, 1].

$$\theta_E = \sqrt{4GM_L \frac{D_{LS}}{D_L D_S}} \equiv \sqrt{2R_S \frac{D_{LS}}{D_L D_S}}. \tag{138}$$

where R_S is the Schwarzschild radius of the lens. Einstein radius sets the scale of strong lensing phenomenon [79], thus we can obtain:

$$x = \frac{\theta}{\theta_E}; \quad y = \frac{\beta}{\theta_E}; \quad w \equiv \omega(1+z_L)\frac{D_S D_L}{D_{LS}}\theta_E^2; \quad \psi = \frac{1}{1+z_L}\frac{D_{LS}}{D_S D_L}\frac{1}{\theta_E^2}\hat{\psi} \tag{139}$$

x is the dimensionless position of the image, y is the impact parameter, ω is the dimensionless frequency, and ψ is the lens potential [78].

Within the framework of geometric optics, the formation of images occurs at the stationary points of the time delay function:

$$x_\pm = \frac{1}{2}\left|y \pm \sqrt{y^2+4}\right| \tag{140}$$

$$T_\pm(y) = \frac{1}{4}\left[y^2 + 2 \mp y\sqrt{y^2+4}\right] - \ln x_\pm - \ln\theta_E \tag{141}$$

Here, the shared delay term for both images, $(-\ln\theta_E)$, is generally disregarded. Furthermore, the dimensionless diffraction integral will be written as [86]:

$$F(w,y) = \frac{w}{2\pi i}\int d^2x\, e^{iwT_\pm(y)} \tag{142}$$

The analytical expression for a point mass lens is:

$$F(w,y) = \exp\left(\frac{\pi w}{4} - i\frac{w}{2}\ln\left(\frac{w}{2}\right)\right)\Gamma\left(1-\frac{iw}{2}\right){}_1F_1\left(\frac{iw}{2},1;\frac{iwy^2}{2}\right) \tag{143}$$

- $\Gamma(z)$: Gamma function.
- ${}_1F_1(a,b;z)$: Confluent hypergeometric function (Kummer's function).

- y: Dimensionless impact parameter, representing the source's position relative to the lens.
- w: Dimensionless frequency, defined as:

$$w = \frac{4\pi GMf}{c^3} \tag{144}$$

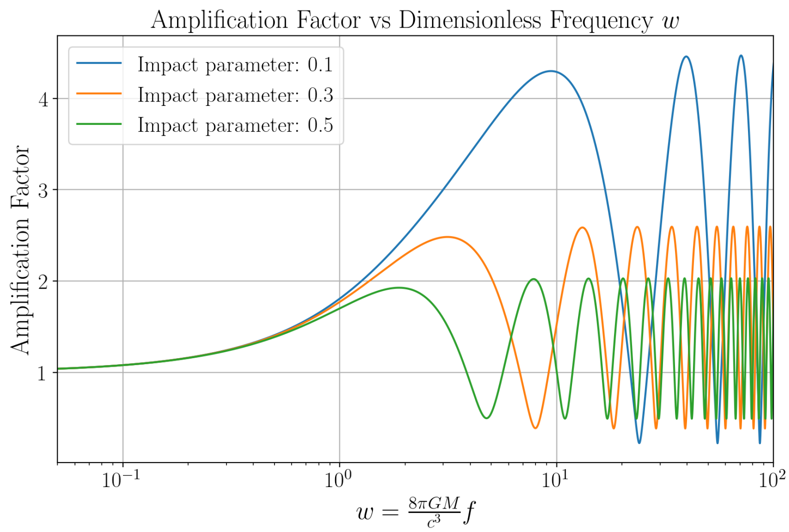

Figure 8: The amplification factor changes with the dimensionless frequency for wave optics waveform. The impact parameters are 0.1, 0.3, 0.5. The lens mass is 500 $M_\odot$.

Fig.8 illustrates the frequency-dependent amplification factor in wave optics. As the frequency increases, the amplification factor begins at 1 for lower values of w, representing no amplification. As w increases, the amplification factor gradually rises and begins to oscillate, indicating the interference effects characteristic of wave optics. This behavior highlights how GWs, when lensed, can experience variations in amplitude due to the wave nature of light, resulting in constructive and destructive interference patterns as seen in the oscillations.

Fig.9 and Fig.10 compares the normalized frequency-domain waveforms and amplitudes of the h_+ polarization for wave optics and the unlensed GW signals. The wave optics signal shows distortions compared to the unlensed signal, particularly noticeable as the GWs interfere with each other. This interference causes an increase in amplitude, emphasizing the effects of wave optics, which differ from the predictions of geometric optics. The plot clearly demonstrates that GWs in the wave optics regime can exhibit enhanced amplitudes and complex structures due to lensing effects, which are not present in the geometric optics limit.

4 Parameter Estimation

Parameter estimation (PE) is the process of using sample data to estimate the values of parameters that define a statistical model or distribution for a population. Simply put, it involves finding

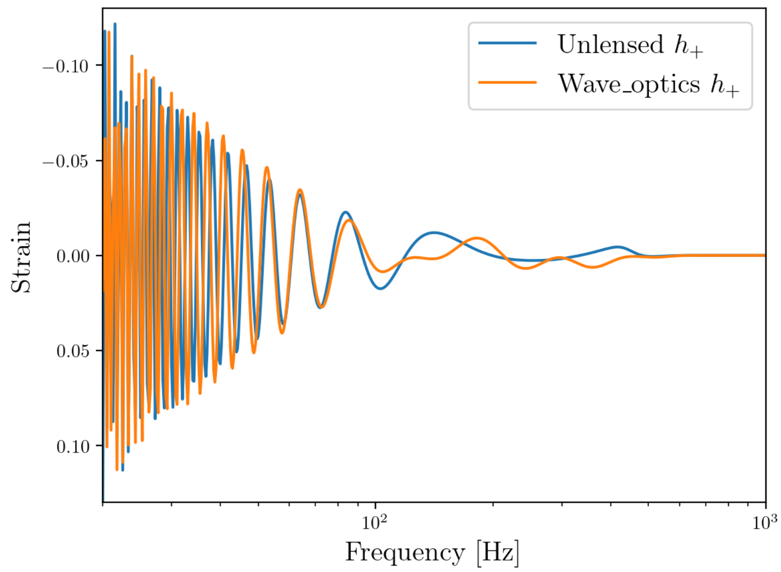

Figure 9: The normalized waveforms for wave optics (orange) and unlensed waveform (blue) in frequency domain. The lens mass is 500 $M_\odot$, and the impact parameter is 0.3.

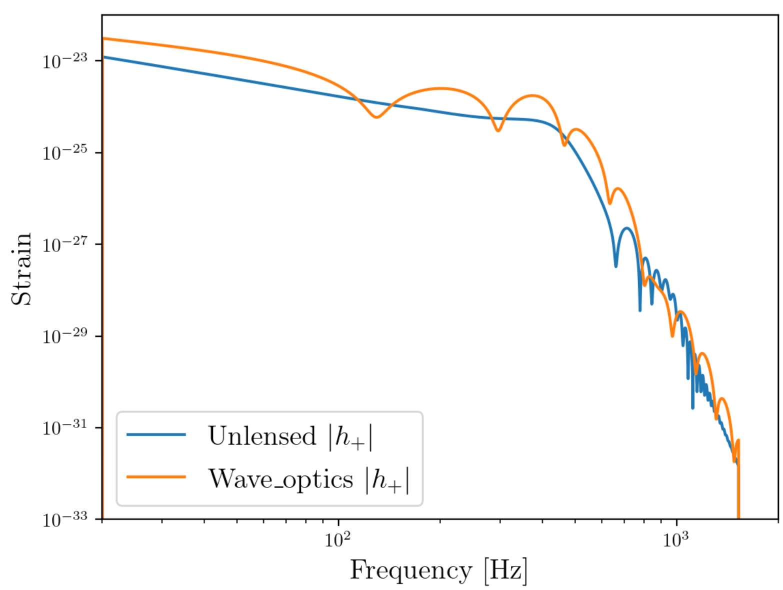

Figure 10: The strain amplitude in h_+ polarization as a function of frequency.

numerical values for these parameters that best describe the data collected from observations [87].

In GW astronomy, parameter estimation is used to determine the properties of astrophysical sources, such as BBHs or NSs, that generate GWs detected by observatories like LIGO and Virgo [88]. These parameters typically include the masses and spins of the binary components, luminosity distance, orbital parameters, sky location, merger time, and phase [89].

GW parameter estimation relies on comparing observed data to theoretical waveforms. Bayesian inference is commonly used, combining prior information about possible parameter values with the likelihood of the observed signal given each set of parameters [90]. Accurate models of GW signals, known as waveform templates, are essential for this process. These waveforms depend on the source parameters and are matched against the detected signal. By finding the waveform template that best fits the data, we can estimate the most possible values of the source parameters.

For Bayesian parameter estimation, tools like Bilby [91] and LALInference [92] are widely used. Algorithms such as Markov Chain Monte Carlo (MCMC) and Nested Sampling [55] are popular for efficiently exploring the high-dimensional parameter space [93] The result of parameter estimation is often a posterior distribution for each parameter, describing the interval of values that match the observed data, allowing scientists to quantify uncertainties in the estimated source properties.

4.1 Bayesian inference

To estimate the parameters of a model based on observed data, Bayesian inference is a robust method, and it is rooted in Bayes' theorem. Bayes' theorem connects the conditional probability of event A occurring given that event B has happened, expressed as:

$$\mathbb{P}(A \mid B) = \frac{\mathbb{P}(B \mid A)\mathbb{P}(A)}{\mathbb{P}(B)} = \frac{\mathbb{P}(B \mid A)\mathbb{P}(A)}{\mathbb{P}(B \mid A)\mathbb{P}(A) + \mathbb{P}(B \mid A^c)\mathbb{P}(A^c)}. \tag{145}$$

In a practical scenario, such as medical diagnostics, A may represent the event of a patient having a particular disease, while A^c represents the event of the patient not having the disease. Similarly, B denotes the event of a diagnostic test yielding a positive result. The likelihood is given by $\mathbb{P}(B \mid A)$, and the prior probability of A is denoted by $\mathbb{P}(A)$. Bayes' theorem facilitates the transformation of the prior probability into the posterior probability $\mathbb{P}(A \mid B)$ upon the evidence of B [94]. Within the Bayesian framework, uncertainty regarding unknown parameters is expressed through probabilities, treating the parameters as random variables.

Bayes' theorem allows us to express the posterior probability density $p(\boldsymbol{\theta} \mid d)$ for a parameter set $\boldsymbol{\theta}$ given data d as:

$$p(\boldsymbol{\theta} \mid d) = \frac{\pi(\boldsymbol{\theta})\mathcal{L}(d \mid \boldsymbol{\theta})}{\mathcal{Z}(d)}, \tag{146}$$

where $\pi(\boldsymbol{\theta})$ denotes the prior probability density, $\mathcal{L}(d \mid \boldsymbol{\theta})$ represents the likelihood of observing the data d given the parameters $\boldsymbol{\theta}$, and $\mathcal{Z}(d)$ is the evidence [55].

The evidence, also referred to as the marginal likelihood, is defined as [55]:

$$\mathcal{Z}(d) = \int d\boldsymbol{\theta}\, \pi(\boldsymbol{\theta})\mathcal{L}(d \mid \boldsymbol{\theta}), \tag{147}$$

which normalizes the posterior distribution, ensuring that it integrates to one over the parameter space.

The likelihood function is a choice we make. It describes the measurement process. Defining a likelihood implicitly establishes a noise model. In GW astronomy, this noise is generally considered to follow a Gaussian distribution. This assumption leads to a likelihood function of the following form [55].,

$$\mathcal{L}(d|\theta) = \frac{1}{2\pi\sigma^2} \exp\left(-\frac{1}{2}\frac{|d-\mu(\theta)|^2}{\sigma^2}\right) \tag{148}$$

Here, $\mu(\theta)$ represents a template for the gravitational strain waveform parameterized by θ, while σ denotes the detector noise level. Note that π without any subscripts or parentheses refers to the mathematical constant (approximately 3.14159) and not a prior distribution. The normalization factor does not include a square root because d is typically complex, reflecting a two-dimensional Gaussian distribution, namely the Whittle likelihood. This likelihood function reflects the assumption that the noise in GW detectors follows a Gaussian distribution.

The choice of prior, like the likelihood function, is also a subjective decision. The prior distribution $\pi(\theta)$ encodes our prior knowledge or assumptions about θ before performing any measurements. In certain contexts, there is a natural choice for the prior. For instance, when considering the sky location of a BBH merger [55], an isotropic prior that assigns equal probability to every point on the sky is a reasonable choice. In other situations, selecting an appropriate prior is less straightforward. For instance, before the first detection of GWs, determining a suitable prior for the primary BH mass, $\pi(m_1)$, would have been challenging. In cases where we have little to no prior knowledge about θ, a common practice is to use a uniform or log-uniform distribution to express this uncertainty [55].

Although θ may consist of many parameters, we are often interested in only a subset of them. In the analysis of GW signals, understanding the posterior distribution is crucial for parameter estimation. An example is the posterior distribution for a BBH merger, which may be a fifteen-dimensional function integrating data on BH masses, their positions in the sky, spins, and other relevant parameters. This high-dimensional distribution allows for a comprehensive characterization of the merger event, facilitating accurate inference of the BHs' properties. To extract the posterior distribution for the primary mass, we perform marginalization by integrating over the parameters of no interest, often called "nuisance parameters" [55].

The posterior probability density $p(\theta_i|d)$ for parameter θ_i given data d is obtained by integrating over all other parameters:

$$p(\theta_i|d) = \int \left(\prod_{k\neq i} d\theta_k\right) p(\theta|d) = \frac{\mathcal{L}(d|\theta_i)\,\pi(\theta_i)}{\mathcal{Z}} \tag{149}$$

Here, $\mathcal{L}(d|\theta_i)$ denotes the marginalized likelihood, defined as:

$$\mathcal{L}(d|\theta_i) = \int \left(\prod_{k\neq i} d\theta_k\right) \pi(\theta_k)\mathcal{L}(d|\theta) \tag{150}$$

When integrating out a variable θ_α to determine the posterior for θ_β, the resulting estimate for θ_β

incorporates the uncertainty associated with θ_α. If θ_α and θ_β are correlated, marginalizing over θ_α increases the uncertainty in the posterior distribution of θ_β. Consequently, the marginalized posterior $p(\theta_\beta|d)$ becomes more spread out compared to the conditional posterior $p(\theta_\beta|d, \theta_\alpha)$. The conditional posterior corresponds to a specific slice of $p(\theta_\beta|d)$, evaluated at a fixed value of θ_α [55].

In Bayesian model comparison, the evidence $\mathcal{Z}$ plays a pivotal role. For two competing hypotheses, $\mathcal{H}_1$ and $\mathcal{H}_2$, the odds ratio $\mathcal{O}_2^1$ is defined as the ratio of their respective evidences. When $\mathcal{O}_2^1 \gg 1$, it indicates strong preference for model $\mathcal{H}_1$ over $\mathcal{H}_2$, and the opposite holds true when the ratio is much smaller than one. This ratio of evidences is also referred to as the Bayes factor, which serves as a measure of the relative likelihood of one model being supported by the data compared to the other.

In practical terms, Bayesian evidence is represented as a single numerical value. By itself, it typically has little interpretive value, but it becomes meaningful when compared to the evidence of another model. The evidence is formally defined as a likelihood function, specifically the fully marginalized likelihood. It is expressed as $\mathcal{L}(d)$, which is independent of θ. Bayesian evidence is also a critical tool for model selection. In the context of BBHs, we may compare a "signal model," which assumes the presence of a BBH signal in the data with a prior $\pi(\theta)$, to a "noise model," which assumes no BBH signal. The signal model has 15 binary parameters. The noise model, however, has no parameters [55]. Consequently, the signal evidence and noise evidence are defined as:

$$\mathcal{Z}_S \equiv \int d\theta \mathcal{L}(d|\theta)\pi(\theta) \tag{151}$$

$$\mathcal{Z}_N \equiv \mathcal{L}(d|0) \tag{152}$$

Bayes factor is

$$BF_N^S \equiv \frac{\mathcal{Z}_S}{\mathcal{Z}_N} \tag{153}$$

and in the log form is

$$\log \mathrm{BF}_N^S \equiv \log(\mathcal{Z}_S) - \log(\mathcal{Z}_N) \tag{154}$$

A large absolute value of $\log \mathrm{BF}$ suggests a strong preference for one model compared to the other. A commonly used threshold of $|\log \mathrm{BF}| = 8$ is considered as providing "strong evidence" in support of one hypothesis compared to another. Similarly, Bayes factors can be computed to compare identical models but with differing priors.

Bayesian evidence conveys two important insights. First, it evaluates how well the model aligns with the observed data through the likelihood. Second, marginalization reveals the effective parameter space utilized during the fitting process.

With the development of phenomenological GWforms, predicting the expected data d for a given set of parameters θ has become computationally straightforward. However, calculating the posterior probability for the 15 parameters describing a BBH merger remains computationally challenging. For example, creating a grid with ten bins in each dimension and evaluating the likelihood at every grid point would require 10^{15} likelihood evaluations, making the process computationally infeasible due to the curse of dimensionality. To address this, stochastic samplers are employed. Commonly used sampling techniques fall into two main categories: The algorithms Markov-chain Monte Carlo and nested sampling produce sets of posterior samples $\{\theta\}$. These samples are extracted from the posterior distribution such that the density of samples in the range $(\theta, \theta + \Delta\theta)$ aligns proportionally with $p(\theta)$ [55].

$$\langle f(x) \rangle_{p(x)} = \int dx\, p(x) f(x) \approx \frac{1}{n_s} \sum_{k}^{n_s} f(x_k) \tag{155}$$

In this context, $p(x)$ represents the posterior distribution being sampled, $f(x)$ is the function whose expectation value is to be computed, and the summation over k spans n_s posterior samples [95].

In summary, Bayesian inference furnishes a comprehensive framework for examining GW data, enabling precise parameter estimation and model comparison. With the increase in the number of observed events, the methods described here will become even more crucial for understanding the underlying physics of GW sources and the broader cosmological implications.

4.2 Methods

4.2.1 Markov Chain Monte Carlo (MCMC)

A significant challenge in Bayesian posterior computation, especially when dealing with a high-dimensional parameter space, is solving complex integration problems. While these problems can be analytically addressed using low-dimensional numerical integration or Gaussian-based approximations [96], high-dimensional cases often require simulation-based computational techniques such as MCMC or nested sampling [93].

In MCMC methods, particles traverse the posterior distribution via a random walk. The likelihood of transitioning to a specific point is determined by the Markov chain's transition probabilities. By recording the positions of these particles, often called walkers, at each step, samples are extracted from the posterior probability distribution [97].

For sampling from a target probability density function $p(\boldsymbol{\theta} \mid \mathbf{d})$, the Monte Carlo technique of rejection sampling is one approach. In this method, a candidate parameter set $\boldsymbol{\theta}^* \sim q(\boldsymbol{\theta})$ is generated from a proposal probability density function $q(\boldsymbol{\theta})$, which is chosen to majorize the target distribution. This means that $p(\boldsymbol{\theta} \mid \mathbf{d}) \leq M q(\boldsymbol{\theta})$ for all $\boldsymbol{\theta}$ and some constant $M > 0$. The candidate $\boldsymbol{\theta}^*$ is accepted with a probability:

$$\alpha = \frac{p(\boldsymbol{\theta}^* \mid \mathbf{d})}{M q(\boldsymbol{\theta}^*)}, \tag{156}$$

and otherwise, it is rejected, prompting the generation of a new candidate. The acceptance probability is $1/M$, indicating that the rejection method is efficient when M is close to 1. However, in high-dimensional spaces, it becomes difficult to find a proposal density that is sufficiently close to the target distribution to maintain efficiency [98].

The Metropolis-Hastings (MH) algorithm extends rejection sampling by generating dependent samples instead of independent ones, thereby avoiding the need for a majorizing proposal density. The algorithm starts with an initial parameter set $\boldsymbol{\theta}_0$. A new candidate $\boldsymbol{\theta}^* \sim q(\boldsymbol{\theta} \mid \boldsymbol{\theta}_0)$ is proposed, where the proposal distribution $q(\boldsymbol{\theta} \mid \boldsymbol{\theta}_0)$ can depend on the current state $\boldsymbol{\theta}_0$ and does not need to majorize the target distribution. The candidate $\boldsymbol{\theta}^*$ is accepted with probability:

$$\alpha(\boldsymbol{\theta}_0) = \min\left\{1, \frac{p(\boldsymbol{\theta}^* \mid \mathbf{d})}{p(\boldsymbol{\theta}_0 \mid \mathbf{d})} \cdot \frac{q(\boldsymbol{\theta}_0 \mid \boldsymbol{\theta}^*)}{q(\boldsymbol{\theta}^* \mid \boldsymbol{\theta}_0)}\right\}, \tag{157}$$

where $M(\boldsymbol{\theta}_0)$ is the ratio of the target densities at $\boldsymbol{\theta}^*$ and $\boldsymbol{\theta}_0$, adjusted by the proposal densities. When the candidate is accepted, the new state becomes $\boldsymbol{\theta}_1 = \boldsymbol{\theta}^*$; otherwise, the Markov chain remains at the previous state, $\boldsymbol{\theta}_1 = \boldsymbol{\theta}_0$. This process generates a Markov chain that, under mild conditions on the proposal distribution, converges to the target posterior distribution $p(\boldsymbol{\theta} \mid \mathbf{d})$ [99, 100].

4.2.2 Nested Sampling

Nested sampling, introduced by John Skilling [93], is a computational technique initially designed for calculating the evidence, or marginal likelihood, in Bayesian models. Over time, it was discovered that this method also produces samples from the posterior distribution as a natural by-product [101]. By weighting each sample according to its posterior probability, nested sampling effectively converts these into posterior samples.

This method systematically explores the parameter space by focusing on regions with higher likelihood values, making it particularly effective for problems with complex likelihood landscapes, such as those with multiple peaks or difficult integrals [102]. As the algorithm progresses, it incrementally refines the regions of interest, efficiently estimating the evidence while concurrently generating posterior samples.

Nested sampling is an important method used in Bayesian inference, especially when dealing with parameter spaces that have a large number of dimensions. The process starts by initializing the parameter space with a set of "live points," which are drawn from the prior distribution [93]. During each iteration, the point with the smallest likelihood is eliminated, and a new sample is generated until one with a higher likelihood is discovered. The algorithm then computes the Bayesian evidence by associating a prior volume with each eliminated point. The evidence is determined by summing the product of the likelihood and prior volume for each sample. This process is repeated iteratively until the algorithm converges, resulting in an efficient estimation of both the Bayesian evidence and the posterior distributions. This method is particularly useful for models where the parameter space is complex and multidimensional.

Nested sampling offers the significant benefit of being able to estimate an upper bound on the evidence at each step of the algorithm. This is done by assuming that the remaining prior volume has a likelihood matching the highest likelihood found among the current live points [93]. This upper bound estimate is crucial for deciding when to stop the algorithm, specifically when the ongoing evidence estimate exceeds a predetermined fraction of this bound [55].

On the downside, unlike MCMC approaches, nested sampling does not parallelize efficiently, and the collection of posterior samples does not grow linearly with the amount of computational time invested. This makes it a more computationally intensive approach, but its efficiency in exploring complex likelihood landscapes can outweigh these drawbacks in certain applications [101].

4.3 Parameter estimation for binary black holes

Matched filtering technique assumes the form of $h(t)$ is known, however, in practise, $h(t)$ depends on several free parameters. Therefore, a family of possible waveforms or templates are considered. Consequently, there exists a corresponding family of optimal filters $K(t;\theta)$. The θ-space must be discretized and the filtering procedure be repeated in practise. Starting with the prior distribution $p^{(0)}(\theta_t)$, the posterior probability distribution for the true parameter value θ_t is determined based on the observed data s, the PDF is:

$$p(\theta_t|s) = \mathcal{N}\, p^{(0)}(\theta_t) \exp\left\{ \langle h_t|s\rangle - \frac{1}{2}\langle h_t|h_t\rangle \right\} \tag{158}$$

where $\mathcal{N}$ is the normalization factor.

The GW strain $h(t)$, as depicted in Eq. 110, is a multifaceted function that encapsulates various parameters defining both the source's intrinsic properties and its orientation relative to the observer. These parameters include:

- Distance to the Source (r): The strain amplitude $h(t)$ is inversely proportional to the distance r between the GW source and the observer. This relationship implies that more distant sources produce weaker GW signals, while closer sources yield stronger detections.

- Source Location Angles (θ, ϕ): The celestial coordinates (θ, ϕ) specify the position of the GW source in the sky relative to the observer. These angles are integral to the pattern functions, which modulate the GW strain based on the source's location, affecting the observed amplitude and phase of the waveform.

- Orbital Orientation: Two angles define the orientation of the binary system's orbital plane in relation to the observer's line of sight:

1. Inclination Angle (ι): This angle measures the tilt of the binary's orbital plane relative to the observer. An inclination of $\iota = 0$ degrees indicates a face-on orientation, while $\iota = 90$ degrees corresponds to an edge-on view. The inclination angle significantly influences the polarization and amplitude of the GW signal.

2. Polarization Angle: This angle determines the orientation of the plus (h_+) and cross ($h_\times$) polarization axes relative to a fixed coordinate system on the sky. It affects how the GW polarizations are projected onto the detector's arms, thereby influencing the observed waveform.

- Reference Time (t_*): The reference time t_* denotes the moment when the GW signal enters the detector's sensitive frequency band. This parameter is embedded within the phase $\Phi(t)$ and the GW frequency $f_{\rm gw}(t)$, dictating the signal's timing and frequency evolution as it is recorded by the detector.

- Constant Phase (φ): The constant phase offset φ sets the initial phase of the GW waveform. This phase factor is crucial for accurately aligning the theoretical waveform with the observed signal, ensuring that the waveform's oscillations match the detector's response.

- Masses of the Binary Components: The masses of the two compact objects in the binary system (m_1 and m_2) are fundamental parameters that shape the GW signal. These masses influence the inspiral rate, merger dynamics, and the resulting waveform's frequency and amplitude evolution. The total mass and mass ratio determine how quickly the binary spirals inward and how the GW frequency increases over time.

- Spins of the Binary Components: The intrinsic spins ($\vec{S}_1$ and $\vec{S}_2$) of the binary objects add another layer of complexity to the GW signal. Spin magnitudes and orientations relative to the orbital angular momentum can lead to precession effects, modulating the waveform's amplitude and phase. These spin-induced effects are vital for understanding the dynamics of the binary system and for accurately extracting source properties from the GW data.

Parameter estimation for BBHs involves the following parameter space: table.1

We consider a BBH merger with parameters in the source frame M1 = $36M_\odot$, M2 = $29M_\odot$, $d_L = 2000Mpc$, $\theta_{jn} = 0.4$, $\psi = 2.659$, phase = 1.3, and the optimal SNR is 15.57, including the detector network of H1 and L1. The priors for M1 and M2 are constraint from 5 to 100 $M_\odot$, while for other parameters (expect for θ_{jn} and δ) are uniform. Fig.11 illustrates the results posterior distributions of the full-space parameters and the joint posterior distributions of the parameter pairs. The analysis of the parameters using BILBY [103], the waveform of "IMRPhenomXPHM", the default design sensitivity PSDs of the interferometers (H1 and L1), and Dynesty sampler. The waveform indicates the model covers all three phases of a compact binary coalescence (Inspiral-Merger-Ringdown), and using a phenomenological approach, including precession.

Parameter	**Description**
Chirp Mass ($\mathcal{M}$)	Combination of component masses that primarily determines the frequency evolution of the inspiral phase (see eq.56).
Mass Ratio (q)	Ratio of the secondary mass to the primary mass, defined as $q = \frac{m_2}{m_1}$ (see eq.97).
Dimensionless Spin Magnitudes (a_1, a_2)	Magnitudes of the dimensionless spin parameters for each BH, $a_i = \frac{cJ_i}{Gm_i^2}$, where $i = 1, 2$.
Spin Tilt Angles (θ_1, θ_2)	Angles between each spin vector and the orbital angular momentum [34].
Spin Azimuthal Angles ($\Delta\phi, \phi_{JL}$)	$\Delta\phi$ is the azimuthal angle between the two spin vectors in the orbital plane. ϕ_{JL} is the angle between the total angular momentum and the orbital angular momentum [34].
Inclination Angle (θ_{JN})	Angle between the total angular momentum and the line of sight to the observer [34].
Orbital Phase (ϕ)	Phase of the orbit at a given reference time, often taken at the time of coalescence.
Polarization Angle (ψ)	Angle describing the orientation of the wave's polarization frame relative to the detector.
Luminosity Distance (d_L)	Distance from the source to the observer, affecting the amplitude of the GW signal.
Right Ascension (α)	Sky position of the binary system in the celestial coordinate system, defining the east-west direction.
Declination (δ)	Sky position of the binary system in the celestial coordinate system, defining the north-south direction.
Coalescence Time (t_c)	Time at which the two BHs merge into a single entity.

Table 1: Parameter space for BBH parameter estimation.

4.4 Relative Binning

Determining the source characteristics of extended-duration signals, including those originating from BNS events, in ground-based GW detectors can be computationally demanding. And this challenge is expected to grow as we advance towards next-generation (XG) GW detectors, such as A+, Cosmic Explorer, and the Einstein Telescope. These detectors will have increased sensitivity at lower frequencies, leading to longer in-band signals and a higher detection rate due to the overall increase in strain sensitivity.

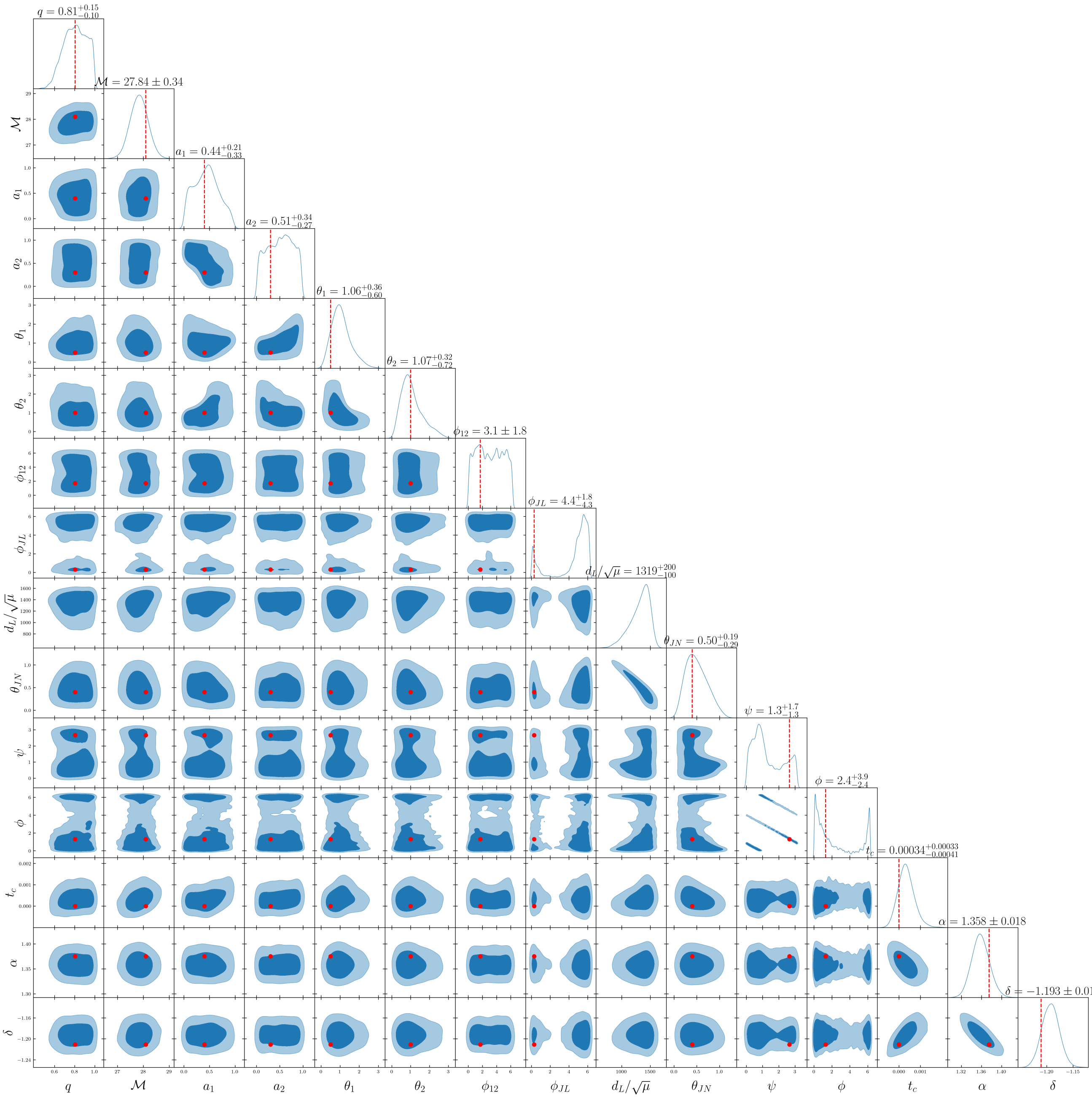

Figure 11: Marginalized posterior distribution for full parameters and joint posteriors for all pairs of these parameters. The red lines and red dots represent the injection value. The off-diagonal plots include contours representing 1σ and 2σ confidence intervals for each parameter pairs.

General-purpose algorithms are designed to generate samples from a distribution by evaluating the probability density at arbitrary points within the parameter space. These samplers efficiently explore the parameter space by leveraging the results of previous evaluations to inform new proposals.

In likelihood-based parameter estimation (PE), the bulk of the computational effort is typically spent on evaluating the likelihood function. To optimize this process, some techniques focus on accelerating individual likelihood evaluations, while others aim to reduce the number of evaluations required for the sampler to converge.

One such technique is relative binning, which speeds up likelihood evaluations by approximating the ratio of neighboring waveforms in the parameter space as a smooth function, allowing it to be approximated by a piecewise linear function [104]. This method enables the a computation in advance of certain terms in the likelihood. As a result, fewer frequency points are needed for waveform evaluation during sampling. This approach is particularly beneficial for the parameter estimation of compact binary coalescences (CBCs), especially those involving NSs, allowing for rapid parameter estimation.

To illustrate the effectiveness of this method in achieving both computational efficiency and accuracy, we analyzed a simulated 32-second duration strain signal from the LIGO L1, LIGO H1, and Virgo detectors, sampled at 2048 Hz. Our analysis focused on a frequency range of 20 Hz to 900 Hz, using 8 CPU cores. We employed fiducial parameters consistent with the injection parameters, the `IMRPhenomPv2_NRTidal` waveform model, and the `Dynesty` sampler, integrated with the `Bilby` analysis framework. The posterior distributions obtained from both the traditional method and relative binning showed strong agreement, validating the accuracy and efficiency of the relative binning technique.

Figures 12 and 13 present the corner plot of the posterior distributions for a BNS event, comparing the results obtained using the traditional computational method with those using relative binning. The total sampling time using relative binning was 49 minutes, in contrast to 8 hours and 25 minutes with the normal computational approach. This demonstrates that relative binning can significantly reduce computational costs while maintaining a fair accuracy. A bias in recovering the chirp mass is observed when using relative binning. In this case, the chirp mass is 1.215 $M_\odot$ and the mass ratio is $q = 0.876$. To investigate this further, we examined a scenario with a different chirp mass value of 1.5 $M_\odot$ and a mass ratio of $q = 0.75$, while keeping all other parameters unchanged. The results of this analysis are presented in Fig.14 and Fig.15. And within this injection values, it is well recovered for all parameters.

Relative binning is based on the idea that waveforms with high posterior probabilities are similar in the frequency domain. The main difference between these waveforms comes from small changes in their parameters. A stochastic sampler looks closely at a small region around the best-fitting waveform, where the likelihood is high. In this region, the variations between waveforms are minor and depend on the parameters. This results in a smooth ratio function between the waveforms.

Any smooth function can be approximated as a piecewise linear function by choosing suitable breakpoints. The space between two adjacent breakpoints forms a frequency bin, denoted as b_i.

Let's consider a reference waveform $\mu_0(f) = \mu(f, \boldsymbol{\theta_0})$ and a nearby waveform $\mu(f, \boldsymbol{\theta})$ within a

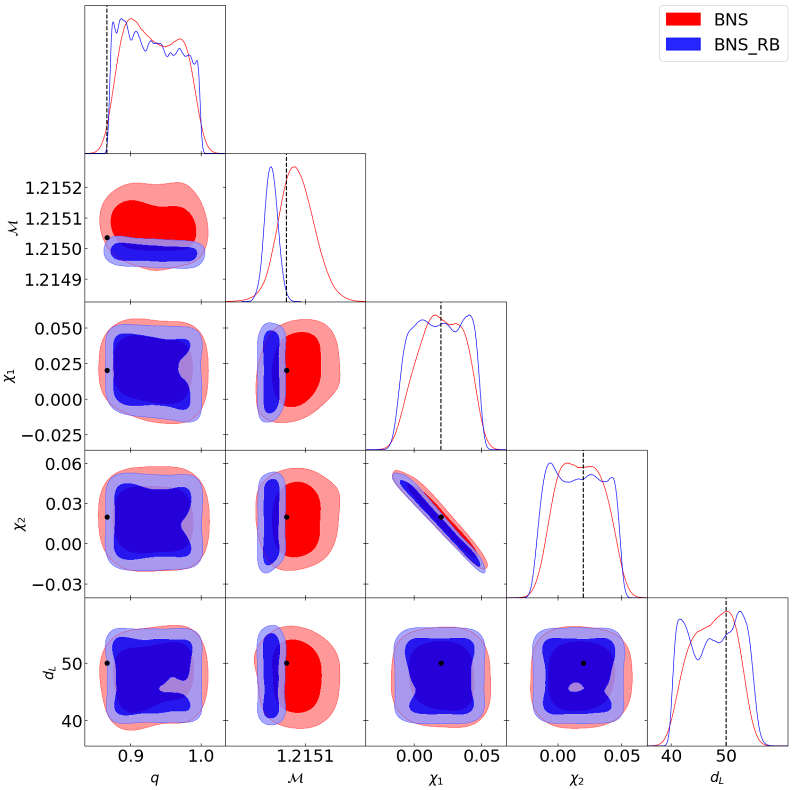

Figure 12: A comparison of posterior distributions—mass ratio, chirp mass, dimensionless spin parameters of the two NSs, and luminosity distance—is shown for a simulated signal analyzed using relative binning parameter estimation in Bilby (blue) and full likelihood computation (red). The diagonal panels display marginalized 1-dimensional histograms for each parameter, with dashed vertical lines representing the injected parameter values. The 2-dimensional joint posterior distributions are displayed in the off-diagonal panels, with the 1σ and 2σ credible regions represented by contours. The black dot within the contours indicates the injected values, with $q = 0.867$ and $\mathcal{M} = 1.215 M_{\odot}$.

region of high likelihood. The ratio of these waveforms, $r(f) = \frac{\mu(f)}{\mu_0(f)}$, can be approximated as:

$$r(f) \approx \begin{cases} r_0(b_1) + r_1(b_1)(f - f_m(b_1)), & \text{if } f \in b_1, \\ r_0(b_2) + r_1(b_2)(f - f_m(b_2)), & \text{if } f \in b_2, \\ \vdots \end{cases}$$

Here, $f_m(b_i)$ represents the midpoint of bin b_i. The coefficients $r_0(b_i)$ and $r_1(b_i)$, which are constant within each bin, are independent of frequency. By assuming linearity, these coefficients can be derived directly from the values of $r(f)$ at the edges of the bins. This approach enables $\mu(f, \boldsymbol{\theta})$ to be evaluated only at the bin edges rather than across the entire frequency range, thereby significantly reducing computational effort.

In the work of Barak Zackay and collaborators [105], this idea is extended by computing summary data in coarse frequency bins for a chosen fiducial waveform. Typically, this fiducial

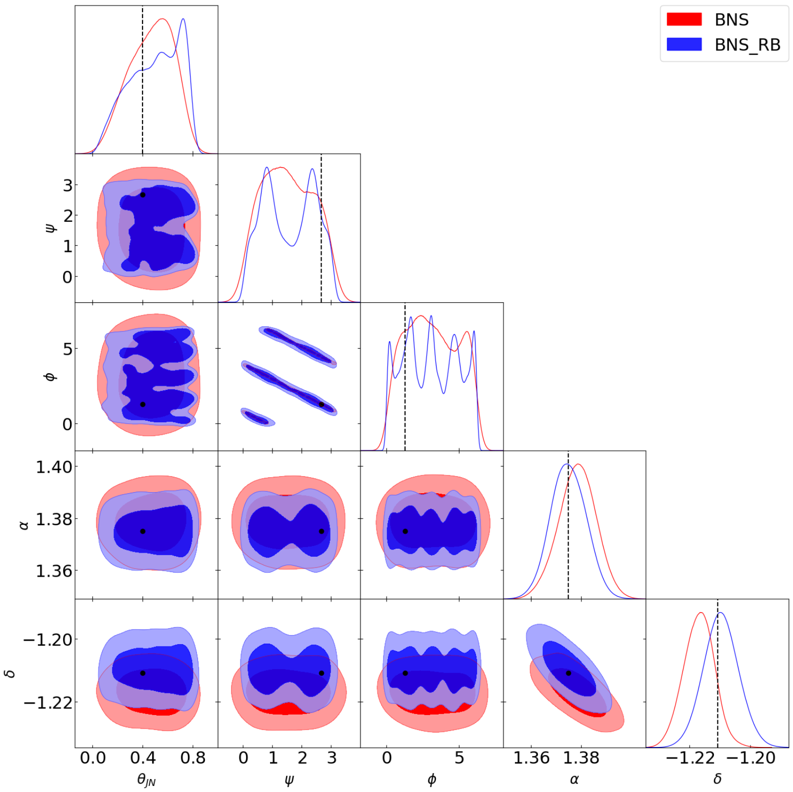

Figure 13: Comparison of posterior distributions for inclination angle, polarization, orbital phase, right ascension and declination.

waveform is selected to maximize the likelihood, although any waveform that closely approximates the best-fit solution may be used. It is shown that these summary data allow for accurate likelihood evaluations of any waveform sufficiently close to the fiducial one. As a result, the number of frequency bins needed to compute the data likelihood for a NS merger event can be reduced by about four orders of magnitude compared to a direct, naive computation.

4.5 Bias

Bias is the discrepancy between the true value of a parameter and the expected value of the estimator used to approximate it. Suppose you are estimating a set of parameters $\boldsymbol{\theta} = (\theta_1, \theta_2, \ldots, \theta_n)$ from data $\mathbf{D}$ using a likelihood function $\mathcal{L}(\mathbf{D}|\boldsymbol{\theta})$. By maximizing $\{L\}$, the maximum likelihood estimator $\hat{\boldsymbol{\theta}}$ is obtained, and its bias is defined as:

$$\text{Bias}(\hat{\boldsymbol{\theta}}) = \mathbb{E}[\hat{\boldsymbol{\theta}}] - \boldsymbol{\theta}$$

where $\mathbb{E}[\hat{\boldsymbol{\theta}}]$ is the expected value (average) of the estimator $\hat{\boldsymbol{\theta}}$ over repeated samples.

Precisely quantifying bias is crucial because it affects the accuracy of our parameter estimations. Accuracy refers to how well the estimator recoveries the injection values. Precision indicates

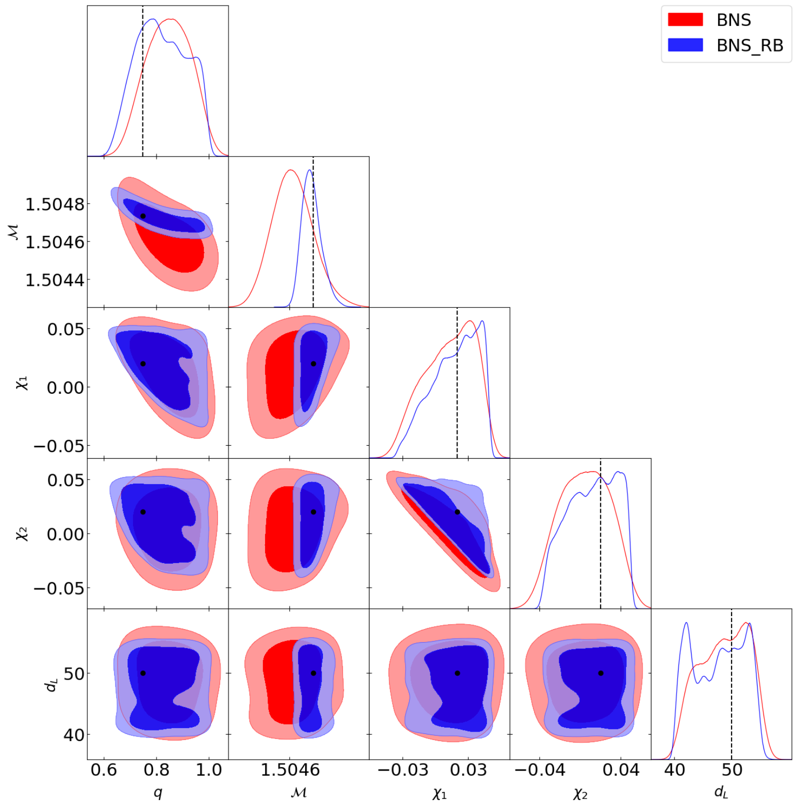

Figure 14: Posterior distributions for mass ratio, chirp mass, dimensionless spins, and luminosity distance for $q = 0.75$, $\mathcal{M} = 1.5M_\odot$.

how big is the error, or more precisely, refers to the degree of variability in the estimator's values. Mathematically,

$$\mathrm{Var}(\hat{\boldsymbol{\theta}}) = \mathbb{E}[(\hat{\boldsymbol{\theta}} - \mathbb{E}[\hat{\boldsymbol{\theta}}])^2] \tag{159}$$

the variance quantifies how much the estimator $\hat{\boldsymbol{\theta}}$ fluctuates around its expected value.

The mean squared error combines both bias and variance:

$$\mathrm{MSE}(\hat{\theta}) = \mathrm{Bias}(\hat{\theta})^2 + \mathrm{Var}(\hat{\theta}) \tag{160}$$

Obtaining the variance values is crucial for constructing the covariance matrix $\boldsymbol{\Sigma}$, which is essential for quantifying uncertainties, creating confidence intervals, and plotting confidence ellipses in the parameter estimation. The Fisher Information Matrix is a pivotal tool in statistics that quantifies how much information observable random variables contain about parameters that are not directly measurable. It establishes a framework for interpreting the relationship between the data and the parameters we wish to estimate. The accuracy of parameter estimates is assessed by the Fisher Information Matrix, which analyzes the expected value of the second derivative of the log-likelihood function. A larger Fisher Information indicates that the data offer substantial information about the parameter, thereby enabling more precise estimation. It is widely used to

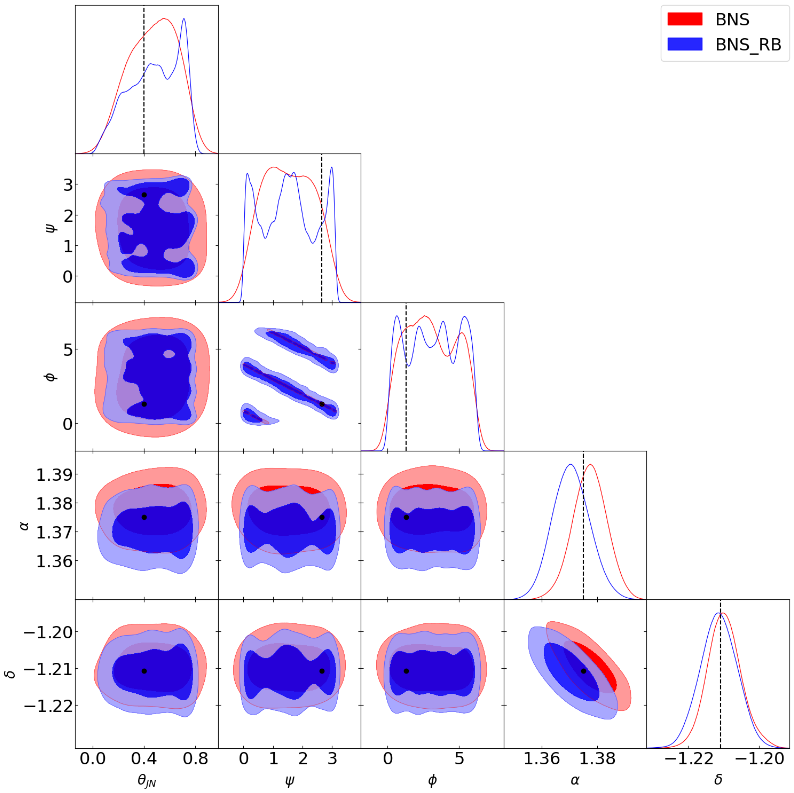

Figure 15: Posterior distributions for inclination angle, polarization, phase, and sky location: right ascension and declination for $q = 0.75$, $\mathcal{M} = 1.5M_{\odot}$.

estimate the variances and covariances of parameter estimators, especially under the assumption that the likelihood function is approximately Gaussian near the maximum likelihood estimate (MLE). By definition,

$$I_{ij} = -\mathbb{E}\left[\frac{\partial^2 \ln \mathcal{L}}{\partial\theta_i \partial\theta_j}\right] \tag{161}$$

where $\mathbb{E}$ is the expectation over the data and $\mathcal{L}(\mathbf{D}|\boldsymbol{\theta})$ is the likelihood function of data $\mathbf{D}$ given parameters $\boldsymbol{\theta}$, specifically, for GWforms the inner product in the likelihood is $\left(\frac{\partial h}{\partial\theta_i}\middle|\frac{\partial h}{\partial\theta_j}\right)$.

The inverse of the Fisher information matrix gives the covariance matrix:

$$\boldsymbol{\Sigma} = \boldsymbol{I}^{-1} \tag{162}$$

the variances are diagonal elements $\sigma_i^2 = \Sigma_{ii}$, and covariances are off-diagonal elements $\sigma_{ij} = \Sigma_{ij}$. The covariance matrix for n random variables is thus:

$$\Sigma = \begin{bmatrix} \mathrm{Var}(\theta_1) & \mathrm{Cov}(\theta_1, \theta_2) & \cdots & \mathrm{Cov}(\theta_1, \theta_n) \\ \mathrm{Cov}(\theta_2, \theta_1) & \mathrm{Var}(\theta_2) & \cdots & \mathrm{Cov}(\theta_2, \theta_n) \\ \vdots & \vdots & \ddots & \vdots \\ \mathrm{Cov}(\theta_n, \theta_1) & \mathrm{Cov}(\theta_n, \theta_2) & \cdots & \mathrm{Var}(\theta_n) \end{bmatrix}$$

MCMC methods are also powerful in Bayesian analysis. The posterior distribution is defined:

$$p(\boldsymbol{\theta}|\mathbf{D}) \propto \mathcal{L}(\mathbf{D}|\boldsymbol{\theta})\, p(\boldsymbol{\theta}) \tag{163}$$

and we could run MCMC chains to sample from the posterior, then compute sample statistics:

$$\sigma_i^2 = \mathrm{Var}(\theta_i) = \frac{1}{N-1}\sum_{k=1}^{N}(\theta_i^{(k)} - \bar{\theta}_i)^2 \tag{164}$$

$$\sigma_{ij} = \mathrm{Cov}(\theta_i, \theta_j) = \frac{1}{N-1}\sum_{k=1}^{N}(\theta_i^{(k)} - \bar{\theta}_i)(\theta_j^{(k)} - \bar{\theta}_j) \tag{165}$$

Correlation between estimated parameters indicates how changes in one parameter affect another, which is quantified using the covariance matrix. For parameters θ_i and θ_j:

$$\mathrm{Cov}(\hat{\theta}_i, \hat{\theta}_j) = \mathbb{E}[(\hat{\theta}_i - \mathbb{E}[\hat{\theta}_i])(\hat{\theta}_j - \mathbb{E}[\hat{\theta}_j])] \tag{166}$$

and correlation coefficient is:

$$\rho_{ij} = \frac{\mathrm{Cov}(\hat{\theta}_i, \hat{\theta}_j)}{\sqrt{\mathrm{Var}(\hat{\theta}_i)\mathrm{Var}(\hat{\theta}_j)}} \tag{167}$$

The covariance matrix can be written in this form, given two parameters θ_1 and θ_2, with means μ_1 and μ_2, variances σ_1^2 and σ_2^2, and covariance σ_{12}:

$$\boldsymbol{\Sigma} = \begin{pmatrix} \sigma_1^2 & \sigma_{12} \\ \sigma_{12} & \sigma_2^2 \end{pmatrix} \tag{168}$$

The equation of the confidence ellipse provides a graphical representation of the confidence region for the mean of a bivariate normal distribution. It is also used to describe the relationship between two variables. This ellipse helps visualize both the variability and the correlation between the two variables in question. The confidence ellipse is mathematically defined by the following equation:

$$(\boldsymbol{\theta} - \boldsymbol{\mu})^\top \boldsymbol{\Sigma}^{-1}(\boldsymbol{\theta} - \boldsymbol{\mu}) = \chi^2 \tag{169}$$

where $\boldsymbol{\theta}$ is the parameter vector

$$\begin{pmatrix} \theta_1 \\ \theta_2 \end{pmatrix} \tag{170}$$

$\boldsymbol{\mu}$ is the mean vector

$$\begin{pmatrix} \mu_1 \\ \mu_2 \end{pmatrix} \tag{171}$$

$\mathbf{\Sigma}^{-1}$ is the inverse of the covariance matrix, and χ^2 is chi-squared value value corresponding to the desired confidence level.

The confidence ellipse equation defines the joint confidence region for two correlated parameters estimated from data. The left-hand side of the equation is a quadratic form representing the squared Mahalanobis distance between the estimated parameters and their mean values. And right-hand side χ^2 corresponds to a value drawn from the chi-squared distribution, where the degrees of freedom match the number of parameters. The specific value of χ^2 determines the confidence level: $\chi^2 = 2.3$ is 68.3% confidence level, $\chi^2 = 5.99$ is 95.4% confidence level, and $\chi^2 = 9.21$ is 99.7% confidence level.

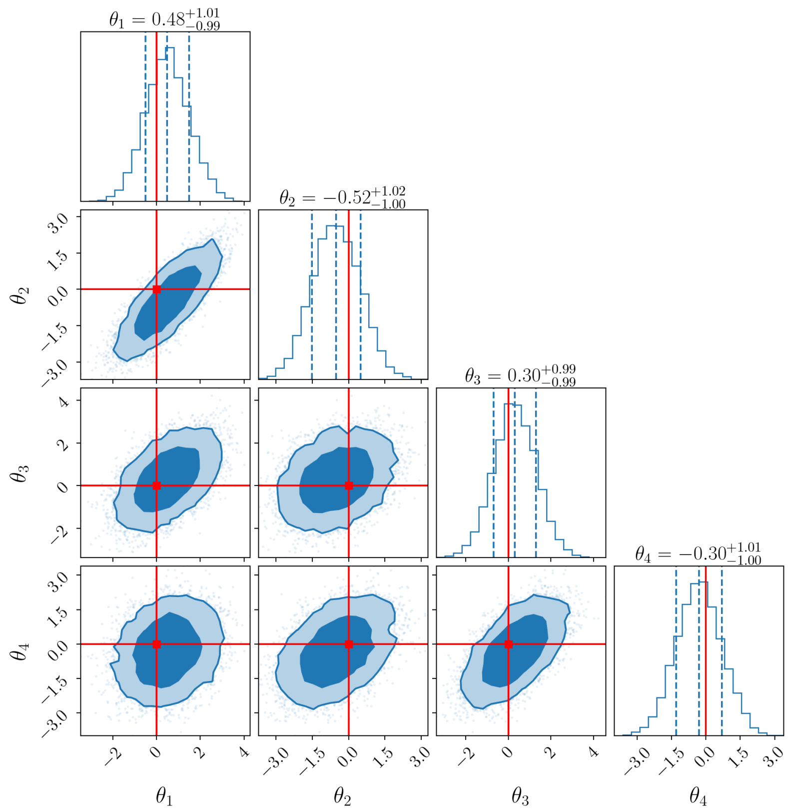

Figure 16: Corner plot displaying the posterior distributions for four parameters, θ_1, θ_2, θ_3, and θ_4, sampled from a biased multivariate normal distribution with specified correlations. The plot shows histograms for the marginalized distributions along the diagonal, with contour plots for pairwise parameter correlations in the off-diagonal panels. Red lines indicate the true (unbiased) parameter values. The contours represent confidence regions, with darker shades indicating higher probability density. The quantiles (68th, and 95th percentiles) are marked by dashed lines on the histograms to illustrate the distribution spread around the median.

Fig.16 shows an example for posterior distributions and correlations under the influence of systematic biases. The red dots and lines are the true values and any consistent deviation of the central tendency of the distributions (blue dashed lines) from these red lines indicates a bias. The variance of an estimator represents the spread of the posterior distribution around its mean in the plot. The true values for four variables are set to 0, while the systematic shifts are introduced, resulting in the biased parameter values $\theta_1 = 0.5, \theta_2 = -0.5, \theta_3 = 0.3, \theta_4 = -0.3$.

The correlations are introduced by the covariance matrix, reflected in the contour plots, where the ellipses indicate the degree of correlation between parameter pairs. In this plot, θ_1 and θ_2 exhibit a strong positive correlation $r = 0.8$, as demonstrated by the narrow elliptical contours oriented along the diagonal. In contract, θ_1 and θ_4 show weaker correlation $r = 0.2$.

5 Parameter estimation for lensing

5.1 Binary black hole

We investigate the impact on source parameter recovery for distinguishable type-II and type-III image signals when unlensed image templates are employed during parameter estimation. Figures 17 and 18 compare the parameter recovery of the three types of injected images using their corresponding templates. The injected parameters are a mass ratio of $q = 0.81$, a chirp mass of $\mathcal{M} = 28.1 M_\odot$, a magnification factor of $\mu = 2$, and a SNR of 29. The injected values fall well within the posterior PDFs for all three recoveries, except for the sky location parameters—declination (δ) and right ascension (α). While both type-I and type-II images recover these sky location parameters accurately, the type-III image signal exhibits a significant bias. In the off-diagonal plots of Figure 17, the correlation between the polarization angle and the phase reveals a bias of $\pi/4$, which is inherently embedded in the waveform templates.

However, when we increase the magnification factor to $\mu = 100$, resulting in a corresponding SNR of 205 while keeping all other parameters fixed (as shown in Figures 19, 20), the injected values for q, d_L, and ι fall into regions of low posterior probability. This demonstrates that increasing the sensitivity can introduce larger biases in certain areas of the parameter space. Notably, the biases in the sky location parameters—α and δ —become less apparent.

Furthermore, we analyze the case of a lower mass ratio, $q = 0.2$, increases the inclination angle to $\iota = 0.5$, while keeping all other parameters unchanged. The resulting SNR is 165, as illustrated in Fig. 21 and Fig. 22. A noticeable bias is observed only in the luminosity distance (d_L), where the injected value is $d_L/\mu = 200\, M_\odot$, while the recovered value is approximately $2000\, M_\odot$.

When the inclination angle ι is close to 0 (i.e., the binary system is face-on), the Type-II image signal can be effectively reproduced by adjusting the coalescence phase. In such cases, the phase shift induced by gravitational lensing can be absorbed by the coalescence phase ϕ_c, allowing the lensed signal to closely resemble an unlensed signal, as demonstrated in [80]. However, as the inclination angle increases (i.e., the system is viewed more edge-on), additional distortions appear in the Type-II image that cannot be accounted for by simply adjusting the coalescence phase. These distortions are not present in the general relativistic (GR) signal, indicating that the Type-II lensed signals deviate from their unlensed counterparts under these conditions.

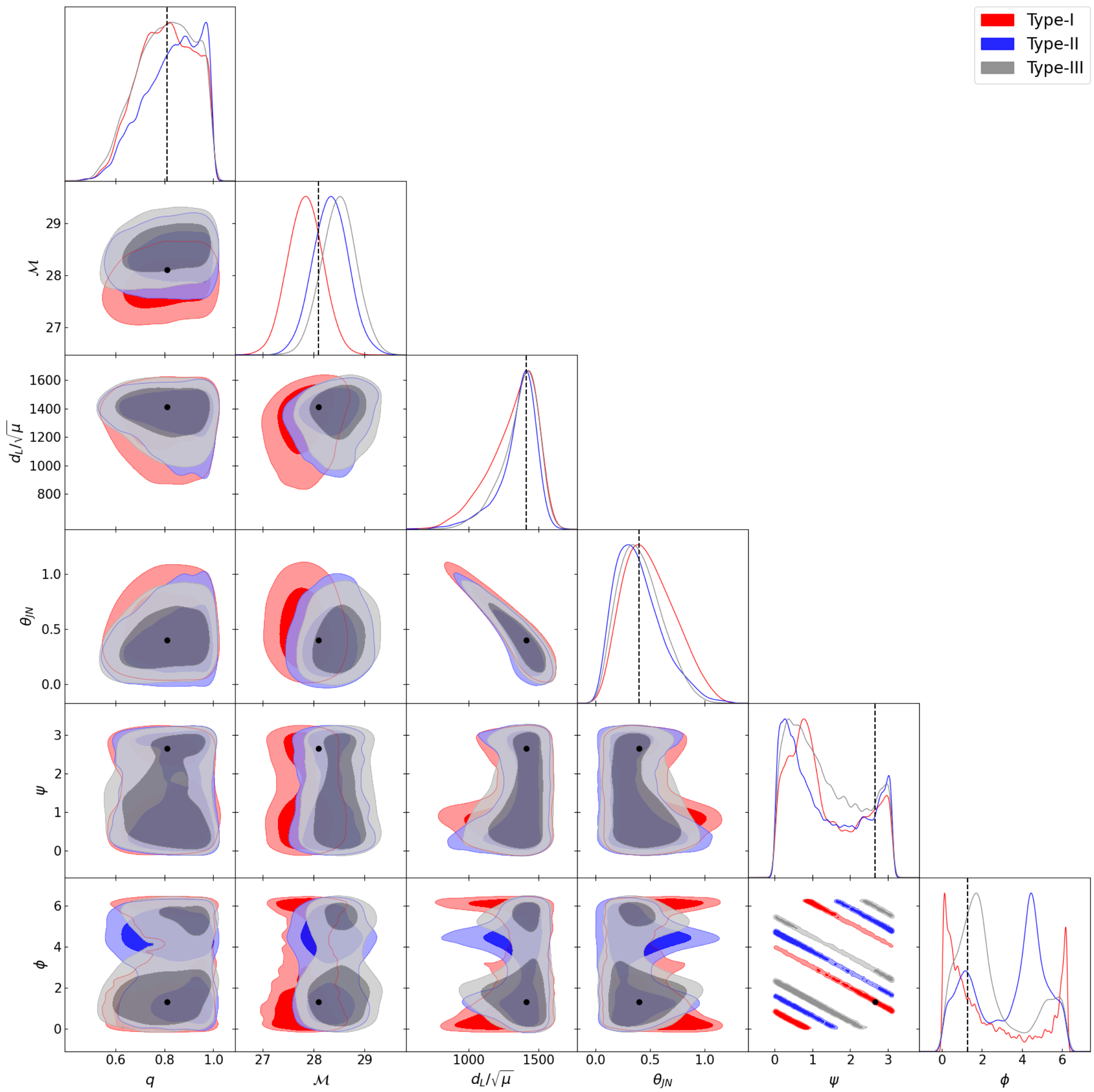

Figure 17: The recovery of source parameters for mass ratio $q = 0.81$, chirp mass $\mathcal{M} = 28.1 M_{\odot}$, SNR $\rho = 29$, inclination angle $\iota = 0.4$, and magnification factor $\mu = 2$ is presented. Results are shown for Type-I (red), Type-II (blue), and Type-III (grey) injection values, where the black dots denote the injection values. The plot includes the recovery of key parameters: mass ratio q, chirp mass $\mathcal{M}$, observed luminosity distance $\frac{d_L}{\sqrt{\mu}}$, inclination angle ι, polarization angle ψ, and phase ϕ. The black dashed lines indicate the injected values. The recovery for Type-I, Type-II, and Type-III image signals aligns consistently with the injection values.

The analysis presented in [80] compares scenarios with a low mass ratio ($q = 0.2$) high total mass ($M = 100 M_{\odot}$), low SNR ($\rho = 20$) and varying inclination angles ($\iota = \pi/6$ and $\iota = 5\pi/12$). The analysis indicates that increasing the inclination angle while holding other parameters constant results in the injected masses, distance, and inclination values falling into a region of low posterior probability. This demonstrates that waveform distortions can introduce substantial biases in

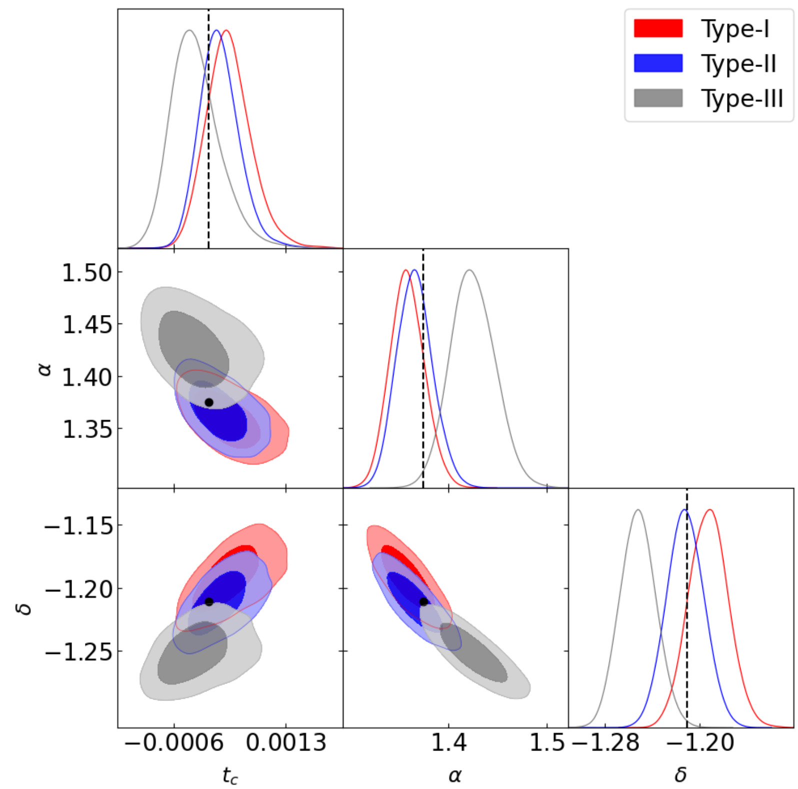

Figure 18: The plot shows the recovery of the time of arrival t_c in the geocenter time, sky location δ (declination), and α (right ascension). There is no bias in the recovery of both Type-I and Type-II templates, but the sky location δ and α show a bias for the Type-III image signal.

parameter estimation within specific areas of the parameter space. Additionally, when the SNR is low ($\rho = 20$), the phase shift introduced by type-II images has negligible impact on the recovery of intrinsic parameters and the estimation of distance for BBH systems. This implies that at lower SNRs, the intrinsic characteristics of the system, such as masses and spins, as well as the distance to the source, can be accurately inferred without significant interference from phase shifts caused by type-II lensing images.

However, as the SNR increases to higher values ($\rho = 50$), the influence of type-II image phase shifts becomes more pronounced, particularly at larger inclination angles ($\iota \geq 5\pi/12$). In these scenarios, the discrepancies in parameter recovery are substantial, indicating that the phase shifts introduced by lensing effects start to interfere with the accurate determination of system parameters.

Furthermore, for BBH systems with greater total mass (M), these differences in parameter recovery become significant even at lower inclination angles, around $\iota \sim \pi/3$. This suggests that more massive systems are more susceptible to the distortions caused by phase shifts, leading to greater uncertainties in parameter estimation at moderate inclination angles.

The estimation of distance is particularly affected, showing significant deviations at inclination angles as low as $\iota \sim \pi/4$. This indicates that distance measurements become less reliable when

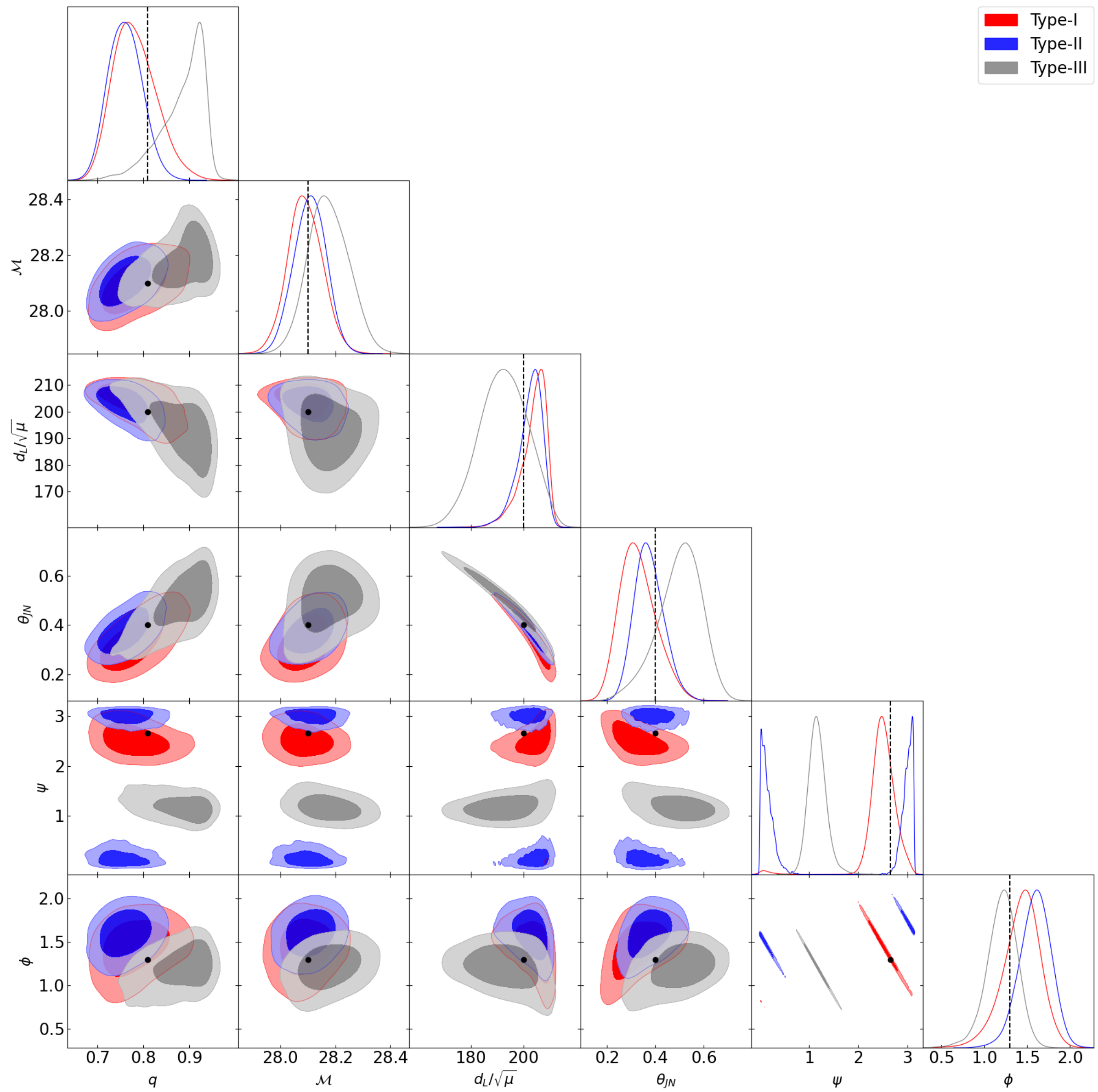

Figure 19: The recovery of source parameters using Type-I (red), Type-II (blue), and Type-III (grey) templates for mass ratio $q = 0.81$, chirp mass $\mathcal{M} = 28.1 M_{\odot}$, SNR $\rho = 29$, inclination angle $\iota = 0.4$, and magnification factor $\mu = 100$

the inclination angle approaches $\pi/4$, especially in the presence of strong lensing effects.

Moreover, as the SNR continues to increase beyond $\rho = 50$, the critical inclination angle at which these effects become significant decreases. This means that even at lower inclination angles, higher SNRs exacerbate the impact of phase shifts on parameter recovery, further challenging the accuracy of intrinsic parameter and distance estimations in highly inclined, high-SNR BBH systems.

In this study, as shown in Fig.23, we investigate how well parameters are recovered for BBH systems with inclination angles (ι) varying between 0.5 and 2.5. We also explore different mass ratios of the injected BBH systems while maintaining all other parameters constant. Additionally,

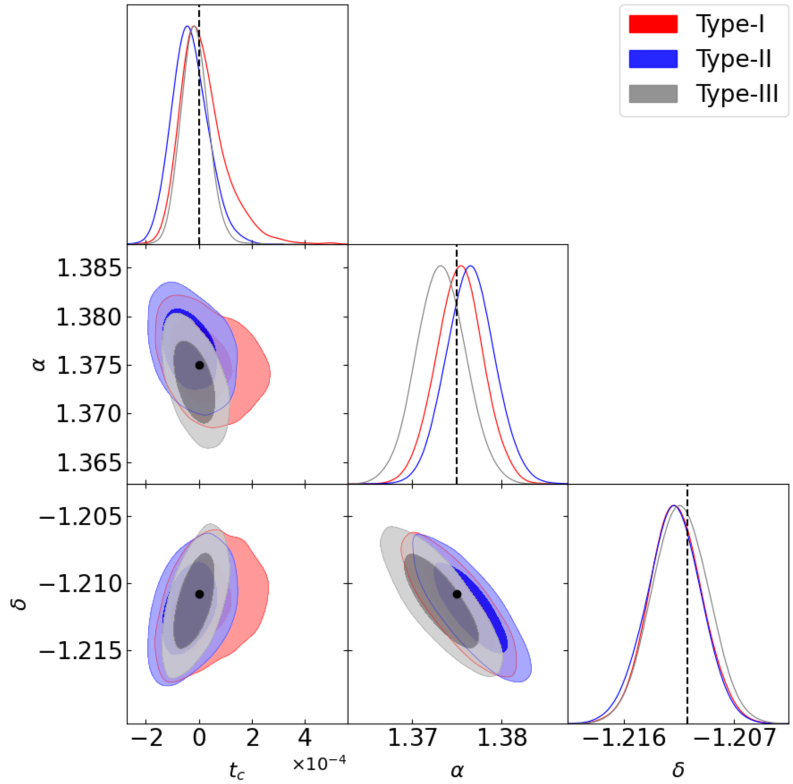

Figure 20: The plot shows the recovery of the time of arrival t_c in the geocenter time, sky location δ (declination), and α (right ascension) for $\mu = 100$.

Fig.24 presents the parameter recovery performance under a higher SNR of $\rho = 62$, using the same set of inclination angles and mass ratios.

The distance, we defined it as:

$$\text{distance} = \frac{|Q_{\text{in}} - Q_{\text{mode}}|}{\sigma} \tag{172}$$

where σ is the standard deviation, and Q_{in} is the injection value, Q_{mode} is the mode of the posterior distribution for the parameter.

The distance metric utilized in this study serves to quantify the extent of deviation between the injected parameter value and the mode, or the most probable value, of the posterior distribution. This measurement is expressed in units of standard deviation, providing a standardized framework for assessing how closely the injected value aligns with the posterior mode. A smaller value of this distance metric indicates that the injected parameter is situated near the peak of the posterior distribution. This proximity suggests that the parameter recovery process is functioning effectively, as the inferred parameters closely match the true, injected values.

In practical terms, when the distance metric approaches zero, it implies that the injected parameter value coincides precisely with the mode of the posterior distribution. Such an alignment signifies a high degree of agreement between the expected parameters—those that were intention-

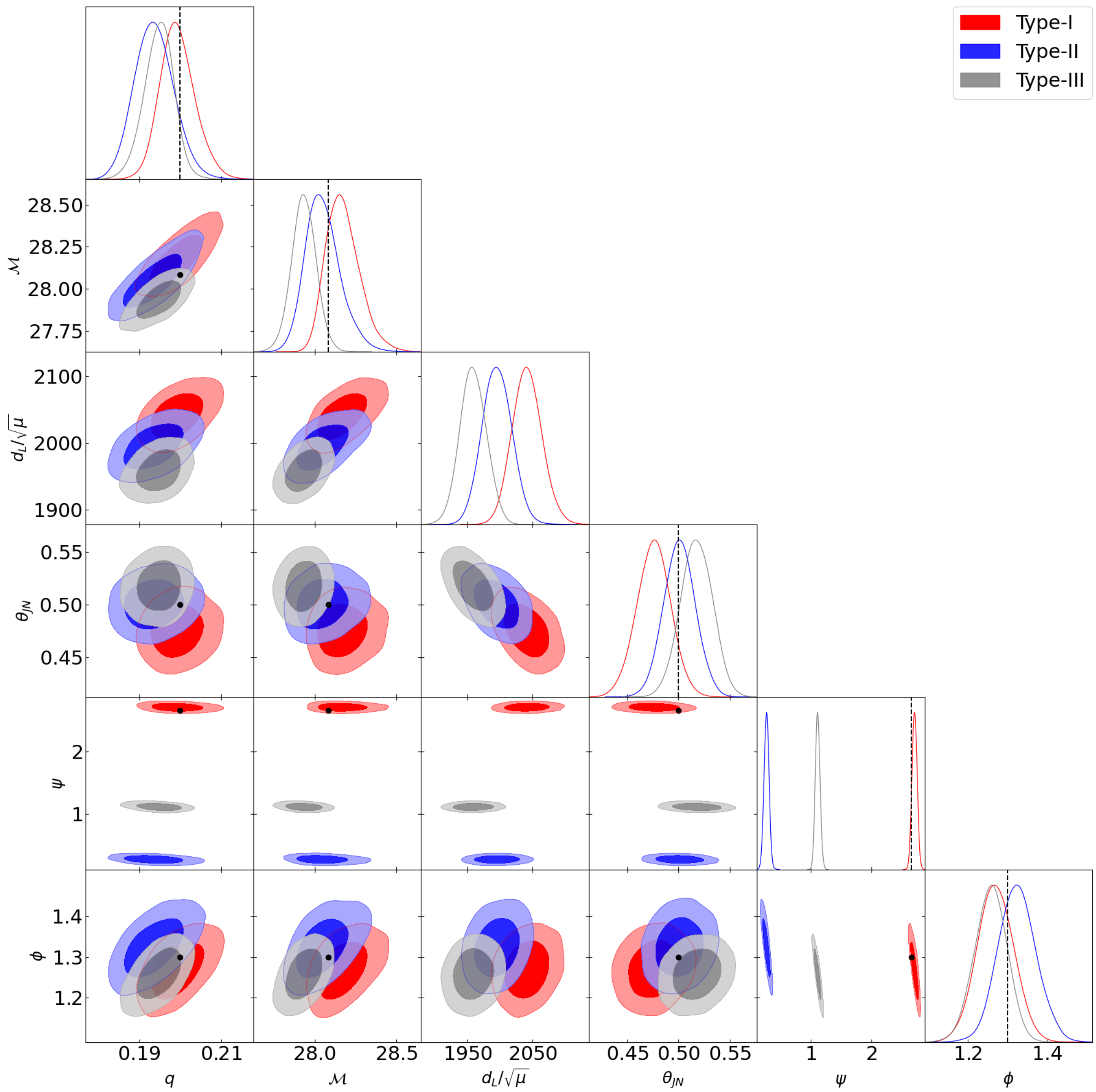

Figure 21: The recovery of source parameters using Type-I (red), Type-II (blue), and Type-III (grey) templates for mass ratio $q = 0.2$, chirp mass $\mathcal{M} = 28.1 M_{\odot}$, SNR $\rho = 29$, inclination angle $\iota = 0.5$, and magnification factor $\mu = 100$

ally introduced—and the parameters that have been accurately recovered through the analysis. This strong concordance is indicative of reliable parameter estimation, demonstrating that the inference method successfully identifies the true underlying parameters based on the observed data.

Conversely, a larger value of the distance metric reveals a substantial separation between the injected parameter value and the posterior mode. This significant deviation may highlight potential biases within the parameter estimation process or expose inherent limitations in the modeling approach employed. Such biases could arise from various sources, including assumptions made during model construction, the quality or quantity of the data used, or computational

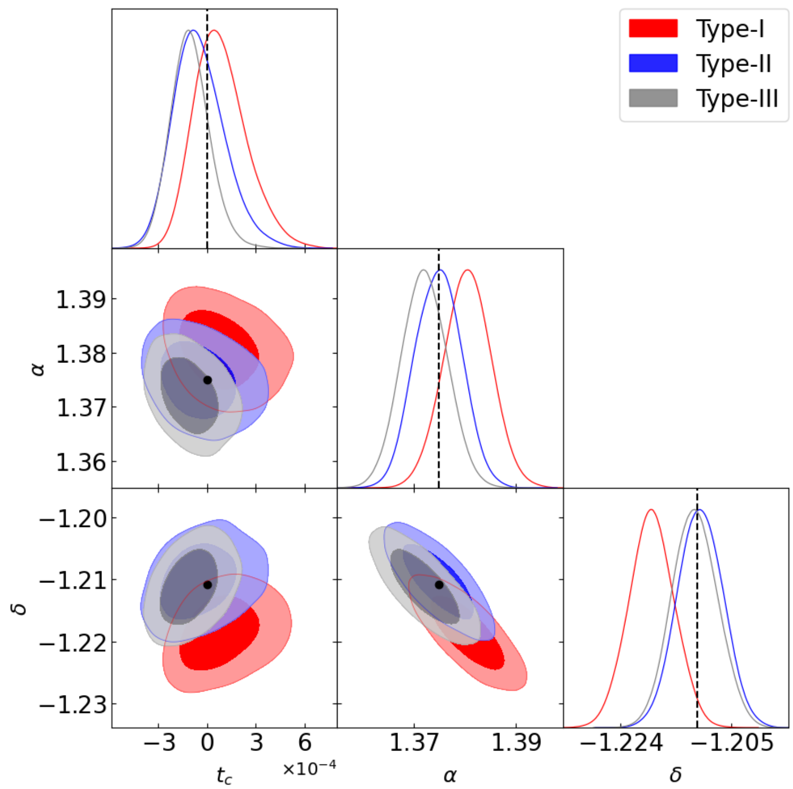

Figure 22: The plot shows the recovery of the time of arrival t_c in the geocenter time, sky location δ (declination), and α (right ascension) for $q = 0.2$ and $\mu = 100$.

constraints inherent in the inference algorithms. Identifying instances where the distance metric is large is crucial, as it underscores areas where the parameter estimation methodology may require refinement or where additional data might be necessary to achieve more accurate and reliable results.

Understanding the biases in parameter recovery at varying inclination angles and mass ratios is crucial for the accurate characterization of BBH systems, especially under low SNR conditions. As illustrated in Fig. 23, our analysis focuses on how different mass ratios (q) and inclination angles (ι) impact the precision of parameter estimation in BBH systems.

For BBH systems with a mass ratio of $q = 0.2$, parameter recovery for mass ratio demonstrates superior performance compared to systems with higher mass ratios of $q = 0.5$ and $q = 0.8$. This enhanced performance suggests that lower mass ratios may be inherently more stable against biases introduced by varying inclination angles at lower SNRs. In contrast, higher mass ratios exhibit increasing bias in mass ratio recovery as the inclination angle ι rises, peaking around $\iota = 1.5$. Beyond this peak, as the inclination angle continues to increase towards 2.5, the bias gradually diminishes.

The chirp mass ($\mathcal{M}$) shows a nuanced pattern of bias across different mass ratios and inclination angles. Specifically, for $q = 0.5$, the bias remains minimal when $\iota < 2.3$, indicating effective parameter recovery at lower inclination angles. Conversely, for $q = 0.2$ and $q = 0.8$, the bias in

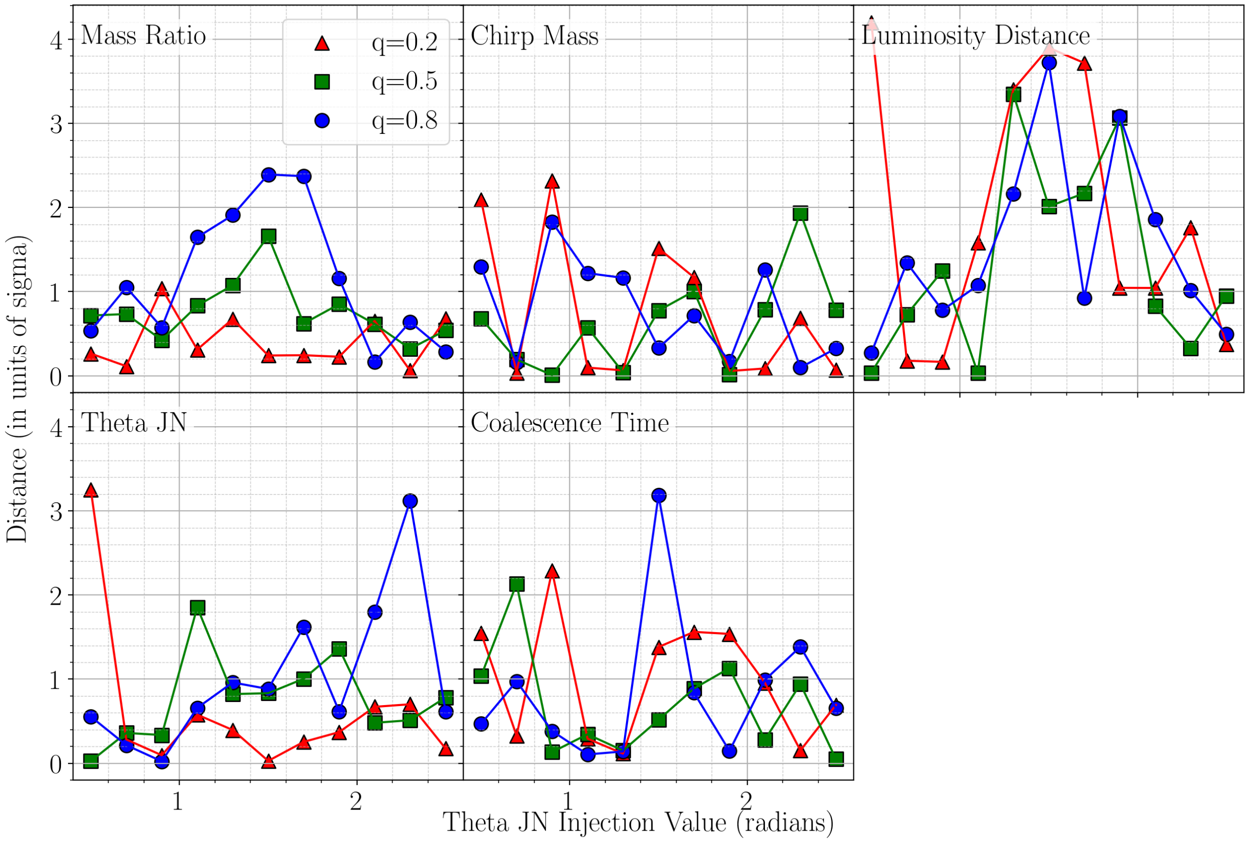

Figure 23: Each panel displays the difference between the injected value and the mode of the posterior distribution as a function of the inclination angle (ι) for the injected BBH systems. The systems have a fixed chirp mass ($\mathcal{M} = 28M_{\odot}$) and SNR ($\rho = 19.6$). The injections utilize the type-II image template. The results are color-coded based on the mass ratio: blue represents $q = 0.8$, green corresponds to $q = 0.5$, and red indicates $q = 0.2$. Each subplot illustrates the parameter estimation outcomes for various parameters, namely the mass ratio, chirp mass, luminosity distance, inclination angle, and coalescence time. This comparison demonstrates how parameter estimation accuracy changes with varying inclination angles.

chirp mass estimation peaks at $\iota = 0.9$ before tapering off as ι increases further. This behavior underscores the sensitivity of chirp mass estimation to inclination angles, particularly in moderately inclined systems.

Luminosity distance (D_L) estimation exhibits significant systematic biases across all examined mass ratios within the inclination angle range of $\iota = 1.3$ to 1.9. This consistent bias suggests potential challenges in accurately determining distance measurements under these specific inclination conditions at low SNRs. Notably, for $q = 0.2$, a substantial bias is also observed at $\iota = 0.5$, indicating that very low inclination angles may pose difficulties in distance estimation for highly asymmetric BBH systems.

The recovery of the inclination angle (ι) itself is influenced by both mass ratio and the angle's magnitude. For higher mass ratios ($q = 0.5$ and $q = 0.8$), the bias in inclination angle recovery generally increases as ι rises from 0.5 to 1.9, reflecting heightened uncertainties in more inclined

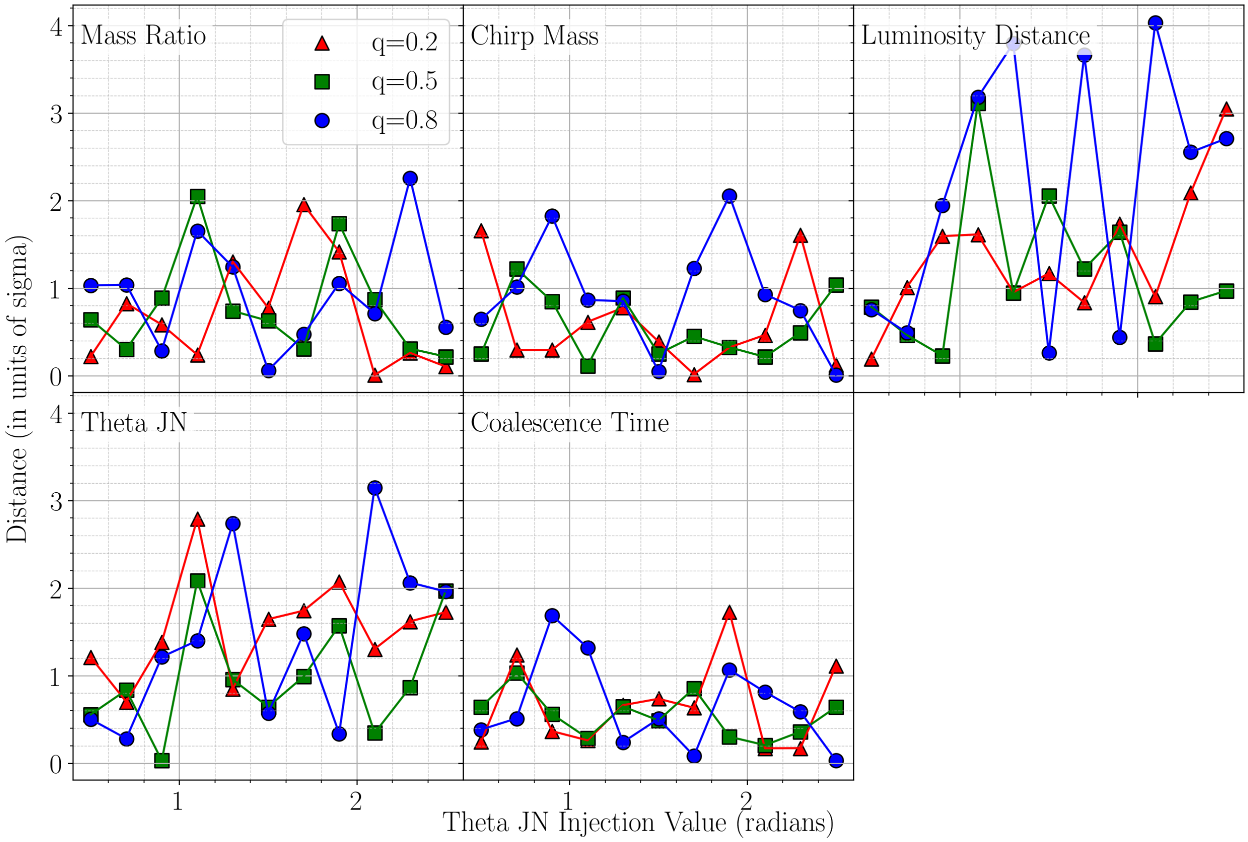

Figure 24: Each panel shows the distance between the injection value and the mode of the posterior distribution value against the inclination angle (ι) of the injected BBH systems for a given chirp mass ($\mathcal{M} = 28M_{\odot}$), and SNR ($\rho = 62$).

systems. Specifically, for $q = 0.8$, the bias peaks at $\iota = 2.5$ before declining with further increases in ι. In contrast, for $q = 0.2$, the bias is most pronounced at $\iota = 0.5$, suggesting that even slight inclinations can introduce significant uncertainties in parameter estimation for highly asymmetric mass ratios.

The estimation of coalescence time (t_c) shows varied performance across different mass ratios and inclination angles. Systems with a higher mass ratio of $q = 0.8$ exhibit improved recovery accuracy compared to those with lower mass ratios, particularly at inclination angles below 1.5. This indicates that more symmetric BBH systems may facilitate more precise estimations of coalescence time under low SNR conditions.

The biases observed in parameter recovery across different mass ratios and inclination angles at low SNRs highlight critical areas for improvement in our inference methodologies. The substantial biases in luminosity distance and inclination angle at specific inclination ranges suggest that current estimation techniques may require refinement to enhance accuracy. Future research should focus on developing more robust inference algorithms capable of mitigating these biases, especially for systems with higher mass ratios and varying inclination angles. Additionally, investigating the impact of different SNR levels on these biases could provide deeper insights into optimizing parameter recovery techniques for diverse observational scenarios.

At a higher SNR of $\rho = 62$, as illustrated in Fig. 24, the parameter recovery dynamics exhibit distinct behaviors compared to the lower SNR scenario. Specifically, the recovery of the mass ratio (q) for values $q = 0.2$ and $q = 0.5$ shows slightly increased biases relative to the lower SNR case. This indicates that, despite the higher SNR, certain mass ratios may still encounter challenges in accurate parameter estimation. Conversely, for the higher mass ratio of $q = 0.8$, the recovery process remains robust, particularly at lower inclination angles ($\iota < 2.3$). This suggests that more symmetric BBH systems benefit from higher SNRs, resulting in more reliable mass ratio estimations under these conditions.

When examining the chirp mass ($\mathcal{M}$), the results reveal that lower mass ratios ($q = 0.2$ and $q = 0.5$) maintain commendable performance across varying inclination angles. These curves demonstrate minimal bias, indicating effective parameter recovery even as inclination angles change. In contrast, the chirp mass recovery for $q = 0.8$ exhibits a peak bias around $\iota = 1.9$, slightly surpassing the 2σ threshold. This peak suggests that at certain inclination angles, the estimation of chirp mass becomes more susceptible to bias, potentially due to the complex interplay between mass ratio and orientation at higher SNRs.

The estimation of luminosity distance (D_L) presents a more nuanced picture. For a mass ratio of $q = 0.2$, the bias in luminosity distance increases steadily as the inclination angle ι rises. This trend indicates that distance estimation becomes progressively less accurate with increasing inclination angles for highly asymmetric systems. For $q = 0.5$, the bias curve reaches its maximum at $\iota = 1.1$ and subsequently decreases as ι continues to increase. This behavior highlights a peak sensitivity in distance estimation around this inclination angle, followed by improved accuracy at higher angles. However, for the highest mass ratio of $q = 0.8$, significant biases are observed at multiple inclination angles, notably at $\iota = 1.3$, $\iota = 1.7$, and for $\iota > 2.1$. These pronounced biases suggest that distance estimation for more symmetric BBH systems can be particularly challenging at these specific inclination angles, even at higher SNRs.

The recovery of the inclination angle (ι) itself generally shows an increasing bias trend as ι increases. However, within the range of $\iota = 1.1$ to $\iota = 1.3$, local decreases in bias are observed, indicating periods of improved estimation accuracy amidst the overall increasing trend. Notably, all mass ratio curves exceed the 2σ threshold within this inclination angle range, underscoring significant uncertainties in inclination angle recovery under these conditions. Additionally, for $q = 0.8$, even larger biases emerge at inclination angles exceeding $\iota = 2.1$, further emphasizing the challenges in accurately estimating inclination angles for highly symmetric BBH systems at high SNRs.

Finally, the recovery of coalescence time (t_c) demonstrates favorable performance across all examined mass ratios. Regardless of the mass ratio, coalescence time is accurately estimated, indicating that this parameter is less susceptible to the biases observed in mass ratio, chirp mass, luminosity distance, and inclination angle recoveries. This consistent performance suggests that coalescence time remains a robust parameter under high SNR conditions, providing reliable estimates even as other parameters exhibit varying levels of bias.

Overall, the analysis at $\rho = 62$ reveals that while higher SNRs generally enhance parameter recovery accuracy, certain mass ratios and inclination angles still pose significant challenges. The increased biases observed for specific mass ratios and inclination angles highlight the need for refined inference methods and further investigation to mitigate these discrepancies, ensuring more accurate and reliable parameter estimations in BBH systems.

In our comparative analysis with the findings documented by Aditya Vijaykumar [80], we observe consistent outcomes for binary systems characterized by lower total masses and a SNR of approximately 20. Both studies demonstrate effective recovery of crucial source parameters, specifically the chirp mass and the mass ratio of the binary system.

Notably, both studies identify an increasing trend in measurement bias for the luminosity distance as the inclination angle (ι) increases. As ι approaches 90° (edge-on orientation), the projection effects and relativistic beaming can introduce complexities in parameter estimation. In our analysis, we observe that the bias in luminosity distance measurements grows with increasing ι, reaching a peak around an inclination angle of $\iota = 1.3$ radians. This peak suggests that there is a particular orientation where the measurement bias is maximized, potentially due to the interplay between GW amplitude modulation and the detector's sensitivity pattern.

Interestingly, while Vijaykumar's findings indicate a general increase in bias across all mass ratios with rising inclination angles, our results reveal a deviation in systems with low mass ratios ($q = 0.2$). Specifically, for these low mass ratio systems, the inclination angle decreases as ι increases. This counterintuitive trend suggests that the relationship between inclination angle and bias is not uniform across different mass ratios. The underlying cause may stem from the distinct waveform characteristics of low mass ratio binaries, where the secondary object exerts a significant influence on the overall GW signal morphology. Such systems might exhibit unique dynamical behaviors or waveform features that mitigate the bias typically introduced by higher inclination angles. Additionally, this deviation highlights potential variations in system dynamics that could be influenced by factors such as spin-orbit coupling, or other astrophysical processes not fully captured in existing waveform models.

For systems with higher SNRs, we observe a notable discrepancy between our results and those reported in Aditya Vijaykumar's study [80]. While Vijaykumar noted an increase in biases across all recovered parameters for very low mass ratios (q) as the inclination angle (ι) increased, our findings present a contrary trend. Specifically, our analysis reveals a decreasing trend in the biases associated with the recovery of chirp mass, luminosity distance, and coalescence time at higher SNRs. This divergence suggests that our modeling approach or data analysis methods may respond differently under conditions of higher SNR, particularly for systems with low mass ratios. One possible explanation is that higher SNRs provide more precise GW signal information, allowing for better disentanglement of parameter degeneracies and thus reducing biases in parameter estimation. Alternatively, differences in the waveform models, noise treatment, or statistical inference techniques employed between the two studies could account for the observed discrepancies. This divergence underscores the importance of continuous refinement and validation of GW parameter estimation methods, especially as detectors become more sensitive and capable of observing a wider variety of binary systems.

Overall, these comparative insights highlight the nuanced interplay between system parameters such as mass ratio and inclination angle, and their impact on GW parameter estimation biases. Understanding these relationships is crucial for improving the accuracy of GW measurements and for refining theoretical models of binary mergers. Future work should focus on exploring the underlying causes of these discrepancies, potentially through more sophisticated waveform modeling, enhanced noise mitigation strategies, or the incorporation of additional physical effects that may influence parameter recovery in GW observations.

5.2 Binary neutron star

We employ the `IMRPhenomD_NRTidal` waveform model to simulate BNS systems. In this context, IMR represents the Inspiral-Merger-Ringdown framework. Specifically, IMRPhenomD is a phenomenological model originally developed to describe GWforms from BBH mergers. The NRTidal component adds corrections to account for tidal effects unique to NSs. As NSs merge, their internal structure and tidal deformability influence the emitted GWs, making these effects essential for distinguishing BNS systems from BBHs.

For the simulation, we use sensitivity files from three detectors: H1, L1, and V1, and assume Gaussian noise to simulate a realistic interferometric noise environment. The signal is sampled at a frequency of 2048 Hz over a time duration of 32 seconds. The source is modeled using the `LALSuite` (LIGO Algorithm Library Suite), with parameters consistent with the injected values. These injected values include NS masses of $1.5M_\odot$ and $1.3M_\odot$, aligned spins of 0.02 for both stars, and tidal deformabilities of $\lambda_1 = 545$ and $\lambda_2 = 1346$. Additional parameters include a luminosity distance of 50 Mpc, an inclination angle $\iota = 0.4$ radians, a polarization angle $\psi = 2.659$ radians, a phase $\phi = 1.3$, and sky locations $\alpha = 1.375$ radians and $\delta = -1.2108$ radians.

Parameter estimation was performed using the nested sampler `Dynesty`.

Figure 25 and Figure 26 illustrate the posterior distributions for the $\mathcal{M}$, q, χ_1 and χ_2, d_L, $\theta_{\rm JN}$, ψ, ϕ, α and δ, and tidal deformabilities (λ_1 and λ_2) obtained using Type-I and Type-II templates for a BNS system. Both Type-I and Type-II images can recover the injected values very well, except for the mass ratio and tidal deformabilities. In addition, the correlation of ψ and ϕ from Type-II image shows an unexpected shape.

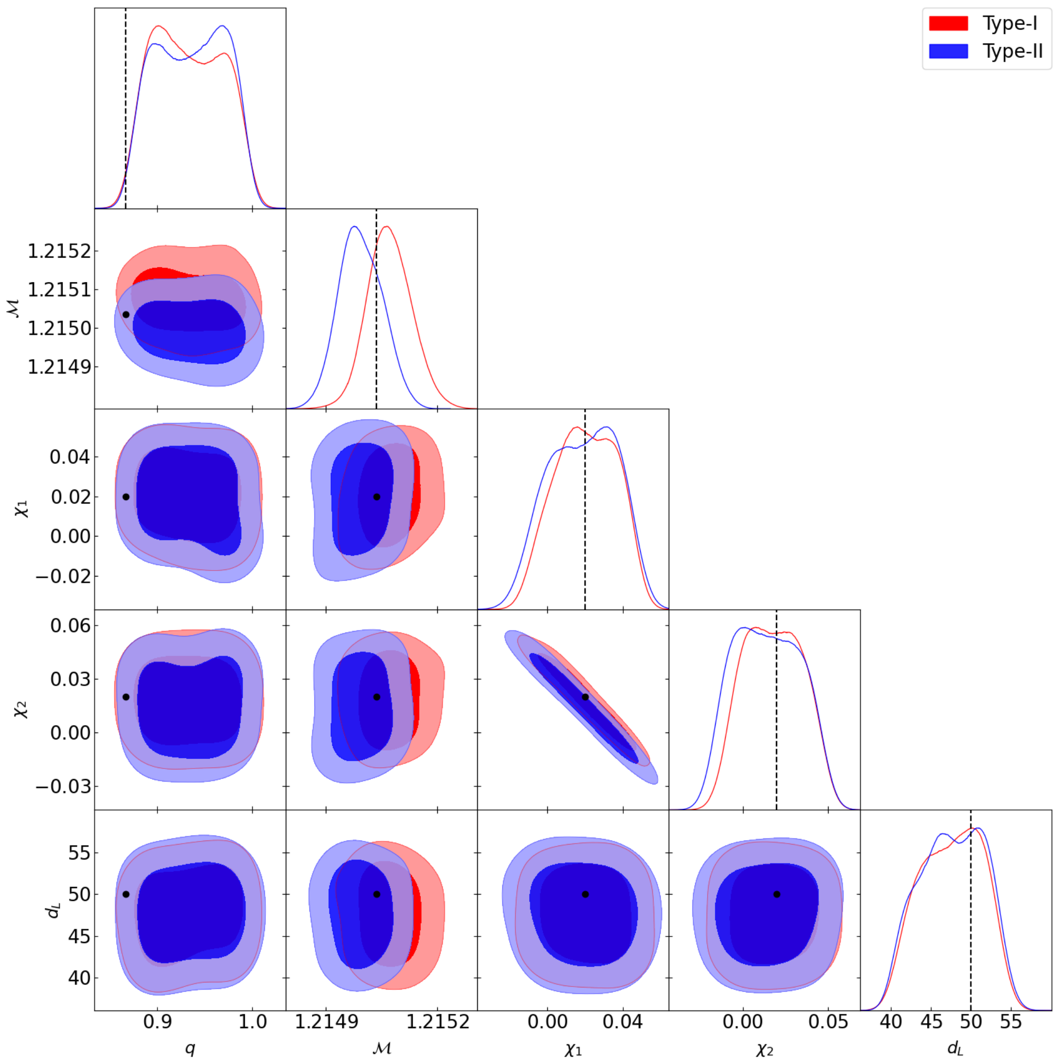

Figure 25: The plots shows the distribution of posteriors of Type-I (red) and Type-II (blue) templates for BNS. The SNR is 57.15.

6 Conclusion

In this thesis, we aimed to investigate the impact of gravitational lensing on GWs as they traverse the massive cosmic structures in their journey to Earth. Specifically, we sought to determine whether gravitational lensing, known to magnify, induce phase shifts, and cause time delays, could be detected and how these effects might bias the interpretation of GW signals.

We first established a strong theoretical foundation by reviewing the production, propagation, and detection of GWs, with particular focus on instruments like LIGO and Virgo. Using Bayesian inference for parameter estimation, we analyzed how effectively the posterior distributions recovered the injected parameters that define GWs. Additionally, we tested the efficiency of the relative binning method on non-lensed binary NS systems, demonstrating its potential to significantly reduce computational sampling time without introducing bias into the parameter

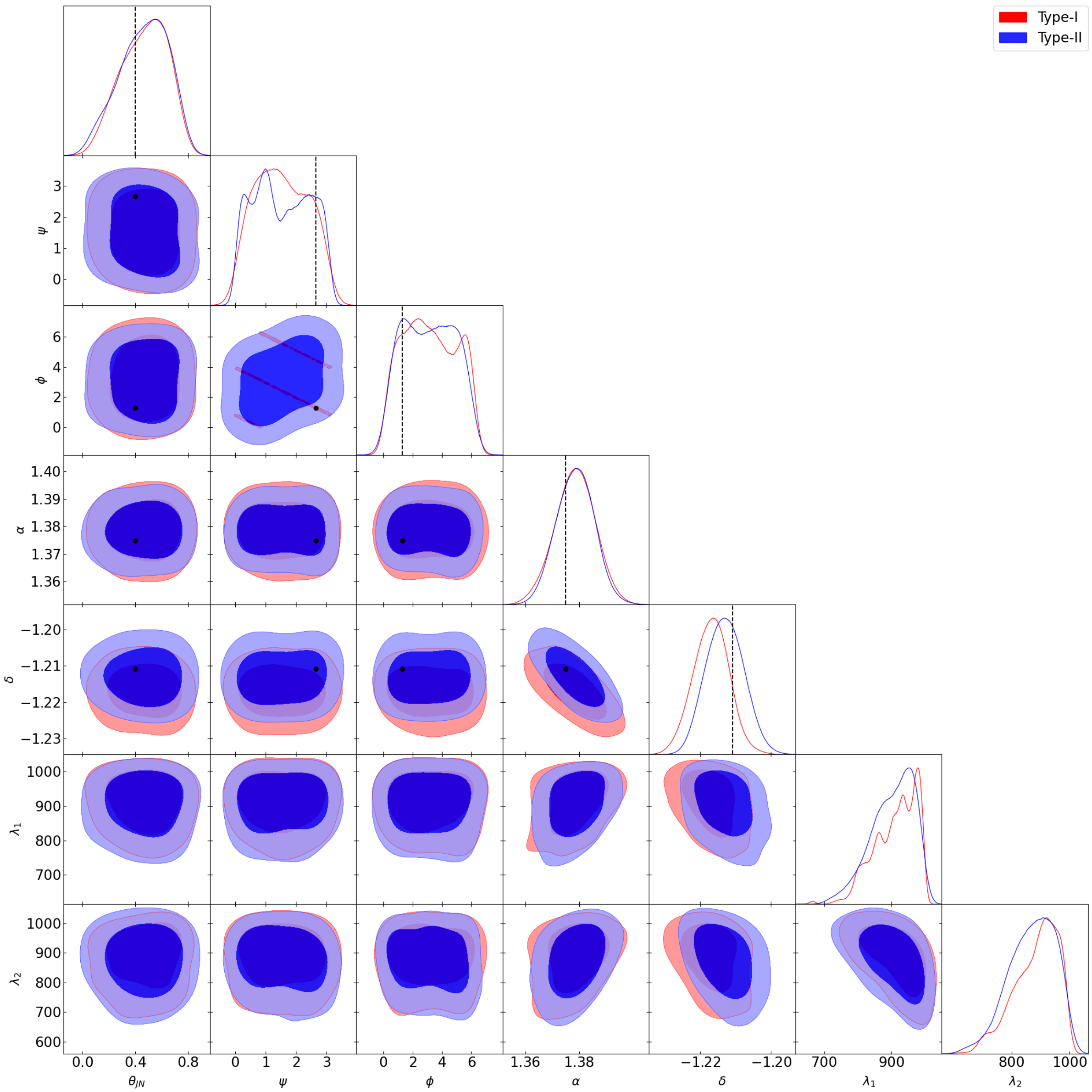

Figure 26: The injected values of λ_1 and λ_2 are out of the range of posterior distributions in the plot.

estimation results.

Our findings are compelling.

- In the wave optics regime, we derived a GW waveform that is magnified and distorted under the influence of lensing and showed that within different impact parameters and lens masses the amplification factor varies in both phase shift and magnification.

- In the geometric optics regime, we categorized the resulting lensed waveforms into three distinct types. Parameter estimation showed that at low SNR, significant bias in the recovered sky location occurred for type-III images. As SNR increased, sky locations were accurately recovered; however, key intrinsic parameters, such as mass ratio and chirp mass, remained challenging to estimate. For very low mass ratio, a significant bias occurred in recovering luminosity distance for all images.

- With particular focus on the effects of inclination angles, we found that the biases tend to increase with inclination angle for most parameters, especially for higher mass ratios ($q = 0.5$ and $q = 0.8$). Certain parameters, such as luminosity distance and inclination angle, show systematic biases at specific ranges of ι when the SNR is low ($\rho = 19.6$).

- Higher SNR improves the recovery of some parameters, such as chirp mass and coalescence time, with biases becoming more stable. However, biases in luminosity distance and inclination angle remain substantial, particularly for $q = 0.8$, where the highest peaks are observed at larger inclination angles. Fluctuations in bias curves are more pronounced compared to the lower SNR case, reflecting the interplay of signal strength and parameter sensitivity.

While gravitational lensing can introduce detectable biases into GW signals, these effects are detailed and depend heavily on system-specific parameters like SNR, mass ratio, and inclination angle. Future studies should focus on refining parameter estimation techniques in regimes where lensing effects are prominent, in order to deepen our understanding of both GWs and the large-scale structures that lens them.

However, challenges remain. Further investigation is required to improve parameter estimation in the wave optics regime and gain deeper insights into gravitational lensing in this context. The relative binning method, while effective for non-lensed events, presents limitations when applied to lensed events. Future studies should also focus on non-lensed BBH systems to explore how variations in injected parameter values affect posterior distributions. Additionally, the oscillatory patterns observed in bias quantification need further simulations to fully understand their nature, and the current research on BNSs is still incomplete and requires additional work.

In conclusion, this thesis represents a step forward in understanding how GWs interact with the large-scale structures of the universe. While significant progress has been made, there is still much to uncover. Future research, supported by next-generation detectors and advanced modeling, will continue this journey, allowing GWs to be used as a tool not only to observe the universe's most violent events but also to map its structure on a cosmological scale. The exploration of GWs is ongoing, and this work marks only the beginning of a larger scientific endeavor.

7 Acknowledgments

This work has opened a door for me into the mysterious and awe-inspiring world of cosmology. It allowed me to build a solid foundation in physics and mathematics, starting from scratch, to comprehend the nature of black holes (BHs), how they warp and distort spacetime, and how they ultimately generate gravitational waves (GWs)—faint but powerful signals that we can still detect and decode from thousands of megaparsecs away. I feel incredibly privileged to have had this glimpse into such a dark, enigmatic, and yet beautiful part of our universe.

The journey began with a pre-project for this thesis in February 2023 and culminated in its completion in December 2024. Over the past 22 months, I have traversed a landscape of emotions—moments of deep frustration, self-doubt, and even depression, but also moments of joy, amazement, and genuine satisfaction. This journey has been one of personal growth and discovery, both intellectually and emotionally. Thankfully, through perseverance and the guidance of incredible people, it has all been worth it.

First and foremost, I would like to express my deepest and most sincere gratitude to my supervisor, José María Ezquiaga, for his unwavering support, exceptional mentorship, and patient guidance throughout these nearly two years. His positivity and kindness have been a constant source of encouragement during challenging times, and his dedication to fostering both my academic skills and confidence has been invaluable. José has not only been a mentor but a role model, and it has been an absolute privilege and joy to work under his supervision.

I am also truly grateful to the wonderful members of our research group—Rico, Juno, and Luka. Despite the physical distance, their camaraderie and collaboration have made this journey far less lonely and infinitely more enjoyable. To Rico, in particular, I owe a special thanks for his generous and patient assistance with Bilby—a tool I might still be struggling with without his expertise. His willingness to share knowledge and help others has made a significant difference in my work.

In addition, I would like to extend my acknowledgment to a steadfast companion over the past two years—the Tycho supercomputer, hosted at the SCIENCE HPC Center at the University of Copenhagen. Tycho's immense computational power and reliability made this work possible, enabling me to perform the large-scale analyses required for this research. Tycho has been the silent yet indispensable partner in unraveling some of the mysteries of black holes and gravitational waves.

This thesis would not have been possible without the unwavering emotional and financial support of my family. Their belief in me, even when I doubted myself, provided the foundation I needed to persist through difficult times. I owe them more than words can express.

Lastly, to my best friend of all time, Bai Yifan—thank you for always being my rock. Your constant presence, understanding, and encouragement have meant the world to me. Whether I needed someone to vent to, share a laugh with, or simply remind me that I could do this, you were always there. For that, and for everything you've done, I am forever grateful.

This thesis marks not just the completion of a project but the beginning of a new chapter, filled with curiosity and a deeper appreciation for the universe and the people who help us explore it. To everyone who has been part of this journey—thank you.

References

[1] M. Grespan and M. Biesiada, "Strong gravitational lensing of gravitational waves: A review," Universe, vol. 9, no. 5, 2023.

[2] K. Schwarzschild, "On the gravitational field of a mass point according to Einstein's theory," Sitzungsber. Preuss. Akad. Wiss. Berlin (Math. Phys.), vol. 1916, pp. 189–196, 1916.

[3] D. Finkelstein, "Past-future asymmetry of the gravitational field of a point particle," Phys. Rev., vol. 110, pp. 965–967, May 1958.

[4] M. D. Kruskal, "Maximal extension of schwarzschild metric," Phys. Rev., vol. 119, pp. 1743–1745, Sep 1960.

[5] R. P. Kerr, "Gravitational field of a spinning mass as an example of algebraically special metrics," Phys. Rev. Lett., vol. 11, pp. 237–238, Sep 1963.

[6] C. V. Vishveshwara, "Scattering of Gravitational Radiation by a Schwarzschild Black-hole," Nature, vol. 227, pp. 936–938, 1970.

[7] W. H. Press, "Long Wave Trains of Gravitational Waves from a Vibrating Black Hole," , vol. 170, p. L105, Dec. 1971.

[8] S. Chandrasekhar and S. Detweiler, "The Quasi-Normal Modes of the Schwarzschild Black Hole," Proceedings of the Royal Society of London Series A, vol. 344, pp. 441–452, Aug. 1975.

[9] L. Blanchet, T. Damour, B. R. Iyer, C. M. Will, and A. G. Wiseman, "Gravitational-radiation damping of compact binary systems to second post-newtonian order," Phys. Rev. Lett., vol. 74, pp. 3515–3518, May 1995.

[10] L. Blanchet, "Gravitational radiation from post-newtonian sources and inspiralling compact binaries," Living Rev. Relativ., vol. 17, no. 2, 2014.

[11] A. Buonanno and T. Damour, "Effective one-body approach to general relativistic two-body dynamics," Phys. Rev. D, vol. 59, p. 084006, Mar 1999.

[12] B. L. Webster and P. Murdin, "Cygnus x-1: A spectroscopic binary with a heavy companion.," Nature (London) 235: No. 5332, 37-8(7 Jan 1972)., 1 1972.

[13] C. T. Bolton, "Dimensions of the binary system hde 226868 = cygnus x-1.," Nature (London) Phys. Sci. 240: No. 102, 124-7(11 Dec 1972)., 1 1972.

[14] J. Casares and P. G. Jonker, “Mass measurements of stellar and intermediate-mass black holes,” Space Science Reviews, vol. 183, p. 223–252, Dec. 2013.

[15] B. Abbott et al., “Observation of gravitational waves from a binary black hole merger,” Physical Review Letters, vol. 116, Feb. 2016.

[16] J. Weber, “Detection and generation of gravitational waves,” Phys. Rev., vol. 117, pp. 306–313, Jan 1960.

[17] M. E. Gertsenshtein and V. I. Pustovoit, “On the Detection of Low Frequency Gravitational Waves,” Sov. Phys. JETP, vol. 16, p. 433, 1962.

[18] G. E. Moss, L. R. Miller, and R. L. Forward, “Photon-noise-limited laser transducer for gravitational antenna,” Appl. Opt., vol. 10, pp. 2495–2498, Nov 1971.

[19] R. Weiss, “Republication of: Electromagnetically coupled broadband gravitational antenna,” General Relativity and Gravitation, vol. 54, no. 153, 2022.

[20] R. W. P. Drever, “Gravitational radiation,” in Gravitational Radiation (N. Deruelle and T. Piran, eds.), p. 321, Amsterdam: North-Holland, 1983.

[21] R. W. P. Drever, F. J. Raab, K. S. Thorne, R. Vogt, and R. Weiss, “Laser interferometer gravitational-wave observatory (ligo) technical report,” tech. rep., LIGO, 1989. LIGO-M890001.

[22] J. Hough et al., “Proposal for a joint german-british interferometric gravitational wave detector,” MPQ Technical Report 147, No. GWD/137/JH(89), Max Planck Institute for Quantum Optics (MPQ), 1989.

[23] A. Abramovici, W. E. Althouse, R. W. P. Drever, Y. Gursel, S. Kawamura, F. J. Raab, D. Shoemaker, L. Sievers, R. E. Spero, K. S. Thorne, R. E. Vogt, R. Weiss, S. E. Whitcomb, and M. E. Zucker, “Ligo: The laser interferometer gravitational-wave observatory,” Science, vol. 256, pp. 325–333, 1992.

[24] A. Brillet, A. Giazotto, et al., “Virgo project technical report,” Tech. Rep. VIR-0517A-15, Virgo Project, 1989.

[25] J. Aasi et al., “Advanced ligo,” Classical and Quantum Gravity, vol. 32, no. 7, p. 074001, 2015.

[26] F. Acernese et al., “Advanced virgo: a second-generation interferometric gravitational wave detector,” Classical and Quantum Gravity, vol. 32, no. 2, p. 024001, 2015.

[27] C. Affeldt et al., “Advanced techniques in the geo 600 gravitational wave detector,” Classical and Quantum Gravity, vol. 31, no. 22, p. 224002, 2014.

[28] Y. Aso, Y. Michimura, K. Somiya, M. Ando, O. Miyakawa, T. Sekiguchi, D. Tatsumi, and H. Yamamoto, “Interferometer design of the kagra gravitational wave detector,” Physical Review D, vol. 88, no. 4, p. 043007, 2013.

[29] R. A. Hulse and J. H. Taylor, “Discovery of a pulsar in a binary system.,” , vol. 195, pp. L51–L53, Jan. 1975.

[30] B. Abbott et al., “Gw170817: Observation of gravitational waves from a binary neutron star inspiral,” Physical Review Letters, vol. 119, Oct. 2017.

[31] B. Abbott et al., “Gw150914: First results from the search for binary black hole coalescence with advanced ligo,” Physical Review D, vol. 93, June 2016.

[32] D. Kasen, B. D. Metzger, J. Barnes, E. Quataert, and E. Ramirez-Ruiz, “Origin of the heavy elements in binary neutron-star mergers from a gravitational wave event,” Nature, vol. 551, no. 7678, pp. 80–84, 2017.

[33] B. P. Abbott et al., “Tests of general relativity with gw150914,” Physical Review Letters, vol. 116, no. 22, p. 221101, 2016.

[34] R. Abbott et al., “GWTC-2: Compact binary coalescences observed by ligo and virgo during the first half of the third observing run,” Physical Review X, vol. 11, no. 2, p. 021053, 2021.

[35] C. W. Misner, K. S. Thorne, and J. A. Wheeler, Gravitation. W. H. Freeman and Company, 1973.

[36] S. Weinberg, Gravitation and Cosmology: Principles and Applications of the General Theory of Relativity. Wiley, 1972.

[37] B. F. Schutz, A First Course in General Relativity. Cambridge University Press, 2009.

[38] R. A. Isaacson, “Gravitational radiation in the limit of high frequency. i. the linear approximation and geometrical optics,” Physical Review, vol. 166, no. 5, pp. 1263–1271, 1968.

[39] M. Maggiore, Gravitational Waves: Volume 1: Theory and Experiments. Oxford University Press, online edition ed., 2007.

[40] L. Blanchet, “Post-newtonian theory for gravitational waves,” 2024.

[41] K. S. Thorne, “Gravitational radiation,” in Three Hundred Years of Gravitation (S. W. Hawking and W. Israel, eds.), pp. 330–458, Cambridge University Press, 1987.

[42] S. Weinberg, Cosmology. Oxford: Oxford University Press, 2008.

[43] D. W. Hogg, “Distance measures in cosmology,” arXiv preprint, 1999.

[44] G. Pratten, C. García-Quirós, M. Colleoni, A. Ramos-Buades, H. Estellés, M. Mateu-Lucena, R. Jaume, M. Haney, D. Keitel, J. E. Thompson, and S. Husa, “Computationally efficient models for the dominant and subdominant harmonic modes of precessing binary black holes,” Physical Review D, vol. 103, May 2021.

[45] K. S. Thorne, “Multipole expansions of gravitational radiation,” Rev. Mod. Phys., vol. 52, pp. 299–339, Apr 1980.

[46] L. E. Kidder, “Using full information when computing modes of post-newtonian waveforms from inspiralling compact binaries in circular orbit,” Physical Review D, vol. 77, Feb. 2008.

[47] C. K. Mishra, A. Kela, K. G. Arun, and G. Faye, “Ready-to-use post-newtonian gravitational waveforms for binary black holes with nonprecessing spins: An update,” Phys. Rev. D, vol. 93, p. 084054, Apr 2016.

[48] H. A. Lorentz and J. Droste, “The motion of a system of bodies under the influence of their mutual attraction, according to einstein’s theory,” in The Collected Papers of H.A. Lorentz, vol. 5, pp. 330–355, Nijhoff, The Hague, 1937. Translated from Versl. K. Akad. Wet. Amsterdam, 26, 392 and 649 (1917).

[49] C. M. Will, “The confrontation between general relativity and experiment,” Living Reviews in Relativity, vol. 17, p. 4, 2014.

[50] T. Damour, P. Jaranowski, and G. Schäfer, “Dynamics of compact binaries in general relativity: The third post-newtonian order,” Physical Review D, vol. 62, p. 044024, 2000.

[51] L. E. Kidder, “Coalescing binary systems of compact objects to (post)5/2-newtonian order. v. spin effects,” Physical Review D, vol. 52, p. 821, 1995.

[52] P. Ajith et al., “Phenomenological template family for black-hole coalescence waveforms,” Classical and Quantum Gravity, vol. 24, p. S689, 2007.

[53] B. Abbott et al., “Properties of the binary black hole merger gw150914,” Physical Review Letters, vol. 116, June 2016.

[54] T. Hinderer, L. Rezzolla, and L. Baiotti, “Gravitational waves from merging binary neutron-star systems,” in The Physics and Astrophysics of Neutron Stars (L. Rezzolla, P. Pizzochero, D. I. Jones, N. Rea, and I. Vidaña, eds.), vol. 457 of Astrophysics and Space Science Library, pp. 575–635, Cham: Springer, 2019.

[55] E. Thrane and C. Talbot, “An introduction to bayesian inference in gravitational-wave astronomy: Parameter estimation, model selection, and hierarchical models,” Publications of the Astronomical Society of Australia, vol. 36, 2019.

[56] B. Allen and J. D. Romano, “Detecting a stochastic background of gravitational radiation: Signal processing strategies and sensitivities,” Physical Review D, vol. 59, no. 10, p. 102001, 1999.

[57] L. S. Finn, “Detection, measurement, and gravitational radiation,” Physical Review D, vol. 46, no. 12, pp. 5236–5249, 1992.

[58] J. M. Ezquiaga, D. E. Holz, W. Hu, M. Lagos, and R. M. Wald, “Phase effects from strong gravitational lensing of gravitational waves,” Physical Review D, vol. 103, no. 6, 2021.

[59] P. Jaranowski and A. Królak, “Gravitational-wave data analysis. formalism and sample applications: The gaussian case,” Living Reviews in Relativity, vol. 15, p. 4, 2012.

[60] LIGO Scientific Collaboration et al., “Advanced LIGO,” Classical and Quantum Gravity, vol. 32, p. 074001, Apr. 2015.

[61] P. Brady, G. Losurdo, and H. Shinkai, LIGO, VIRGO, and KAGRA as the International Gravitational Wave Network, pp. 1205–1225. Singapore: Springer Nature Singapore, 2022.

[62] LIGO Scientific Collaboration, “Observing plans for ligo, virgo, and kagra,” 2024. Accessed: 2024-09-16.

[63] L. S. Collaboration and V. Collaboration, “Ligo’s fourth observing run (o4) begins with significant improvements in sensitivity,” 2024. Updates on LIGO’s O4 run and detector improvements. Accessed: 2024-09-16.

[64] T. Akutsu et al., “Kagra: 2.5 generation interferometric gravitational wave detector,” Nature Astronomy, vol. 3, p. 35–40, Jan. 2019.

[65] T. Akutsu et al., “Overview of kagra: Detector design and construction history,” 2020.

[66] t. Accadia, F. Acernese, M. Alshourbagy, P. Amico, F. Antonucci, S. Aoudia, N. Arnaud, C. Arnault, K. Arun, P. Astone, S. Avino, D. Babusci, G. Ballardin, F. Barone, G. Barrand, L. Barsotti, M. Barsuglia, A. Basti, T. Bauer, and Z. Zhang, “Virgo: A laser interferometer to detect gravitational waves,” Journal of Instrumentation, vol. 7, p. P03012, 03 2012.

[67] F. Acernese et al., “Advanced virgo: a second-generation interferometric gravitational wave detector,” Classical and Quantum Gravity, vol. 32, p. 024001, Dec. 2014.

[68] B. Abbott et al., "Gw170814: A three-detector observation of gravitational waves from a binary black hole coalescence," Physical Review Letters, vol. 119, Oct. 2017.

[69] A. R. A. C. Wierda, E. Wempe, O. A. Hannuksela, L. V. E. Koopmans, and C. Van Den Broeck, "Beyond the detector horizon: Forecasting gravitational-wave strong lensing," The Astrophysical Journal, vol. 921, p. 154, nov 2021.

[70] Y. Aso et al., "Interferometer design of the kagra gravitational wave detector," Physical Review D, vol. 88, Aug. 2013.

[71] T. Akutsu et al., "Overview of kagra: Detector design and construction history," 2020.

[72] M. Saleem et al., "The science case for ligo-india," Classical and Quantum Gravity, vol. 39, p. 025004, Dec. 2021.

[73] D. Reitze et al., "Cosmic explorer: The u.s. contribution to gravitational-wave astronomy beyond ligo," 2019.

[74] B. Sathyaprakash et al., "Scientific objectives of einstein telescope," Classical and Quantum Gravity, vol. 29, p. 124013, June 2012.

[75] R. K. L. Lo, L. Vujeva, J. M. Ezquiaga, and J. C. L. Chan, "Observational signatures of highly magnified gravitational waves from compact binary coalescence," 2024.

[76] R. Blandford and R. Narayan, "Fermat's Principle, Caustics, and the Classification of Gravitational Lens Images," , vol. 310, p. 568, Nov. 1986.

[77] P. Schneider, J. Ehlers, and E. E. Falco, Gravitational Lenses. Astronomy and Astrophysics Library, New York: Springer, 1992.

[78] R. Narayan and M. Bartelmann, "Lectures on gravitational lensing," 1996. Preprint available at arXiv:astro-ph/9606001.

[79] A. O. Petters, H. Levine, and J. Wambsganss, Singularity Theory and Gravitational Lensing. Boston: Birkhäuser, 2001.

[80] A. Vijaykumar, A. K. Mehta, and A. Ganguly, "Detection and parameter estimation challenges of type-ii lensed binary black hole signals," 2023.

[81] L. Dai and T. Venumadhav, "On the waveforms of gravitationally lensed gravitational waves," 2017.

[82] Y. Wang, R. K. Lo, A. K. Li, and Y. Chen, "Identifying type ii strongly lensed gravitational-wave images in third-generation gravitational-wave detectors," Physical Review D, vol. 103, May 2021.

[83] M. Grespan and M. Biesiada, "Strong Gravitational Lensing of Gravitational Waves: A Review," Universe, vol. 9, p. 200, Apr. 2023.

[84] R. M. Wald, General Relativity. Chicago: University of Chicago Press, 1984.

[85] R. P. Feynman and A. R. Hibbs, Quantum Mechanics and Path Integrals. New York: McGraw-Hill, 1965.

[86] M. Born and E. Wolf, Principles of Optics. Oxford: Pergamon Press, 1999.

[87] E. L. Lehmann and G. Casella, Theory of Point Estimation. Springer, 1998.

[88] B. P. Abbott, R. Abbott, T. D. Abbott, et al., "Observation of gravitational waves from a binary black hole merger," Physical Review Letters, vol. 116, no. 6, p. 061102, 2016.

[89] C. Cutler and E. E. Flanagan, "Gravitational waves from merging compact binaries: How accurately can one extract the binary's parameters from the inspiral waveform?," Physical Review D, vol. 49, no. 6, pp. 2658–2697, 1994.

[90] J. Veitch and A. Vecchio, "Bayesian coherent analysis of in-spiral gravitational wave signals with a detector network," Physical Review D, vol. 81, no. 6, p. 062003, 2010.

[91] G. Ashton et al., "Bilby: A user-friendly bayesian inference library for gravitational-wave astronomy," The Astrophysical Journal Supplement Series, vol. 241, no. 2, p. 27, 2019.

[92] J. Veitch, V. Raymond, B. Farr, et al., "Parameter estimation for compact binaries with ground-based gravitational-wave observations using the lalinference software library," Physical Review D, vol. 91, no. 4, p. 042003, 2015.

[93] J. Skilling, "Nested sampling for general bayesian computation," Bayesian Analysis, vol. 1, no. 4, pp. 833–859, 2006.

[94] N. Christensen and R. Meyer, "Parameter estimation with gravitational waves," Reviews of Modern Physics, vol. 94, Apr. 2022.

[95] A. Gelman, J. B. Carlin, H. S. Stern, D. B. Dunson, A. Vehtari, and D. B. Rubin, Bayesian Data Analysis. Boca Raton: Chapman and Hall/CRC, 3rd ed., 2013.

[96] D. J. Mackay, Information Theory, Inference, and Learning Algorithms. Cambridge University Press, 2003.

[97] C. Andrieu, N. de Freitas, A. Doucet, and M. I. Jordan, "An introduction to mcmc for machine learning," Machine Learning, vol. 50, no. 1-2, pp. 5–43, 2003.

[98] W. R. Gilks, S. Richardson, and D. J. Spiegelhalter, Markov Chain Monte Carlo in Practice. Chapman and Hall/CRC, 1996.

[99] N. Metropolis, A. W. Rosenbluth, M. N. Rosenbluth, A. H. Teller, and E. Teller, “Equation of state calculations by fast computing machines,” The Journal of Chemical Physics, vol. 21, no. 6, pp. 1087–1092, 1953.

[100] W. K. Hastings, “Monte carlo sampling methods using markov chains and their applications,” Biometrika, vol. 57, no. 1, pp. 97–109, 1970.

[101] W. Handley, M. Hobson, and A. Lasenby, “Polychord: next-generation nested sampling,” Monthly Notices of the Royal Astronomical Society, vol. 453, no. 4, pp. 4384–4398, 2015.

[102] F. Feroz, M. P. Hobson, and M. Bridges, “Multinest: an efficient and robust bayesian inference tool for cosmology and particle physics,” Monthly Notices of the Royal Astronomical Society, vol. 398, no. 4, pp. 1601–1614, 2009.

[103] G. Ashton, M. Hübner, P. D. Lasky, C. Talbot, K. Ackley, S. Biscoveanu, Q. Chu, A. Divakarla, P. J. Easter, B. Goncharov, F. Hernandez Vivanco, J. Harms, M. E. Lower, G. D. Meadors, D. Melchor, E. Payne, M. D. Pitkin, J. Powell, N. Sarin, R. J. E. Smith, and E. Thrane, “BILBY: A User-friendly Bayesian Inference Library for Gravitational-wave Astronomy,” , vol. 241, p. 27, Apr. 2019.

[104] K. Krishna, A. Vijaykumar, A. Ganguly, C. Talbot, S. Biscoveanu, R. N. George, N. Williams, and A. Zimmerman, “Accelerated parameter estimation in bilby with relative binning,” 2023.

[105] B. Zackay, L. Dai, and T. Venumadhav, “Relative binning and fast likelihood evaluation for gravitational wave parameter estimation,” 2018.